

RICE UNIVERSITY

**Resolving the Nanoscale Mechanisms of Calcite Growth and Dissolution
from Nonstoichiometric and Microbial Solutions**


by

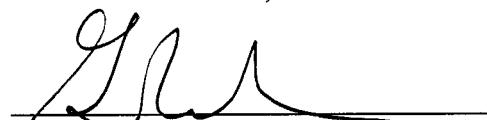
Kevin James Davis


A THESIS SUBMITTED
IN PARTIAL FULFILLMENT OF THE
REQUIREMENTS FOR THE DEGREE

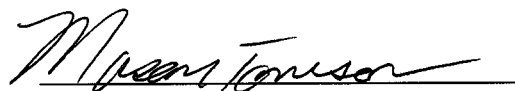
Doctor of Philosophy

APPROVED, THESIS COMMITTEE:


Andreas Lüttge, Chair
Associate Professor, Earth Science


Gerald R. Dickens
Associate Professor, Earth Science


Dale S. Sawyer
Professor, Earth Science


Mason B. Tomson
Professor of Civil and Environmental
Engineering

HOUSTON, TEXAS
MAY 2008

UMI Number: 3309854

INFORMATION TO USERS

The quality of this reproduction is dependent upon the quality of the copy submitted. Broken or indistinct print, colored or poor quality illustrations and photographs, print bleed-through, substandard margins, and improper alignment can adversely affect reproduction.

In the unlikely event that the author did not send a complete manuscript and there are missing pages, these will be noted. Also, if unauthorized copyright material had to be removed, a note will indicate the deletion.

UMI[®]

UMI Microform 3309854

Copyright 2008 by ProQuest LLC.

All rights reserved. This microform edition is protected against unauthorized copying under Title 17, United States Code.

ProQuest LLC
789 E. Eisenhower Parkway
PO Box 1346
Ann Arbor, MI 48106-1346

ABSTRACT

Resolving the Nanoscale Mechanisms of Calcite Growth and Dissolution from Nonstoichiometric and Microbial Solutions

by

Kevin James Davis

The relative rates of calcite (CaCO_3) precipitation and dissolution largely determine the preservation and subsequent accumulation of carbonate in the geologic record and are fundamental parameters for predicting the fate of fossil fuel carbon dioxide as well as the sequestration of several co-precipitated trace elements. Here we use the surface techniques, atomic force microscopy (AFM) and vertical scanning interferometry (VSI) to elucidate the nanoscale mechanisms of calcite growth and dissolution from nonstoichiometric and microbial solutions. Our results clearly demonstrate that the $\text{Ca}^{2+}/\text{CO}_3^{2-}$ ratio of carbonate solutions, at constant saturation, determines both the kinetics and anisotropy of step advancement. Anisotropic step velocities, in turn, alter step generation rates at screw dislocations, thereby significantly affecting the overall growth and dissolution rates of calcite surfaces. These results reflect different mechanistic roles for the cation and anion during both growth and dissolution and suggest limitations on the application of concentration-based rate laws in solutions of varying ionic ratios. Further, this study offers clear demonstration that the crystal surface exerts a primary control on growth and dissolution rates through step-specific and defect-directed interactions, producing differences in rate that could not be predicted from considerations

of bulk chemistry alone. Further insight into calcite dissolution in natural systems was achieved by investigating the effect of *Shewanella oneidensis* MR-1 surface colonization on the dissolution rates of calcite (CaCO_3) and dolomite ($\text{CaMg}(\text{CO}_3)_2$). By quantifying and comparing the significant processes occurring at the microbe–mineral interface, a mechanistic understanding of the way in which microbes alter the dissolution rates of carbonate minerals was achieved. MR-1 attachment under aerobic conditions was found to influence carbonate dissolution through two distinct mechanistic pathways: (1) inhibition through interference with etch pit development and (2) catalytic removal of carbonate material at the cell–mineral interface during irreversible attachment to the mineral surface. The relative importance of these two competing effects was found to vary with the solubility of the carbonate mineral studied. This study demonstrates the dynamic and competitive relationship between microbial surface colonization and mineral dissolution that may be expected to occur in natural environments.

*There is no higher or lower knowledge,
but one only, flowing out of experimentation.*

Leonardo da Vinci (1452-1519)

*Nothing tends so much to the advancement of knowledge as the application
of a new instrument. The native intellectual powers of men in different times
are not so much the causes of the different success of their labours, as the
peculiar nature of the means and artificial resources in their possession.*

Sir Humphrey Davy (1778-1829)

To my parents who afforded me every opportunity in life and made certain that the only limitations I faced were those of my own ambitions and dreams.

To my two beautiful friends, Lizette Leon-Rodriguez and Patricia Suarez, who were always there for me, whether I deserved them or not, and whose constant encouragement made completion of this work possible. They have touched my heart, each in their own way, taught me volumes about how to live, and have been a source of endless joy to me since I have known them.

Finally, this work is dedicated to the memories of Isaac Asimov (1920-1992) and Carl Sagan (1934-1996), who recognized the importance of communicating the many discoveries of science to the general public, so as to inspire future generations of scientists
... *including me.*

ACKNOWLEDGEMENTS

I am greatly indebted to my advisor, Andreas Lüttge, for his support and guidance throughout my dissertation research. I especially recognize his patience and encouragement during the many experimentally difficult periods leading to the completion of this dissertation. In addition to providing the foresight to pursue exciting new research directions in the field of geomicrobiology, he also provided me with the rare academic freedom to pursue unfunded research that eventually yielded novel insight into the mechanisms of calcite growth and dissolution.

This dissertation would also not be possible without the considerable expertise of Dr. Rolf S. Arvidson. Rolf was present in person, or in spirit, during every important step of the calcite growth and dissolution experiments. He was there during the early stages of the experimental design, helping to guide the formulation of the “Chipotle Hypotheses” as well as providing an early solution chemistry scheme that proved invaluable in the lab. Additionally, he was ever-present for key discussions that made the lab a much less lonely place to work.

Key insight and support for the geomicrobiology portion of this dissertation was provided by Dr. Kenneth H. Nealson at the University of Southern California. His advice and encouragement greatly facilitated the breadth and quality of this work.

Finally, I am extremely grateful for the constant support and understanding offered by my family throughout the many years of my research career.

This research would not be possible without the support of the U.S. Department of Energy (DE-FG03-02ER63427), Office of Naval Research (N00014-06-1-0115), Department of Defense Multidisciplinary University Research Initiative (FA9550-06-1-0292) and National Science Foundation (EEC-0118007). In addition, the facilities and resources of the Center for Biological and Environmental Nanotechnology (CBEN) at Rice University have been of constant empirical value during the performance of this dissertation.

TABLE OF CONTENTS

ABSTRACT.....	ii
DEDICATION.....	v
ACKNOWLEDGEMENTS.....	vi
TABLE OF CONTENTS.....	viii
LIST OF TABLES.....	xiii
LIST OF FIGURES.....	xiv
GENERAL INTRODUCTION.....	1
CHAPTER 1. THE ROLE OF $\text{Ca}^{2+}/\text{CO}_3^{2-}$ RATIO IN CALCITE GROWTH: MECHANISTIC INSIGHT INTO BIOMINERALIZATION AND CONSEQUENCES OF NONSTOICHIOMETRIC SOLUTIONS FOR CONCENTRATION-BASED RATE LAWS.....	4
Abstract.....	4
1.1 Introduction.....	5
1.1.1 Concentration-Based Rate Laws and Solution Stoichiometry.....	5
1.1.2 Kinetic Expectations for Nonstoichiometric Solutions.....	7
1.1.3 Potential Consequences of Nonstoichiometric Solutions for Calcium Carbonate Biomineralization.....	10
1.1.4 Step-Specific Measurements on the Calcite Cleavage Surface.....	14
1.2 Materials and Methods.....	23
1.2.1 Solution Chemistry Modeling.....	23
1.2.2 Solution Preparation.....	26
1.2.3 Atomic Force Microscopy (AFM) Experiments.....	26

1.2.4 Vertical Scanning Interferometry (VSI) Experiments.....	27
1.3 Results and Discussion.....	31
1.3.1 Saturation Controls: The Role of Saturation State in Anisotropy.....	31
1.3.2 Ratio Experiments: The Role of $\text{Ca}^{2+}/\text{CO}_3^{2-}$ Concentration Ratio in Calcite Growth.....	35
1.3.3 Vertical Scanning Interferometry (VSI): Surface Normal Calcite Growth Rates Under Different of $\text{Ca}^{2+}/\text{CO}_3^{2-}$ Concentration Ratios.....	44
1.4 Conclusions	
1.4.1 Solution Stoichiometry and Calcite Growth Rate: Implications for the Applicability of Affinity-Based Rate Laws.....	48
1.4.2 Solution Stoichiometry and Calcite Growth Anisotropy: Implications for Carbonate Biomineralization Strategies and Trace/Minor Element Proxies.....	51
1.4.3 The Importance of the Surface in Determining Growth Rates.....	53
CHAPTER 2. CALCITE DISSOLUTION IN NONSTOICHIOMETRIC SOLUTIONS: A SITE-SPECIFIC ROLE FOR CARBONATE CONTROL OF DISSOLUTION RATES.....	54
Abstract.....	54
2.1 Introduction.....	55
2.2 Materials and Methods.....	57
2.2.1 Solution Chemistry Modeling.....	57
2.2.2 Solution Preparation.....	59
2.2.3 Atomic Force Microscopy (AFM) Experiments.....	61
2.3 Results and Discussion.....	63

2.3.1 Dissolution at Dislocation Spirals.....	63
2.3.2 Saturation Controls: The Role of Saturation State in Anisotropy.....	66
2.3.3 Ratio Experiments: The Role of $\text{Ca}^{2+}/\text{CO}_3^{2-}$ Activity Ratio in Calcite Dissolution.....	74
2.4 Conclusions.....	95
2.5 Chapter Appendix.....	98
2.5.1 The Difference Between Growth and Dissolution at Near-Equilibrium Conditions.....	98
CHAPTER 3. QUANTIFYING THE RELATIONSHIP BETWEEN MICROBIAL ATTACHMENT AND MINERAL SURFACE DYNAMICS USING VERTICAL SCANNING INTERFEROMETRY.....	
Abstract.....	100
3.1 Introduction.....	101
3.1.1 Importance of Microbial Attachment in Biogeochemical and Engineered Systems.....	101
3.1.2 Critical Questions that Require Further Study.....	104
3.1.3 Quantifying Microbe-Mineral Interactions – A Challenge.....	106
3.2 Vertical Scanning Interferometry (VSI).....	107
3.3 The Application of VSI to the Quantification of Mineral Surface Dynamics in the Context of Microbial Attachment.....	110
3.4 Experimental Methods.....	111
3.4.1 Mineral-Surface Selection and Preparation.....	111
3.4.2 Shewanella Culture Preparation and Controls.....	112

3.4.3 Reaction Conditions.....	114
3.4.4 VSI And AFM Imaging and Measurements.....	115
3.5 Results and Discussion.....	116
3.5.1 Surface Colonization on Carbonate Surfaces.....	116
3.5.2 Comparison of VSI and AFM Imaging Techniques and Measurements.....	124
3.5.3 Role of Mineral-Surface Dynamics in Surface Colonization.....	128
3.5.4 Role of Surface Colonization in Determining Calcite Dissolution Rate.....	131
3.5.5 Role of Mineral-Surface Topography in Determining Surface Colonization.....	137
3.6 Summary and Conclusions.....	141
CHAPTER 4. CALCITE AND DOLOMITE DISSOLUTION RATES IN THE CONTEXT OF MICROBE-MINERAL SURFACE INTERACTIONS.....	144
Abstract.....	144
4.1 Introduction.....	145
4.2 Experimental Methods.....	150
4.2.1 MR-1 Culture Preparation and Controls.....	150
4.2.2 Reaction Conditions.....	152
4.2.3 VSI and AFM Imaging and Measurements.....	153
4.3 Results and Discussion.....	155
4.3.1 Surface Colonization on Carbonate Surfaces.....	155
4.3.2 Role of Surface Colonization in Determining Calcite Dissolution Rate.....	162
4.3.3 Role of Surface Colonization in	

Dolomite Dissolution.....	167
4.3.4 Role of Microbial Entrenchment in Carbonate Dissolution.....	168
4.4 Conclusions.....	179
GENERAL CONCLUSIONS.....	182
REFERENCES.....	185

LIST OF TABLES

CHAPTER 1.

Table 1.1 Theoretical and Empirical Rate Expressions for Precipitation from Solution.....	6
Table 1.2 Solution Speciation for the Saturation Controls and Ratio Experiments with Preparation Parameters.....	25
Table 1.3 AFM Data for the Saturation Controls and Ratio Experiments.....	34
Table 1.4 VSI Data for the Saturation Controls and Ratio Experiments.....	46

CHAPTER 2.

Table 2.1 Solution Speciation for the Saturation Controls and Ratio Experiments with Preparation Parameters.....	60
Table 2.2 AFM Data for the Saturation Controls and Ratio Experiments.....	68

CHAPTER 3.

Table 3.1 Average Measured Attached Cell Densities (Cells/100 μm^2).....	132
Table 3.2 Calcite Dissolution Measurements After 35 Hours.....	135
Table 3.3 Measured Attached Cell Densities on Pristine and Pre-Etched Surfaces after 4 Hours (Cells/100 μm^2).....	139

CHAPTER 4.

Table 4.1 Calcite Dissolution Measurements after 8 and 33.5 Hours.....	164
Table 4.2 Trench Depth for Calcite and Dolomite after 8 and 33.5 Hours.....	176

LIST OF FIGURES

CHAPTER 1.

Figure 1.1 Important Interactions of Growth Units with the Surface of an Idealized Kossel Crystal.....	8
Figure 1.2 Calcite Growth Hillocks Showing Anisotropy.....	15
Figure 1.3 AFM image of a growth spiral emanating from a screw dislocation on the {104} cleavage surface of calcite.....	17
Figure 1.4 A measure of the anisotropy of a growth hillock (ϕ).....	18
Figure 1.5 The Anisotropic Growth Condition.....	19
Figure 1.6 VSI images of a calcite surface following an AFM experiment.....	22
Figure 1.7 Measuring the Advancement of Individual Monomolecular Steps Relative to the y Scan Direction.....	28
Figure 1.8 Calcite Growth Hillocks Grown Under Different Saturation States at Constant $\text{Ca}^{2+}/\text{CO}_3^{2-}$ Concentration Ratio Equal to 1.....	33
Figure 1.9 Calcite Growth Hillocks Grown Under Different $\text{Ca}^{2+}/\text{CO}_3^{2-}$ Concentration Ratios at Constant Saturation State ($\sigma = 2.34$, $\Omega = 10.4$).....	36
Figure 1.10 Step Velocity Versus $\text{Ca}^{2+}/\text{CO}_3^{2-}$ Concentration Ratio at Constant Saturation.....	38
Figure 1.11 $\text{Ca}^{2+}/\text{CO}_3^{2-}$ Concentration Ratio Controls Step-Edge Anisotropy.....	39
Figure 1.12 v_{sum} Versus BCF Rate ($R = p\nu$).....	41
Figure 1.13 Period of Spiral Rotation Versus Saturation State and $\text{Ca}^{2+}/\text{CO}_3^{2-}$ Concentration Ratio.....	42

Figure 1.14 Period of Spiral Rotation Versus Step Velocity Anisotropy.....	43
Figure 1.15 VSI Measurements of Surface Normal Growth.....	45
Figure 1.16 VSI Measurements of Surface Normal Growth.....	47

CHAPTER 2.

Figure 2.1 Calcite Growth Hillocks and Dissolution Spirals Showing Anisotropy.....	64
Figure 2.2 AFM Image of a Calcite Dissolution Spiral.....	65
Figure 2.3 Calcite Dissolution Spirals Grown Under Different Saturation States at Constant $\text{Ca}^{2+}/\text{CO}_3^{2-}$ Concentration Ratio Equal to 1.....	69
Figure 2.4 Step Velocity Versus Undersaturation at Constant $\text{Ca}^{2+}/\text{CO}_3^{2-}$ Concentration Ratio.....	70
Figure 2.5 Period of Spiral Rotation Versus Undersaturation at Constant $\text{Ca}^{2+}/\text{CO}_3^{2-}$ Concentration Ratio.....	71
Figure 2.6 BCF Dissolution Rate Versus Undersaturation at Constant $\text{Ca}^{2+}/\text{CO}_3^{2-}$ Concentration Ratio.....	72
Figure 2.7 Step Velocity Anisotropy Versus Undersaturation at Constant $\text{Ca}^{2+}/\text{CO}_3^{2-}$ Concentration Ratio.....	73
Figure 2.8 Vicinal Slope Versus Undersaturation at Constant $\text{Ca}^{2+}/\text{CO}_3^{2-}$ Concentration Ratio.....	75
Figure 2.9 Step Velocity Versus Carbonate Concentration at Constant $\text{Ca}^{2+}/\text{CO}_3^{2-}$ Concentration Ratio.....	76
Figure 2.10 Calcite Growth Hillocks Grown Under Different $\text{Ca}^{2+}/\text{CO}_3^{2-}$ Concentration Ratios at Constant Undersaturation State	78
Figure 2.11 Step Velocity Anisotropy Versus $\text{Ca}^{2+}/\text{CO}_3^{2-}$ Concentration Ratio at Constant Undersaturation.....	79

Figure 2.12 Step Velocity Versus $\text{Ca}^{2+}/\text{CO}_3^{2-}$ Concentration Ratio at Constant Undersaturation.....	80
Figure 2.13 Step Velocity Versus $\text{Ca}^{2+}/\text{CO}_3^{2-}$ Concentration Ratio at Constant Undersaturation.....	81
Figure 2.14 Step Velocity Sum Versus $\text{Ca}^{2+}/\text{CO}_3^{2-}$ Concentration Ratio at Constant Undersaturation.....	83
Figure 2.15 Period of Spiral Rotation Versus $\text{Ca}^{2+}/\text{CO}_3^{2-}$ Concentration Ratio at Constant Undersaturation.....	85
Figure 2.16 Period of Spiral Rotation Versus Normalized Step Velocity Anisotropy at Constant Undersaturation.....	86
Figure 2.17 BCF Dissolution Rate Versus $\text{Ca}^{2+}/\text{CO}_3^{2-}$ Concentration Ratio at Constant Undersaturation.....	87
Figure 2.18 Velocity of the Positive (+) Step-Type Versus Carbonate Concentration.....	89
Figure 2.19 Velocity of the Negative (-) Step-Type Versus Carbonate Concentration.....	90
Figure 2.20 Step Velocity Anisotropy Versus Carbonate Concentration.....	91
Figure 2.21 Step Velocity Sum Versus Carbonate Concentration.....	92
Figure 2.22 Period of Spiral Rotation Versus Carbonate Concentration.....	93
Figure 2.23 BCF Dissolution Rate Versus Carbonate Concentration.....	94
 CHAPTER 3.	
Figure 3.1 3D plots of VSI data sets showing progressive surface colonization by <i>Shewanella</i> on dolomite over 35 hours.....	117
Figure 3.2 2D VSI image of <i>Shewanella</i> surface colonization on a magnesite surface after 9 hours.....	119

Figure 3.3 Cross-section measurements of a single <i>Shewanella</i> cell on a dolomite surface and its associated organic material.....	120
Figure 3.4 2D VSI image of entrenched cells on calcite following the removal of associated organic material.....	121
Figure 3.5 The removal of associated organic material revealed the clear presence of <i>Shewanella</i> microcolonies on the calcite surface.....	122
Figure 3.6 The role of mineral-surface microtopography in determining cell attachment on calcite.....	123
Figure 3.7 AFM images of <i>Shewanella</i> surface colonization on a dolomite surface after 35 hours.....	125
Figure 3.8 High-resolution deflection AFM images of <i>Shewanella</i> cells on a dolomite surface.....	126
Figure 3.9 Cross-section of a recently divided cell on a calcite surface.....	127
Figure 3.10 Images showing the extent of dissolution between masked and unmasked areas of a calcite crystal following 4 hours of reaction in the cell-free control solutions.....	129
Figure 3.11 Images showing the masked and unmasked regions of a dolomite crystal surface following 4 hours of exposure to <i>Shewanella</i> cells.....	130
Figure 3.12 VSI images showing differences in <i>Shewanella</i> surface colonization on calcite, dolomite and magnesite surfaces after 8 and 35 hours of exposure to microbial cultures.....	133
Figure 3.13 VSI image of <i>Shewanella</i> surface colonization on the calcite surface after 35 hours.....	134
Figure 3.14 VSI data of calcite dissolution relative to masked	

portions of the crystal surface after 35 hours of exposure to cell-free controls and <i>Shewanella</i> cell cultures.....	136
Figure 3.15 VSI images of surface colonization on barite and dolomite surfaces after 4 hours.....	138
Figure 3.16 AFM image of pre-etched dolomite surface revealing extremely rough surface steps that are not observable using VSI.....	140
Figure 3.17 AFM images of cell attachment on pre-etched dolomite and barite surfaces.....	142

CHAPTER 4.

Figure 4.1 MR-1 biofilm morphology and development on dolomite.....	157
Figure 4.2 Occasionally, initial surface colonization appeared to occur through microcolony formation.....	158
Figure 4.3 2D VSI image of MR-1 surface colonization on a dolomite surface after 9 hours.....	159
Figure 4.4 Cross-section measurements of a single MR-1 cell on a dolomite surface and its associated organic material.....	160
Figure 4.5 MR-1 surface colonization on calcite after 2 hours exposure to MR-1 in the 10% LB medium.....	161
Figure 4.6 Images showing the extent of dissolution between masked and unmasked areas of a calcite crystal following 4 hours of reaction in the cell-free control solutions (low-nutrient medium).....	163
Figure 4.7 Calcite dissolution relative to masked portions of the crystal surface after 8 hours of exposure to cell-free controls and MR-1 cell cultures in the 10% LB medium.....	165
Figure 4.8 Calcite dissolution relative to masked portions of the	

crystal surface after 33.5 hours of exposure to cell-free controls and MR-1 cell cultures in the low-nutrient medium.....	166
Figure 4.9 Images showing the masked and unmasked regions of a dolomite crystal surface following 4 hours of exposure to MR-1 cells in the low-nutrient medium.....	169
Figure 4.10 Images showing the masked and unmasked regions of a calcite crystal surface following 4 hours exposure to MR-1 cells in the 10% LB medium.....	170
Figure 4.11 Microbial trenches on the carbonate surface, indicating that MR-1 colonizes through irreversible attachment	171
Figure 4.12 AFM Images of calcite in the context of MR-1 Attachment.....	173
Figure 4.13 Topographic profiles of trenches produced by dividing or polarly attached cells.	174
Figure 4.14 3-D Plot of a MR-1 cell (top) and a microbial trench (bottom) on dolomite after 8 hours exposure to MR-1 in the low-nutrient medium.....	175

GENERAL INTRODUCTION

Carbonate minerals are principal components of biomineralizing systems and play a central role in a number of important biogeochemical cycles. In particular, the relative rates of calcite (CaCO_3) precipitation and dissolution determine the preservation and subsequent accumulation of carbonate in the geologic record as well as the sequestration of several co-precipitated trace elements. Accordingly, a thorough understanding of calcite growth and dissolution rates is critical to the successful modeling of the global carbon cycle and its use in predicting the fate of fossil fuel carbon dioxide. Most rate laws describing the growth and dissolution of natural crystals, including calcite, have been focused on the saturation-state dependence of mineral growth and dissolution. The clear benefit of these rate expressions is that they allow the use of easily measured bulk chemistry parameters for rate-prediction and extrapolation. While equilibrium requires that there must be a dependence of the rate on ΔG , assumptions involving rate dependence on ΔG , and hence saturation state, are not based upon mechanistic kinetic theory (Lasaga & Lüttge, 2005). Kinetic models for mineral reaction rates rigorously involve the arrival and departure of molecular units which are independently controlled by their respective concentrations and their binding at the surface. It follows that nonstoichiometric solutions, where the concentration ratio of lattice ions does not correspond to the stoichiometry of the mineral, may significantly modify growth and dissolution kinetics. Unfortunately, current concentration-based rate laws do not allow for mechanistic differences in rate resulting from nonstoichiometric solutions with varying cation/anion ratios. In addition to the complexities offered by nonstoichiometric solutions, natural systems offer several other obstacles to accurate rate prediction. In

fact, much of contemporary geochemistry has been focused on deciphering the remaining complexities exhibited by natural systems and the resultant difficulties in extending laboratory-derived rates to the accurate prediction of their behavior. In order to address the complexities of natural systems, two specialized sub-fields have emerged over the last several decades: mineral-surface geochemistry and geomicrobiology. Mineral-surface geochemistry may be seen as having originated with the original Burton, Cabrera, Frank (BCF) theory (Burton et al., 1951) that provided a quantitative theoretical explanation for the way in which growth and dissolution rates are enhanced by defects on imperfect surfaces. Ever since this postulation, it has been known that surfaces play an important role in determining solid-phase reaction rates and mineral-surface geochemists have accordingly argued that surface-structure and surface-dependent processes dominate the behavior of many natural systems. Concurrently, geomicrobiologists frequently persuade that the abiotic processes that occur on mineral surfaces in the laboratory are not representative of natural systems which are often dominated by biological processes. Instead, natural growth and dissolution rates can only be understood in the context of microbial interactions with mineral-surfaces and coincident biologically-induced changes in solution chemistry. Fortunately, the development of surface-sensitive techniques such as atomic force microscopy (AFM) and vertical scanning interferometry (VSI) over the last two decades has provided a window into the world of mineral-surfaces and critical biological interfaces, that has allowed for rapid exploration of these two emergent fields. Here we use the complementary surface techniques, AFM and VSI, to investigate the interrelationships of solution stoichiometry, microbial attachment, and surface-dependent mechanisms in determining calcite growth and dissolution rates, independent of

saturation state. Our results, confirmed at multiple length-scales, demonstrate that all three of these parameters play primary and determinant roles in the growth and dissolution of calcite in the context of constant saturation state. In so doing, the combined results of our experiments elucidate many of the important underlying mechanisms by which changes in carbonate solution chemistry and microbial attachment may mediate calcite growth and dissolution in natural systems.

CHAPTER 1. The Role of $\text{Ca}^{2+}/\text{CO}_3^{2-}$ Ratio in Calcite Growth: Mechanistic Insight into Biomineralization and Consequences of Nonstoichiometric Solutions for Concentration-Based Rate Laws

Abstract

Biomineralization and crystal growth studies typically normalize precipitation kinetics to the ion activity product (IAP), especially in the form of supersaturation expressions. However, concentration-based rate laws do not allow for mechanistic differences in rate resulting from nonstoichiometric solutions with varying cation/anion ratios. Here we present molecular-scale evidence, confirmed at multiple length-scales, that the $\text{Ca}^{2+}/\text{CO}_3^{2-}$ ratio of carbonate solutions, at constant saturation, determines both the kinetics and anisotropy of step advancement. Anisotropic step velocities, in turn, alter step generation rates at screw dislocations, thereby significantly affecting the overall growth rate of calcite surfaces. These results reflect different mechanistic roles for the cation and anion during growth and suggests limitations on the application of concentration-based rate laws in solutions of varying ionic ratios. Further, this study offers clear demonstration that the crystal surface exerts a primary control on growth rate through step-specific and defect-directed interactions, producing differences in rate that could not be predicted from considerations of bulk chemistry alone. Instead, specific knowledge of the surface and its interaction with particular solution-species is required for accurate rate prediction. Finally, the effects of solution stoichiometry on calcite growth demonstrated in this study, suggest that biological control over $\text{Ca}^{2+}/\text{CO}_3^{2-}$ ratio may be an underestimated factor in carbonate biomineralization strategies.

1.1 Introduction

1.1.1 Concentration-Based Rate Laws and Solution Stoichiometry

Classical crystal growth theory relates the rate of precipitation to the ion activity product (IAP), especially in the form of supersaturation (Ω) expressions,

$$\Omega = \frac{\text{IAP}}{K_{\text{sp}}}$$

where K_{sp} is the solubility product. Since $\Omega = \exp(\Delta G/RT)$, the degree of supersaturation reflects the thermodynamic driving force for crystallization and carries the general expectation that as saturation state increases, so does the rate of precipitation.

Accordingly, numerous theoretical and empirical rate expressions have been developed that relate the kinetics of crystallization to the concentration of reactants (see Table 1.1). All of these overall or elementary rate laws exhibit a dependence on ΔG , or the saturation state. However, the ion activity product, or saturation state, does not uniquely describe the chemical speciation of a solution. To the contrary, nearly an infinite number of unique solutions could be prepared for any given saturation state. Consider, for instance, the ubiquitous calcium carbonate system. Two end-member solutions could be constructed with the same ion activity product or saturation state, but with very different solution chemistries. One solution could have a high cation/anion ($\text{Ca}^{2+}/\text{CO}_3^{2-}$) ratio while the other solution may exhibit a high anion/cation ($\text{CO}_3^{2-}/\text{Ca}^{2+}$) ratio. Nevertheless, none of the rate expressions commonly used for calcium carbonate crystallization (refer to Table 1.1) makes an allowance for differences in solution stoichiometry, despite the

Table 1.1 – Theoretical and Empirical Rate Expressions for Precipitation from Solution

General Precipitation Rate Laws for Surface-Controlled Crystallization (Nielsen, 1983)	
$R \propto (\Omega - 1)$	limited by adsorption
$R \propto (\Omega - 1)^2$	limited by spiral growth at screw dislocation
$R \propto \exp\left(-\frac{K}{\ln \Omega}\right)$	limited by two-dimensional nucleation
Elementary Rate Laws for a Kossel Crystal (Zhang and Nancollas, 1998)	
$R_{\text{kink}} = v(S-1)$	Rate of kink propagation
$R_{\text{step}} = 2av(S-1)S^{1/2}\exp(-\varepsilon/kt)$	Rate of step movement
$R_{\text{spiral}} = k_k(S-1)S^{1/2}\ln S$	Rate of spiral growth
Calcite Precipitation Rate Law that is Linear with Respect to ΔG (Reddy and Nancollas, 1971)	
$R_{\text{ppt}} = k_p[\text{Ca}^{2+}]\text{CO}_3^{2-}]$	Mechanistic model for calcite precipitation
Calcite Precipitation Rate Law that is Nonlinear with Respect to ΔG (Reddy and Nancollas, 1973; Reddy, 1977; Reddy and Gaillard, 1981; House, 1981)	
$R_{\text{ppt}} = k(\Omega - 1)^2$	Adopted for calcite experiments at 25°C

where $S = ([A]^\alpha[B]^\beta/K_s)^{1/(\alpha+\beta)}$, a is the atomic size and v is the attachment/detachment frequency

strong potential for solutions with different solution compositions to exhibit different precipitation rates. This limitation in kinetic description is especially troublesome given that natural solutions are likely to exhibit nonstoichiometric solution chemistries, where the concentrations of the lattice ions do not correspond to the stoichiometry of the mineral lattice.

1.1.2 Kinetic Expectations for Nonstoichiometric Solutions

Most crystal growth theories have been developed using a simple cubic lattice, called the Kossel model (Kossel, 1927), which recognizes the importance of kink sites as the primary attachment sites for growth units. In this model, growth proceeds by the successive attachment of growth units at a kink until a row is completed (refer to Fig. 1.1). New rows are begun by the attachment of a growth unit at a non-kink site, following initial diffusion to the surface and translation to a step-edge. While this model only considers one type of growth unit, it has nevertheless been applied to the growth and dissolution kinetics of AB electrolyte crystals. In such cases, the lattice ions are considered to form a single kinetic entity, AB . The rates of kink propagation, step movement, and dislocation-controlled growth are then generally expressed in terms of the saturation state, which is related to the thermodynamic driving force for growth (see Table 1.1). However, these equations based upon the Kossel lattice, only allow for the presence of one type of kink site, while simple ionic crystals (*e.g.* AB lattices) have two possible types of kink sites: one terminating with an anion and one terminating with a cation. Since any understanding of the dependence of growth rate on solution stoichiometry must ultimately involve the interaction of solution species with kinks

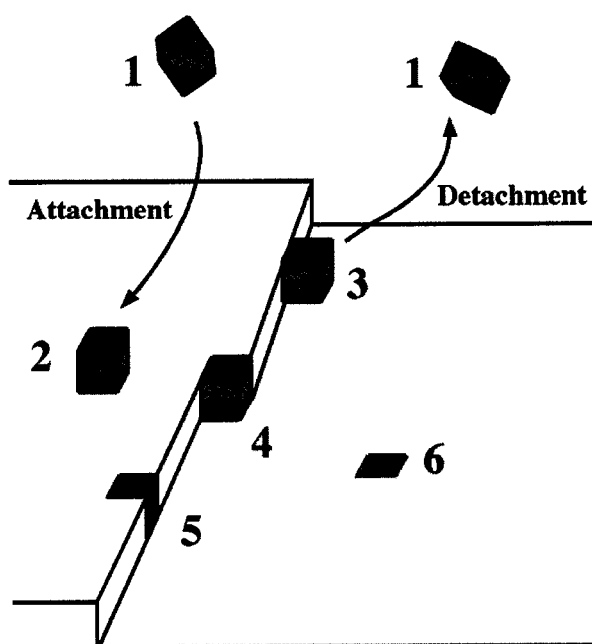


Figure 1.1 – Important Interactions of Growth Units with the Surface of an Idealized Kossel Crystal

(1) Free Growth Unit in Solution; (2) Atom Adsorbed on the Crystal Face [*1 saturated bond*]; (3) Atom Adsorbed at the Step Edge [*2 saturated bonds*]; (4) Atom Attached to a Kink Site ("Half-Crystal Position") [*3 saturated bonds*]; (5) Atom Embedded in a Step Edge [*4 saturated bonds*]; (6) Atom Embedded into the Outermost Crystal Plane [*5 saturated bonds*]

terminating with anions and cations, it is necessary to consider non-Kossel kinetic growth models. In such models, the frequencies of attachment and detachment of cations/anions at specific kink sites would be expected to be elementary crystal growth parameters that determine the precipitation rate. Further, these frequencies should depend on the concentrations of components in solution, and therefore the stoichiometric ratio of reactants. However, empirical observations of such phenomena are difficult. Nevertheless, some kinetic expectations for the effect of solution stoichiometry on crystal growth rates may be formed from theoretical models and from empirical observations of the motion of monomolecular steps exposed to different solution chemistries.

Zhang and Nancollas (1998) used a kink creation – propagation – collision (CPC) model to calculate the rates of step movement for different solution stoichiometries on a NaCl lattice under nonequilibrium conditions. The authors determined that the rate could not be defined solely in terms of the ionic activity product but also depended on the activity ratio (solution stoichiometry) and the relative integration frequencies of the lattice ions as well. At a given thermodynamic driving force, a maximum rate occurred at a certain ratio of lattice ion activities. If the role of the cation and anion during growth are precisely the same, then the maximum rate would be expected to occur at an activity ratio of one. However, geochemists commonly postulate different roles for the cation and anion during growth based upon aqueous solution thermodynamics. For instance, cation dehydration has been widely considered as a possible rate-limiting step during crystal growth due to the much higher dehydration energy characteristic of cations as compared to anions. Accordingly, a kinetic advantage for growth might be anticipated for solutions exhibiting excess cations at a given saturation state. A recent experimental

study tested this hypothesis by measuring the dependence of step velocities on solution stoichiometry for the growth of calcium oxalate monohydrate ($\text{CaC}_2\text{O}_4 \cdot \text{H}_2\text{O}$) using atomic force microscopy (AFM) (Chernov et al., 2006). The authors determined that the growth rate was highest when the solution concentration ratio equaled one and decreased symmetrically with increasing or decreasing concentration ratios ($\text{Ca}^{2+}/\text{C}_2\text{O}_4^{2-}$). This behavior is consistent with the kink growth rate theory for non-Kossel crystals only if the frequency factors for attachment to kink sites are the same for the cation and anion. Therefore, this study observed the kinetic limitation on growth imposed by the stoichiometric ratio that was predicted by Zhang and Nancollas (1998), but did not observe a differential kinetic role for the cation and anion during calcium oxalate monohydrate growth. Nevertheless, it is critical that the aforementioned kinetic expectations be tested for key natural systems where nonstoichiometric solutions are the rule.

1.1.3 Potential Consequences of Nonstoichiometric Solutions for Calcium Carbonate Biomineralization

Perhaps no natural system is more important or more interesting in terms of the potential role of solution stoichiometry than the calcium carbonate system. Calcium carbonate (CaCO_3) precipitates from seawater largely as a result of biomineralization processes and plays a central role in a number of important biogeochemical cycles. The accumulation of carbonate in the geologic record is an important component of the global carbon cycle and a thorough understanding of carbonate growth and dissolution rates is fundamental to predicting the fate of fossil fuel carbon dioxide (Morse, 1983; Morse &

Mackenzie, 1990; Morse & Arvidson, 2002). More importantly, the incorporation of stable isotopes and trace elements in biogenic calcite are used as indicators of past environments. However, the interpretation of these environmental signals is complicated by the “vital effect”, or the overprint by biological processes on isotopic and elemental partitioning during biomineralization. A further complication in understanding this system is that the $\text{Ca}^{2+}/\text{CO}_3^{2-}$ ratio of seawater is highly nonstoichiometric. The $\text{Ca}^{2+}/\text{CO}_3^{2-}$ ratio of surface ocean waters is on the order of 100 (Zeebe and Westbroek, 2003), while in marine pore waters the ratio may be as high as 2000 (Cai et al., 2000; Mueller et al., 2003; Jahnke & Jahnke, 2004). The stoichiometric ratio of seawater is also spatially variable, as the balance between productivity and calcium carbonate dissolution rates governs the localized alkalinity. The resulting variations in seawater carbonate ion concentration ($\text{Ca}^{2+}/\text{CO}_3^{2-}$ ratio) are increasingly being shown to play a role in the trace element and isotopic composition of some biominerals (Spero et al., 1997; Spero et al., 1999; Russell & Spero, 2000; Russell et al., 2004; Elderfield et al., 2006; Rosenthal et al., 2006). The presence of this carbonate ion effect (CIE) offers tangible empirical evidence that the solution stoichiometry of seawater plays an important role during biomineral formation. Paleoenvironmental reconstruction over much longer periods of time is further complicated by recent evidence that suggests that the stoichiometric ratio of seawater has changed dramatically during the geologic past. Systematic changes in the fluid inclusions of marine halites suggest that seawater chemistry has oscillated dramatically during the Phanerozoic due to changes in seafloor spreading rates (Lowenstein et al., 2001). These oscillations in seawater chemistry produced changes in the primary calcium carbonate mineralogy precipitated from

seawater as manifested by the alternating ‘aragonite seas’ and ‘calcite seas’ evident in the rock record. While the importance of this work is usually cast in terms of changes in the $\text{Mg}^{2+}/\text{Ca}^{2+}$ ratio, the $\text{Ca}^{2+}/\text{CO}_3^{2-}$ ratio of seawater changed concurrently. This oscillation in seawater chemistry has been implicated as a potentially important selective pressure during the evolution of biomineralizing organisms and makes paleoenvironmental reconstruction over longer periods of geologic time increasingly suspect (Stanley & Hardie, 1998; Stanley & Hardie, 1999).

Biominerals do not form directly from seawater but rather in a microenvironment that is under either the active or passive control of the organism. Here the $\text{Ca}^{2+}/\text{CO}_3^{2-}$ ratio of the solutions from which biominerals form is likely to be mediated by metabolic activity, photosynthesis, proton pumps and ion selective membrane channels.

Accordingly, there is considerable opportunity within biological systems for changes in the stoichiometric ratio to play an important role during biomineral growth.

Unfortunately, there remains no predictive capacity for understanding the intertwined roles of seawater chemistry and biological processes in determining the composition of biominerals and its impact on paleoenvironmental signals. Especially unclear is the fundamental relationship between solution stoichiometry ($\text{Ca}^{2+}/\text{CO}_3^{2-}$ ratio) and calcium carbonate growth kinetics, morphological development and impurity partitioning. Given the considerable biological potential for mediating the $\text{Ca}^{2+}/\text{CO}_3^{2-}$ ratio at the site of mineralization, several key questions emerge that deserve further scientific inquiry: Is it possible that a major source of the complexity encountered in trying to understand biomineralization processes and biogenic proxies is related to local differences in the $\text{Ca}^{2+}/\text{CO}_3^{2-}$ ratio at the site of mineralization? Can some biogenic controls be ultimately

reduced to inorganic control exerted by the organism over $\text{Ca}^{2+}/\text{CO}_3^{2-}$ ratio in a microenvironment? Are these differences in $\text{Ca}^{2+}/\text{CO}_3^{2-}$ ratio the principal vital effect?

The first step for testing these hypotheses is to determine the effect of the stoichiometric ratio on abiotic calcite growth. Unfortunately, the effect of solution stoichiometry on calcite growth is difficult to ascertain from previous laboratory investigations because the experimental designs that were employed used either fixed stoichiometric ratios or ratios that tended to covary with the saturation state. Therefore, in order to further the understanding of calcite growth from nonstoichiometric solutions, we present here kinetic data collected at multiple length-scales that demonstrates for the first time the precise role of solution stoichiometry in calcite growth. Our results show that the $\text{Ca}^{2+}/\text{CO}_3^{2-}$ ratio of carbonate solutions, at constant saturation, determines both the kinetics and anisotropy of step advancement on the calcite surface. These coupled effects on step dynamics were found to produce significant changes in the overall growth rate of calcite surfaces that depended on the specific $\text{Ca}^{2+}/\text{CO}_3^{2-}$ solution ratio, indicating a differential mechanistic role for that cation and anion during growth. These results suggest that the application of concentration-based rate laws in solutions of varying ionic ratios is limited and that biological control over solution stoichiometry may indeed be an important factor in understanding the vital effect in carbonate biominerals. Our experimental results were made possible through the use of surface imaging techniques that allowed for the measurement of fundamental crystal growth parameters over the short empirical timescales required to maintain precise control over solution chemistry, that in turn allowed for the decoupling of the roles of solution stoichiometry and saturation state.

1.1.4 Step-Specific Measurements on the Calcite Cleavage Surface

In order to understand the influence of solution stoichiometry on the rate of crystal growth, the motion and structure of elementary steps on the crystal surface must be taken into account. Fortunately, an experimental technique exists that allows for the observation of step dynamics in the context of step-edge structure. Atomic force microscopy (AFM) provides high-resolution images of monomolecular steps on surfaces, thereby allowing for the direct measurement of reaction rates and processes without extrapolating from changes in bulk chemistry. Because these measurements occur in real-time and under flow-through conditions, the effects of changes in solution chemistry are observed immediately, which allows for more exquisite chemical control and working at the lower saturation states characteristic of natural systems. The near molecular-scale resolution of AFM also allows for the isolation of particular growth mechanisms. Especially useful are growth spirals emanating from screw dislocations on the calcite cleavage surface. Dislocations are thought to govern growth at the low saturation states common in natural systems and the growth hillocks that they produce provide a collection of steps that are convenient for measuring the fundamental parameters of crystal growth.

Layer-by-layer growth on the $(10\bar{1}4)$ calcite surface proceeds by the migration of atomically flat steps generated at screw dislocations. The advancement of these 3.1 Å monomolecular steps results in the formation of polygonal growth hillocks that reflect the symmetry of the face (Fig. 1.2). Each growth hillock exhibits four well-formed vicinal faces. Each vicinal face is in turn comprised of straight growth steps of like orientation that run parallel to periodic bond chains (PBCs) in the calcite lattice (Reeder & Rakovan,

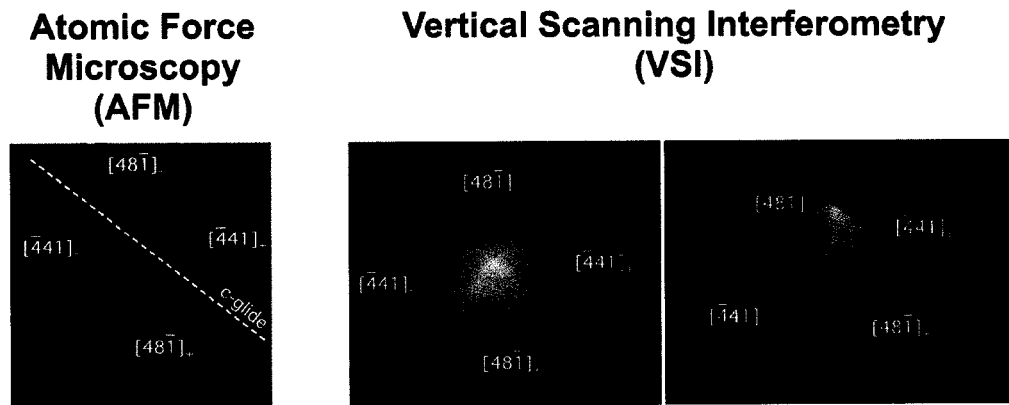


Figure 1.2 – Calcite Growth Hillocks Showing Anisotropy

AFM and VSI images of calcite growth hillocks showing crystallographic orientation. These representations show the difference in resolution characteristic of the two techniques. The AFM image has a scan size of $3 \times 3 \mu\text{m}$ while the VSI scan size is $38 \times 33 \mu\text{m}$.

1999). The *c*-glide plane generates two distinct pairs of crystallographically identical steps, denoted as the positive ($[\bar{4}41]_+$ and $[48\bar{1}]_+$) and negative directions ($[\bar{4}41]_-$ and $[48\bar{1}]_-$) (Fig. 1.3). These two step-types have non-equivalent step-edge geometries and kink-site structures because of differences in the orientation of exposed carbonate groups (Reeder & Rakovan, 1999). The tilt of the carbonate anions cause the ‘positive steps’ to exhibit a step-edge geometry that is obtuse with respect to the cleavage plane, while the ‘negative steps’ form an acute angle with the cleavage surface. This anisotropy in step-edge structure often results in differential step velocities for the two step-types and accounts for the non-equivalent terrace widths evident on many growth hillocks (i.e., Figs. 1.2 and 1.3). Accordingly, the anisotropic growth condition is common for calcite, whereby one step-type moves significantly faster than the other step-type and thus is responsible for a greater amount of new CaCO_3 deposition. In the absence of step velocity measurements for the two step-types, the anisotropy of a growth hillock can be determined by measuring the angle (ϕ) created by the intersection of the positive (+) and negative (-) step-types (Fig. 1.4). For instance, when $\phi > 180^\circ$, the (-) steps travel at a faster rate than the (+) steps and account for the majority of growth. Conversely, when $\phi < 180^\circ$ the (+) steps travel at a faster rate than the (-) steps and account for the majority of growth. When $\phi = 180^\circ$, isotropic growth predominates as both step-types travel at the same rate and make equivalent contributions to the growth of new CaCO_3 layers. An important consequence of the anisotropic growth condition (Fig. 1.5) stems from experimental evidence that demonstrates that impurities selectively incorporate into one step-type or another (Paquette & Reeder, 1990; Paquette & Reeder, 1995). This step-specific impurity incorporation results from the stereochemical preference of a given

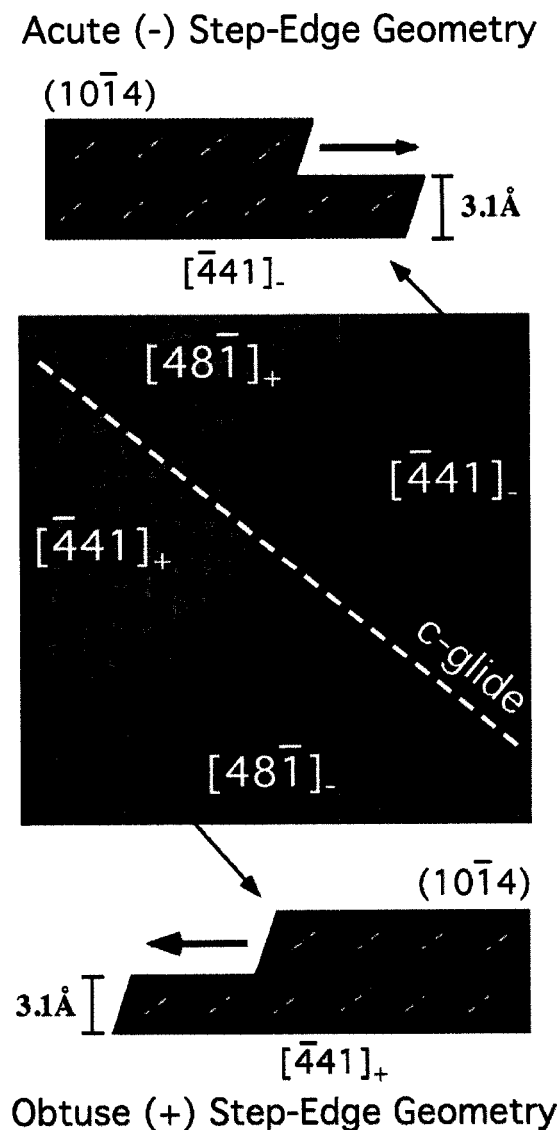


Figure 1.3 – AFM image of a growth spiral emanating from a screw dislocation on the $\{104\}$ cleavage surface of calcite.

The polygonal growth hillock exhibits four vicinal faces that in turn are comprised of two pairs of crystallographically equivalent steps that are reflected across the c -glide plane. These steps, however, have nonequivalent molecular-scale step-edge geometries denoted as the positive ($[\bar{4}41]_+$ and $[48\bar{1}]_+$) and negative ($[\bar{4}41]_-$ and $[48\bar{1}]_-$) step directions. This anisotropy in step-edge structure results in the different terrace widths evident on this growth hillock. The scan size of the AFM image is $3 \times 3 \mu\text{m}$.

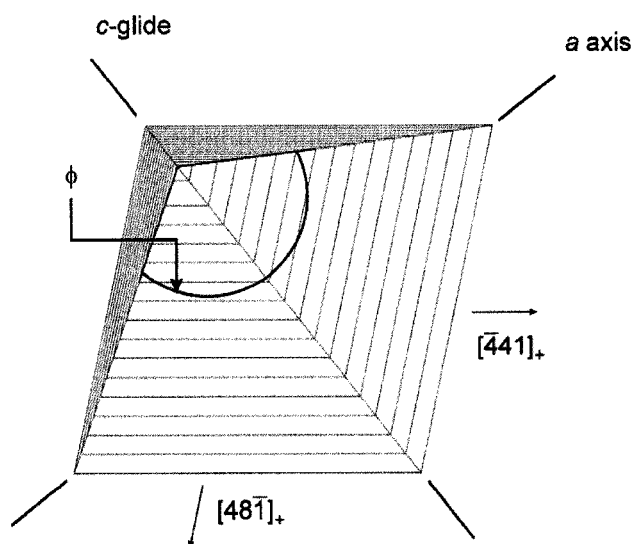


Figure 1.4 – A measure of the anisotropy of a growth hillock (ϕ)

The anisotropy of a growth hillock can be determined by measuring the angle (ϕ) created by the intersection of the positive (+) and negative (-) step-types. When $\phi > 180^\circ$, the (-) steps travel at a faster rate than the (+) steps and account for the majority of growth. Conversely, when $\phi < 180^\circ$ the (+) steps travel at a faster rate than the (-) steps and account for the majority of growth. When $\phi = 180^\circ$, isotropic growth predominates as both step-types travel at the same rate and make equivalent contributions to the growth of new CaCO_3 layers.

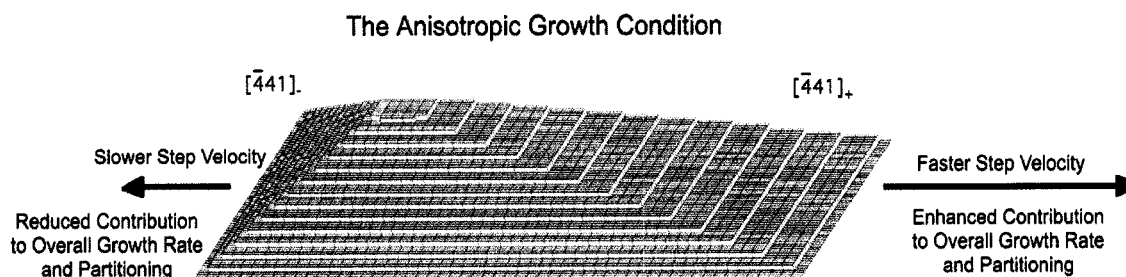


Figure 1.5 – The Anisotropic Growth Condition

During the anisotropic growth condition, one step travels at a faster rate than the other step-type, resulting in differences in the relative contribution of each step to the overall growth rate. Here, the (+) step has a high step velocity and thus accounts for the majority of the deposition of new CaCO_3 layers. Since element partitioning is known to be step-specific, growth anisotropy should produce significant differences in bulk impurity incorporation.

impurity for a particular step-type due to molecular-scale differences in its step-edge structure. In general, species with an ionic radius smaller than Ca prefer to incorporate into the (-) steps, denoted as $[\bar{4}41]_-$ and $[48\bar{1}]_-$. Ionic species that are larger than Ca preferentially incorporate in the (+) steps, $[\bar{4}41]_+$ and $[48\bar{1}]_+$. Since during anisotropic growth, one step-type accounts for a majority of the deposition of new layers, the same factors that affect the anisotropy of growth are also likely to influence impurity partitioning.

Another factor that may affect trace element partitioning in calcite is the kinetics of growth. The partitioning of many elements have been shown to be dependent on the overall growth rate of calcite (Lorens, 1981; Lahann and Siebert, 1982; Morse and Bender, 1990). According to BCF theory (Burton et al., 1951), the surface normal growth rate (R) during spiral growth is equal to the product of the step velocity (v_s) and the hillock slope (ρ):

$$R = v_s \rho$$

Since the hillock slope (ρ) is equal to the monomolecular step height (h) divided by the terrace width (λ), or the distance between adjacent steps on the spiral, the surface normal growth rate can be calculated from measurements of step velocity and terrace width as follows:

$$R = \frac{h}{\lambda} v_s,$$

where the step height (h) for monomolecular steps on the calcite surface is 0.31 nm. In turn, the terrace width is determined by the relative rate by which new steps are created by the dislocation and how fast these steps move away from the dislocation source. The rate of step production can be quantified as the period of spiral rotation (τ) in seconds, which is defined as:

$$\tau = \frac{\lambda}{v_s}$$

In this way, the rate by which layer-by-layer growth occurs during spiral growth can be thought of as being determined by the period of spiral rotation (the rate at which new steps are created) and the velocity of monomolecular surface steps. Importantly, AFM provides for the measurement of these critical kinetic parameters as a function of step-edge structure, enabling an assessment of step-specific interactions between certain step-types and solutions exhibiting different stoichiometries. However, surface maps reveal that the overall growth rate of calcite is the result of the continuous coalescence of numerous growth hillocks (Fig. 1.6). Images such as these indicate that calcite growth cannot be understood solely in terms of AFM observations of a single growth hillock but requires an integrated measurement of calcite growth. This can be accomplished using vertical scanning interferometry (VSI) which provides integrated rate measurements over much larger areas of the crystal surface. The combination of these two surface techniques provides a powerful tool for unraveling the relationship between step-edge structure, growth mechanism and solution stoichiometry that is necessary for achieving a rigorous understanding of calcite growth in nonstoichiometric solutions.

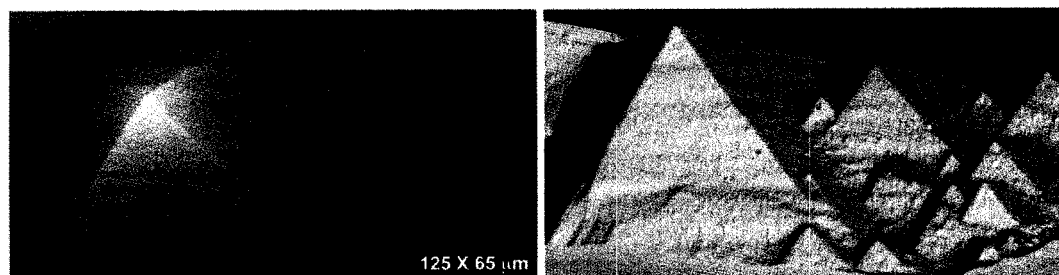


Figure 1.6 – VSI images of a calcite surface following an AFM experiment.

Surface maps reveal that calcite growth proceeds by the continuous coalescence of numerous growth hillocks. Images such as these indicate that calcite growth cannot be understood solely in terms of AFM observations of a single growth hillock but requires an integrated measurement of calcite growth. Left: 2D topographic VSI image Right: 3D solid model representation of the VSI data file.

1.2 Materials and Methods

1.2.1 Solution Chemistry Modeling

Experimental investigation of the role of solution stoichiometry in calcite growth requires experimental solutions with precisely controlled saturation states and calcium carbonate chemistries. This was achieved using the EQ3NR chemical speciation code (Wolery, 1992) and a specially-designed solution preparation scheme. The recipe for each experimental solution was calculated using the numerical code which implemented the B-dot equation for activity determinations. Solutions of the appropriate saturation were generated by manually adjusting the solubility product (K_{sp}) of calcite used to determine the activities of calcium and carbonate in solution. The remaining model input parameters included total sodium (Na_T) and total chloride (Cl_T). Additionally, the pH of the system was fixed at 8.5.

Solutions with varying Ca^{2+}/CO_3^{2-} concentration ratios at constant saturation state (IAP) were created by changing the relative concentrations of Na_T and Cl_T , thereby forcing the system to electrochemically balance on the Ca^{2+} and CO_3^{2-} ions, while maintaining the constant IAP set by the K_{sp} . In this way, solutions with exact Ca^{2+}/CO_3^{2-} concentration ratios were calculated by adjusting Na_T and Cl_T in the numerical code. The activity (concentration) of Ca^{2+} was solved in the model by setting it equal to the ratio of the desired IAP and carbonate ion activity:

$$a_{Ca^{2+}} = \frac{IAP}{a_{CO_3^{2-}}} = R \ a_{CO_3^{2-}}$$

where R is the desired ratio. Thus, $a_{\text{CO}_3^{2-}} = \sqrt{IAP/R}$. By fixing pH and carbonate ion activity, the two necessary and sufficient constraints on the carbonic acid are met. In practice, the desired ratio (R) was controlled by adding mineral alkalinity in the form of bicarbonate or introducing negative alkalinity through the addition of mineral acid, HCl (see solution preparation below). The solution compositions that satisfied these conditions were computed using EQ3NR and the critical speciation outputs were the activities of Ca^{2+} and CO_3^{2-} , total Ca (Ca_T), ionic strength (I), and the concentration of bicarbonate ion ($m_{\text{HCO}_3^-}$). In these calculations, it was necessary to allow the ionic strength (I) to vary considerably for the lowest $\text{Ca}^{2+}/\text{CO}_3^{2-}$ ratios, since maintaining fixed ionic strength would have only been possible through the addition of a large amount of background electrolyte, which would have in turn complicated the saturation state calculations, particularly at high $\text{Ca}^{2+}/\text{CO}_3^{2-}$ ratios where little carbonate ion is present.

The saturation state (σ , Ω) of each solution was determined using a K_{sp} equal to $10^{-8.48}$, which was calculated from the activities at which measured step velocities went to zero. In Table 1.2 we report the saturation state according to the two formalisms in most common use, where $\Omega = IAP/K_{sp}$ and $\sigma = \ln(IAP/K_{sp}) = \ln\Omega$. While we use Ca^{2+} and CO_3^{2-} activities to compute the saturation state (IAP), we thereafter report the $\text{Ca}^{2+}/\text{CO}_3^{2-}$ ratio as a concentration ratio, since it is the concentration of these species that controls the kinetics of calcite growth. However, it should be noted that the activity coefficients for Ca^{2+} and CO_3^{2-} in this study are nearly identical for all of the experimental solutions employed in this study, and so the reported $\text{Ca}^{2+}/\text{CO}_3^{2-}$ concentration ratios are numerically equivalent to the $\text{Ca}^{2+}/\text{CO}_3^{2-}$ activity ratios for the reported number of digits.

Table 1.2 – Solution Speciation for the Saturation Controls and Ratio Experiments with Preparation Parameters

Solution ID	Calculated by Model (Model Output)						Used to Prepare Solutions				Model Output	
	Ω	σ	$a_{\text{Ca}^{2+}}$	$a_{\text{CO}_3^{2-}}$	$\text{Ca}^{2+}/\text{CO}_3^{2-}$ Ratio	I	+ K _{sp}	pH	Na _T (mol/kg soln)	Cl _T (mol/kg soln)	Ca _T (mol/kg soln)	m _{HCO₃} (mol/kg soln)
control 1-1	6.57	1.88	1.4747x10 ⁻⁴	1.4743x10 ⁻⁴	1.00	0.014	+0.8	8.50	0.0132275	0.00118	2.9632x10 ⁻⁴	1.2x10 ⁻²
control 1-2	10.41	2.34	1.8565x10 ⁻⁴	1.8561x10 ⁻⁴	1.00	0.018	+1.0	8.50	0.017028	0.00162	4.0899x10 ⁻⁴	1.5x10 ⁻²
control 1-3	13.10	2.57	2.0831x10 ⁻⁴	2.0826x10 ⁻⁴	1.00	0.020	+1.1	8.50	0.019347	0.00191	4.8229x10 ⁻⁴	1.7x10 ⁻²
control 2-1	4.14	1.42	1.1711x10 ⁻⁴	1.1711x10 ⁻⁴	1.00	0.011	+0.6	8.50	0.01055	0.0011	2.1738x10 ⁻⁴	9.3x10 ⁻³
control 2-2	6.57	1.88	1.4747x10 ⁻⁴	1.4743x10 ⁻⁴	1.00	0.014	+0.8	8.50	0.0132275	0.00118	2.9632x10 ⁻⁴	1.2x10 ⁻²
control 2-3	10.41	2.34	1.8565x10 ⁻⁴	1.8561x10 ⁻⁴	1.00	0.018	+1.0	8.50	0.017028	0.00162	4.0899x10 ⁻⁴	1.5x10 ⁻²
control 2-4	16.49	2.80	2.3367x10 ⁻⁴	2.3372x10 ⁻⁴	1.00	0.023	+1.2	8.50	0.022	0.00225	5.7002x10 ⁻⁴	1.9x10 ⁻²
ratio 1-1	10.40	2.34	1.6649x10 ⁻⁵	2.0692x10 ⁻³	0.0080	0.222	+1.0	8.50	.25	0.0012	1.6263x10 ⁻⁴	2.0x10 ⁻¹
ratio 1-2	10.40	2.34	3.6041x10 ⁻⁵	9.5587x10 ⁻⁴	0.034	0.095	+1.0	8.50	0.1	0.0012	1.9638x10 ⁻⁴	8.6x10 ⁻²
ratio 1-3	10.41	2.34	1.0656x10 ⁻⁴	3.2337x10 ⁻⁴	0.33	0.030	+1.0	8.50	0.03	0.0012	3.0039x10 ⁻⁴	2.7x10 ⁻²
ratio 1-4	10.40	2.34	1.3170x10 ⁻⁴	2.6158x10 ⁻⁴	0.5	0.025	+1.0	8.50	0.0243	0.00157	3.3591x10 ⁻⁴	2.2x10 ⁻²
ratio 1-5	10.41	2.34	1.8565x10 ⁻⁴	1.8561x10 ⁻⁴	1.0	0.018	+1.0	8.50	0.0169	0.0015	4.0853x10 ⁻⁴	1.5x10 ⁻²
ratio 1-6	10.41	2.34	2.6242x10 ⁻⁴	1.3131x10 ⁻⁴	2.0	0.014	+1.0	8.50	0.01235	0.0020695	5.1324x10 ⁻⁴	1.1x10 ⁻²
ratio 1-7	10.41	2.34	4.2209x10 ⁻⁴	8.1639x10 ⁻⁵	5.2	0.010	+1.0	8.50	0.008	0.0025	7.2786x10 ⁻⁴	6.5x10 ⁻³
ratio 1-8	10.41	2.34	1.3083x10 ⁻³	2.6339x10 ⁻⁵	49.6	0.009	+1.0	8.50	0.0033	0.005	2.0191x10 ⁻³	2.1x10 ⁻³
ratio 1-9	10.41	2.34	4.1831x10 ⁻³	8.2376x10 ⁻⁶	506	0.023	+1.0	8.50	0.00125	0.0153	7.4665x10 ⁻³	6.8x10 ⁻⁴

1.2.2 Solution Preparation

Supersaturated growth solutions with precisely controlled $\text{Ca}^{2+}/\text{CO}_3^{2-}$ concentration ratios were prepared using the results from the chemical speciation calculations, including: Na_T , Cl_T , and Ca_T and pH (Table 1.2). In order for the solutions to be electrochemically balanced as modeled, Na_T and Cl_T had to be independently delivered as acid-base pairs instead of as electroneutral salts. Accordingly, Na and Cl were introduced gravimetrically as NaOH (0.9454 mol/kg soln) and HCl (8.9492×10^{-2} mol/kg soln), respectively. Ca_T was delivered gravimetrically as CaCl_2 (0.4658 mol/kg soln). Additionally, each experimental solution had an initial HCO_3^- concentration of 0.001 mol/kg soln, introduced using a NaHCO_3 solution (0.09917 mol/kg soln). The pH of each solution was adjusted to 8.50 by sparging with ultrapure CO_2 or N_2 gas as required. This final step produced solutions with precise $\text{Ca}^{2+}/\text{CO}_3^{2-}$ activity ratios that were stable over the experimental durations employed.

1.2.3 Atomic Force Microscopy (AFM) Experiments

Fluid-cell atomic force microscopy (AFM) was used to make *in situ* observations of calcite crystallization on a seed crystal in a flow-through environment. Single-sourced growth spirals emanating from screw dislocations on the calcite surface were imaged in Contact Mode (Digital Instruments, Santa Barbara) under controlled solution conditions at 25°C. The rate of solution input was adjusted to yield step velocities independent of flow rate, thereby ensuring that growth was not limited by mass transport to the surface. The resultant flow-rate of 30 mL/hr yielded a residence time of approximately 6 seconds

in the 50 μL fluid-cell. Monomolecular step velocities (v_s) and terrace widths (λ) were directly measured on growth spirals as a function of saturation state or stoichiometric ratio. Step velocity measurements represent step displacement from a fixed reference point (i.e., the dislocation source) per unit time. The most accurate measurements of step velocity using AFM are achieved by adjusting the scan angle to orient the step train parallel to the y axis and then disabling the slow scan direction over the center of the spiral (Land et al., 1997). The resultant images record the movement of steps as the evolution of individual points at step-edges over the imaging area as shown in Fig. 1.7. Using the measured angle (θ), v_s was then calculated for the step trains on both sides of the hillock (the two step directions) by an equation derived from trigonometry:

$$v_s = \frac{Sr \times A}{N \times} \tan \theta$$

where Sr is the scan rate (lines/sec, 5.80-12.20 Hz in this study), A is the scan length (5 μm for this study), and N the sampling rate (lines/scan, 512 in this study). A minimum of six images were captured in continuous mode for the determination of step velocities by image analysis. Terrace widths (λ) were determined by measuring the distance between adjacent steps on the growth spiral.

1.2.4 Vertical Scanning Interferometry (VSI) Experiments

Surface normal calcite growth rates were measured using vertical scanning interferometry (VSI) in the same solutions used for determining the step-specific AFM rates. The

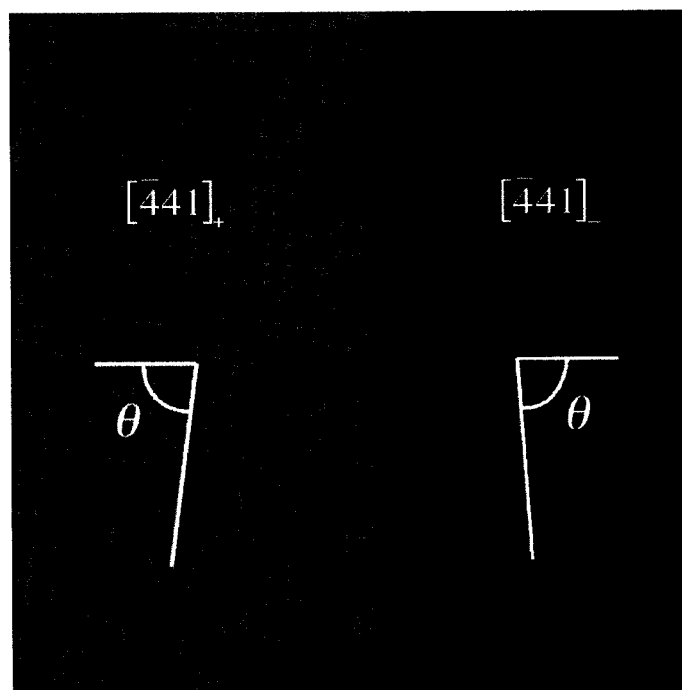


Figure 1.7 – Measuring the Advancement of Individual Monomolecular Steps Relative to the y Scan Direction.

The measured angle (θ) from images such as these were used to calculate step velocity. Smaller angles indicate faster step velocities. Scan size is $5 \times 5 \mu\text{m}$.

longer-term VSI experiments were designed to match as close as possible those conditions employed during the AFM experiments. A single calcite cleavage rhomb was mounted within an AFM fluid-cell that was in turn attached to a large-capacity syringe pump. Each growth experiment ran approximately 13.5 hours with a flow-rate equivalent to the AFM experiments (30 mL/hr). The construction of the syringe pump prevented gas exchange between the atmosphere and the solution reservoir during the course of the experiment. Following each experiment, measurements of surface normal growth were measured using a commercially-available MicroXAM MP-8 (ADE Phase-shift, Tucson, AZ) vertical scanning interferometer (VSI), equipped with 10x and 50x Nikon Mirau objectives. The manner by which this instrument creates topographic images of the surface are described in detail elsewhere (Lüttge et al., 1999). The 10x interferometric objective yields a 845 x 630 μm field of view, while the 50x objective allows for scan sizes of 165 x 125 μm . Images made at 50x magnification using white-light illumination provide a lateral resolution of $\sim 0.5 \mu\text{m}$, while maintaining a vertical resolution (i.e., step height) on the order of 1-2 nm. There are two basic types of images that can be generated from data sets acquired using VSI. The standard data file is a 2-dimensional (2D) topographic image similar to height images obtained using AFM, where topographic information is conveyed according to a color scale. In these images, bright colors typically indicate higher surface features on the image. The second image type used in this study is a 3-dimensional (3D) solid-model representation of the topographic information contained in the VSI data file.

Interferometry measures relative surface height. By placing an inert mask on the surface and measuring the average height difference between the unreacted and reacted

surfaces, an absolute value of surface normal retreat may be determined. Thus, during dissolution, changes in average height $\Delta\bar{h}$ made at time intervals Δt yields a surface normal retreat velocity, $v_{[hkl]}$:

$$\frac{\Delta\bar{h}}{\Delta t} = v_{[hkl]}.$$

Dividing this velocity by the molar volume \bar{V} (cm³/mol) gives a global dissolution rate in the familiar units of moles per unit area per unit time:

$$r = v_{[hkl]} \bar{V}^{-1}.$$

This approach allows a simple and straightforward calculation of surface-area rates from measurements of average surface heights ($\Delta\bar{h}$) (e.g., Lüttge et al., 1999). At least two reference masks were applied to each crystal surface prior to reaction and allowed to cure for 24 hours. The masks used in this study were made using Permatex (www.permatex.com), a commercially-available high-temperature silicone gasket making compound. This type of mask has previously been used in abiotic calcite dissolution experiments where it was found to have no measureable effect on solution chemistry or observed rates (e.g., Arvidson et al., 2003).

1.3 Results and Discussion

1.3.1 Saturation Controls: The Role of Saturation State in Anisotropy

In order to understand how changes in $\text{Ca}^{2+}/\text{CO}_3^{2-}$ concentration ratio at constant saturation affect calcite growth, one must first know the precise role that the saturation state itself plays in determining calcite growth. It is well-known that increasing the saturation state increases the step velocities of both step-types, the period of spiral rotation, and the overall growth rate of calcite. However, it has also been previously reported that the *anisotropy* of calcite growth hillocks is determined by the saturation state (Teng et al., 1999). Teng et al. (1999) determined calcite growth anisotropy through the measurement of relative step velocities of the two step-types, resulting in different hillock geometries as manifested by changes in ϕ (the angle created by the intersection of the positive (+) and negative (-) step-types). At higher saturation states, the velocity of the positive (+) step-types was greater than that of the negative (-) step-types ($v_+ > v_-$), and ϕ was greater than 180° . At lower saturation states, the step velocities became isotropic ($v_+ \approx v_-$) and ϕ approached 180° . At saturation states that were even closer to equilibrium, an interesting phenomenon occurred: the hillock geometry reversed due to negative (-) step velocities outpacing positive (+) step movement ($v_+ < v_-$), causing ϕ to be greater than 180° .

A necessary experimental first step in understanding the effect of solution stoichiometry on calcite growth was to re-test the Teng et al. (1999) finding using our novel set of precisely-controlled experimental solutions. The collected data also serves as a saturation control for subsequent $\text{Ca}^{2+}/\text{CO}_3^{2-}$ concentration ratio experiments.

Accordingly, calcite growth hillocks were grown under a wide range of different saturation states while maintaining a constant $\text{Ca}^{2+}/\text{CO}_3^{2-}$ concentration ratio equal to 1 (Fig. 1.8). Two different experimental series were conducted under different laboratory conditions and for different calcite crystals (Table 1.3). These two experimental series varied in the absolute magnitude of their measured step velocities, due to pronounced differences in the ambient temperature conditions in the laboratory during the experiments. However, the general trend with increasing saturation for the two experimental runs was the same. As the saturation of the experimental solutions increased, the step velocities of both step-types increased and the period of spiral rotation decreased (step generation rate increased). The measured terrace widths for the two step-types also decreased with increasing saturation as the rate of spiral rotation increased relative to the rate of increase in step speeds. Therefore, both the step velocities and slope of the hillock increased with increasing saturation, resulting in a greater calculated BCF growth rate for the hillock. Collectively, these measurements are the expected results for the behavior of a growth hillock as the saturation state, or the thermodynamic driving force for crystallization is increased.

The effect of saturation state on step-velocity anisotropy (and growth hillock anisotropy) was also clearly demonstrated by these experimental series of varying saturation state at constant $\text{Ca}^{2+}/\text{CO}_3^{2-}$ concentration ratio (Fig. 1.8). The results of these molecular-scale AFM studies demonstrated a surprisingly mild dependence of step velocity anisotropy, and its dependent hillock geometry (ϕ), on the saturation state. In the two series, ϕ changed from 158° to 164° and from 174° to 178° , while the saturation state was strongly varied. In general, ϕ was determined to be a poor indicator of step velocity

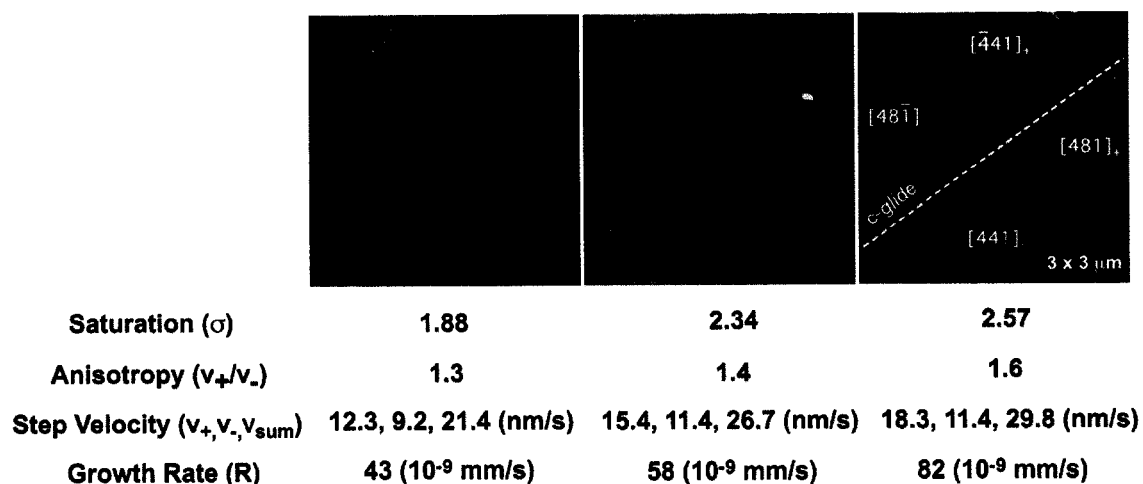


Figure 1.8 – Calcite Growth Hillocks Grown Under Different Saturation States at Constant $\text{Ca}^{2+}/\text{CO}_3^{2-}$ Concentration Ratio Equal to 1.

Saturation state controls demonstrated only a moderate dependence of anisotropy on the saturation state.

Table 1.3 – AFM Data for the Saturation Controls and Ratio Experiments

Solution ID	σ	$\text{Ca}^{2+}/\text{CO}_3^{2-}$ Ratio	ϕ	Terrace Width (nm)			Step Velocity (nm/s)			Period (s)	Slope ($\times 10^{-3}$)		BCF Rate ($\times 10^{-9}$ nm/s)		
				λ_+	λ_-	λ_+/λ_-	v_+	v_-	v_+/v_-		ρ_+	ρ_-	R_+	R_-	R_{avg}
control 1-1	1.88	1.0	164	89	68	1.3	12.3	9.2	1.3	21.4	3.5	4.6	43	42	43
control 1-2	2.34	1.0	163	83	60	1.4	15.4	11.4	1.4	26.7	3.7	5.2	57	59	58
control 1-3	2.57	1.0	158	71	43	1.7	18.3	11.4	1.6	29.8	4.4	7.2	81	82	82
control 2-1	1.42	1.0	178	138	137	1.0	2.9	3.0	1.0	5.9	2.2	2.3	6	7	7
control 2-2	1.88	1.0	176	120	114	1.1	4.4	4.1	1.1	8.5	2.6	2.7	11	11	11
control 2-3	2.34	1.0	178	101	93	1.1	8.1	7.9	1.0	15.9	3.1	3.3	25	26	26
control 2-4	2.80	1.0	174	94	74	1.3	10.6	8.7	1.2	19.2	3.9	5.0	41	44	43
ratio 1-1	2.34	0.0080	171*	58	61	1.0	3.8	4.2	0.9	8.1	5.3	5.1	20	21	21
ratio 1-2	2.34	0.038	172*	65	65	1.0	6.5	6.6	1.0	13.1	4.8	4.8	31	32	32
ratio 1-3	2.34	0.33	180	98	98	1.0	6.7	6.6	1.0	13.3	3.2	3.2	21	21	21
ratio 1-4	2.34	0.5	178	81	84	1.0	8.2	7.4	1.1	15.6	3.8	3.7	31	27	29
ratio 1-5	2.34	1.0	174	108	85	1.3	11.1	8.6	1.3	19.7	2.9	3.6	32	31	32
ratio 1-6	2.34	2.0	168	100	71	1.4	9.0	5.4	1.7	14.5	3.1	4.4	28	24	26
ratio 1-7	2.34	5.2	121	161	59	2.7	9.0	3.3	2.7	12.3	1.9	5.3	17	17	17
ratio 1-8	2.34	49.7	116	173	38	4.6	6.5	1.4	4.5	7.9	1.8	8.2	12	11	12
ratio 1-9	2.34	507.8	107	219	38	5.8	6.1	1.2	5.1	7.2	1.4	8.2	9	10	10

anisotropy, since it is likely affected by the geometry of the dislocation source. Instead, the simple velocity ratio of the two step-types (v_+/v_-) was chosen as a better observational quantity that directly described the anisotropy of step velocities that produced changes in hillock geometry. As the saturation state increased at constant $\text{Ca}^{2+}/\text{CO}_3^{2-}$ ratio, the (+) steps moved progressively faster than the (-) steps causing v_+/v_- to increase. However, this effect was relatively moderate in scale, with v_+/v_- varying from 1.3 to 1.6 for one series and from 1.0 to 1.2 for the other. The general trend of more isotropic step velocities at lower saturation states agreed with the Teng et al. (1999) study, however the magnitude of the effect of saturation state on step velocity anisotropy and hillock geometry was very different, with the current study finding a much weaker dependence of hillock geometry and calcite growth anisotropy on the saturation state.

1.3.2 Ratio Experiments: The Role of $\text{Ca}^{2+}/\text{CO}_3^{2-}$ Concentration Ratio in Calcite Growth

The effect of $\text{Ca}^{2+}/\text{CO}_3^{2-}$ concentration ratio on calcite growth was investigated using AFM observations of calcite crystallization from solutions with strong variation in $\text{Ca}^{2+}/\text{CO}_3^{2-}$ concentration ratio and constant saturation state. The step-specific measurements of step-velocity and terrace width were found to be extremely sensitive to changes in $\text{Ca}^{2+}/\text{CO}_3^{2-}$ concentration ratio, which in turn produced significant changes in hillock geometry (Fig. 1.9). The fastest step velocities and the fastest rate of spiral rotation were measured at a $\text{Ca}^{2+}/\text{CO}_3^{2-}$ concentration ratio of 1. At this $\text{Ca}^{2+}/\text{CO}_3^{2-}$ concentration ratio, the positive (+) steps moved a little faster than the negative (-) steps, resulting in a slightly anisotropic growth spiral ($v_+/v_- = 1.3$). However, as the $\text{Ca}^{2+}/\text{CO}_3^{2-}$ concentration ratio fell below one, the growth spirals quickly became isotropic,

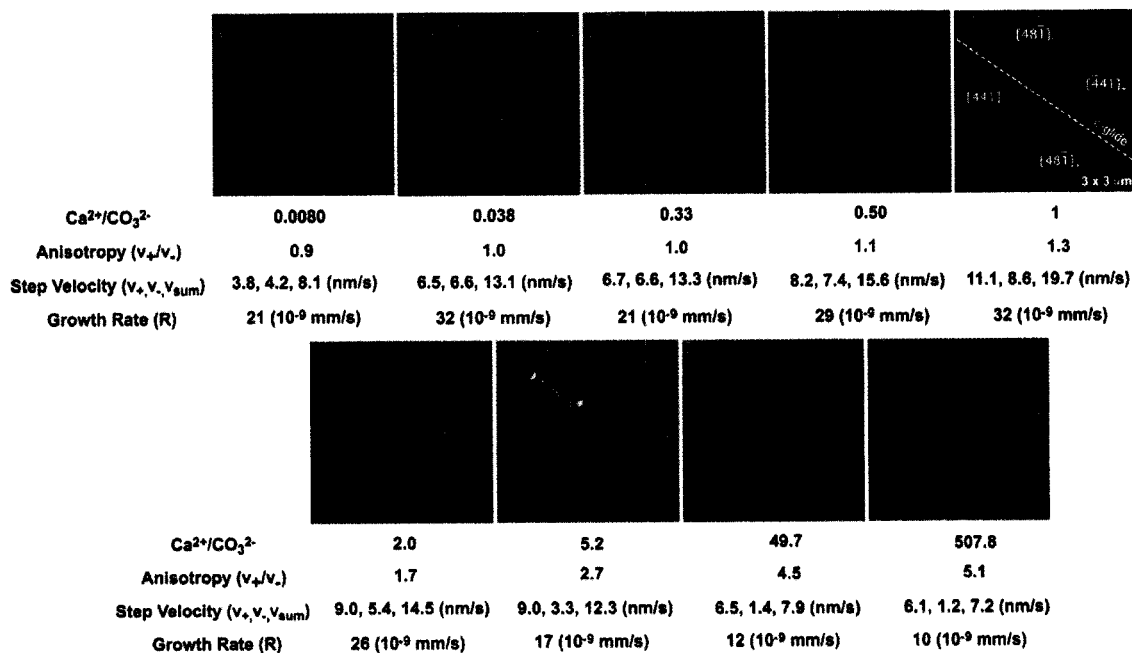


Figure 1.9 – Calcite Growth Hillocks Grown Under Different $\text{Ca}^{2+}/\text{CO}_3^{2-}$ Concentration Ratios at Constant Saturation State ($\sigma = 2.34$, $\Omega = 10.4$).

Changes in $\text{Ca}^{2+}/\text{CO}_3^{2-}$ ratio show that calcite growth anisotropy is strongly dependent on solution stoichiometry.

exhibiting near equivalent step velocities for the two step-types. In contrast, increasing $\text{Ca}^{2+}/\text{CO}_3^{2-}$ concentration ratios produced progressively anisotropic growth hillocks. This effect resulted from increasingly faster relative positive (+) step velocities as compared to the negative (-) step speeds, even though the velocities of both step-types fell as the $\text{Ca}^{2+}/\text{CO}_3^{2-}$ concentration ratio increased away from unity (Fig. 1.10). For instance, at a $\text{Ca}^{2+}/\text{CO}_3^{2-}$ concentration ratio of 2, the + steps moved nearly twice as fast as the – steps, and at a $\text{Ca}^{2+}/\text{CO}_3^{2-}$ concentration ratio of 5.2, the + steps moved nearly three times as fast as the – steps. As the $\text{Ca}^{2+}/\text{CO}_3^{2-}$ concentration ratio approached 50, the + steps moved nearly five times as fast as the negative step-types. This large difference in step velocities produced extreme differences in the terrace widths exhibited by the two step-types as well as in the geometry of the hillock (Fig. 1.9). It is important to note that over this interval of increasing $\text{Ca}^{2+}/\text{CO}_3^{2-}$ concentration ratio, the velocity of both step-types decreased such that v_{sum} fell from 19.7 nm/s to 7.9 nm/s. The observed change in step-velocity anisotropy reflected a greater individual sensitivity to decreasing $\text{Ca}^{2+}/\text{CO}_3^{2-}$ concentration ratio for the negative step-type than for the positive step-type. Furthermore, it is clear from this data that the anisotropy of calcite growth is principally determined by the $\text{Ca}^{2+}/\text{CO}_3^{2-}$ concentration ratio (Fig. 1.11).

Independent of whether the $\text{Ca}^{2+}/\text{CO}_3^{2-}$ concentration ratio of the experimental solutions was greater or less than one, measured step velocities were found to decrease as the $\text{Ca}^{2+}/\text{CO}_3^{2-}$ concentration ratio deviated from unity (Fig. 1.10). In fact, the sum of the step velocities for the two step-types (v_{sum}) decreased in a nearly symmetrical fashion as the $\text{Ca}^{2+}/\text{CO}_3^{2-}$ concentration ratio moved away from one. However this effect was accomplished in a very different way at higher $\text{Ca}^{2+}/\text{CO}_3^{2-}$ concentration ratios than at

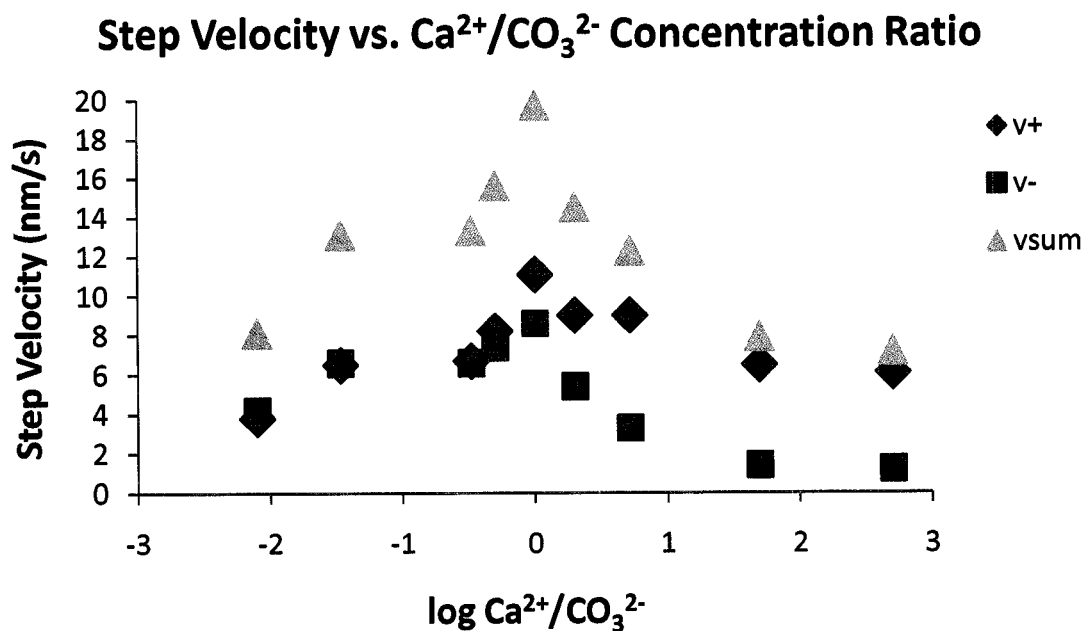


Figure 1.10 – Step Velocity Versus $\text{Ca}^{2+}/\text{CO}_3^{2-}$ Concentration Ratio at Constant Saturation

As the $\text{Ca}^{2+}/\text{CO}_3^{2-}$ ratio deviates from unity, measured step velocities tend to decrease. While the v_{sum} is nearly symmetrical on either side of Ratio=1, it is accomplished in different ways. At $R < 1$ both step-types travel with equivalent velocities (isotropic). However, for $R \gg 1$, step velocities are anisotropic with the + step accounting for several times more growth than the slower – steps.

Step Velocity Anisotropy vs. $\text{Ca}^{2+}/\text{CO}_3^{2-}$ Ratio (Saturation Controls Shown for Comparison)

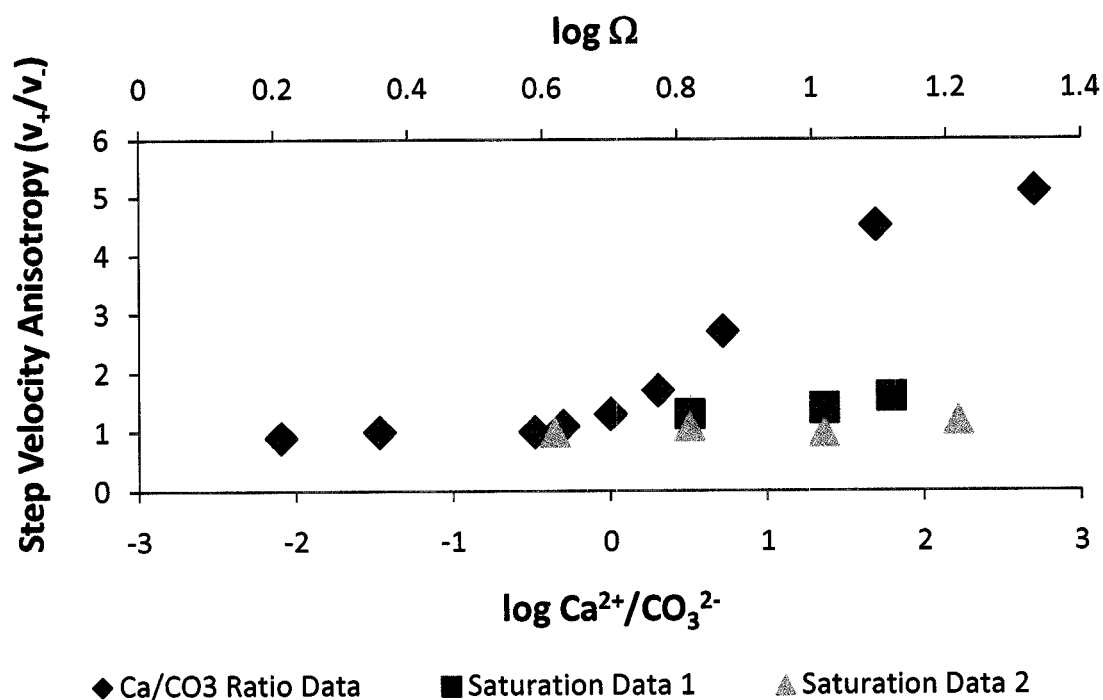


Figure 1.11 – $\text{Ca}^{2+}/\text{CO}_3^{2-}$ Concentration Ratio Controls Step-Edge Anisotropy

The anisotropy of calcite step velocities (v_+/v_-) is strongly dependent on the $\text{Ca}^{2+}/\text{CO}_3^{2-}$ concentration ratio.

lower $\text{Ca}^{2+}/\text{CO}_3^{2-}$ concentration ratios. At $\text{Ca}^{2+}/\text{CO}_3^{2-}$ concentration ratios less than 1, both step-types travelled with equivalent velocities. However, for $\text{Ca}^{2+}/\text{CO}_3^{2-}$ concentration ratios greater than 1, step velocities were anisotropic, with the (+) step accounting for several times more growth than the slower (-) steps (Fig. 1.10). Unlike for v_{sum} , the calculated BCF spiral growth rate was not found to be symmetrical on either side of $R=1$ (Fig. 1.12). A slower spiral growth rate was calculated for higher $\text{Ca}^{2+}/\text{CO}_3^{2-}$ concentration ratios. Inspection of the data in Table 1.3 demonstrates that a slower rate was calculated at elevated $\text{Ca}^{2+}/\text{CO}_3^{2-}$ concentration ratios because of a disproportionately slower period of spiral rotation (slower step generation rate), rather than a difference in the sum of the step velocities (Fig. 1.13). This resulted in a smaller slope component of the BCF equation for spiral growth and smaller calculated growth rates.

Insight into the cause of this disproportionately slower rate of spiral rotation at higher $\text{Ca}^{2+}/\text{CO}_3^{2-}$ concentration ratios can be achieved by plotting the period of spiral rotation versus step velocity anisotropy (v_+/v_-) (Fig. 1.14). While there is a small increase in the period of rotation measured at slower isotropic step velocities, a much larger decrease in period occurred as a result of anisotropic step migration. Furthermore, the linear relationship between step velocity anisotropy and the period of rotation (Fig. 1.14) seemed to outweigh the contribution of v_{sum} to the BCF growth rate. Accordingly, at the monomolecular step-scale, dislocation-controlled changes in step generation rates were found to play a more significant role in determining calcite growth rates than the dynamics of steps far away from the center of spiral rotation. However, the relevance of

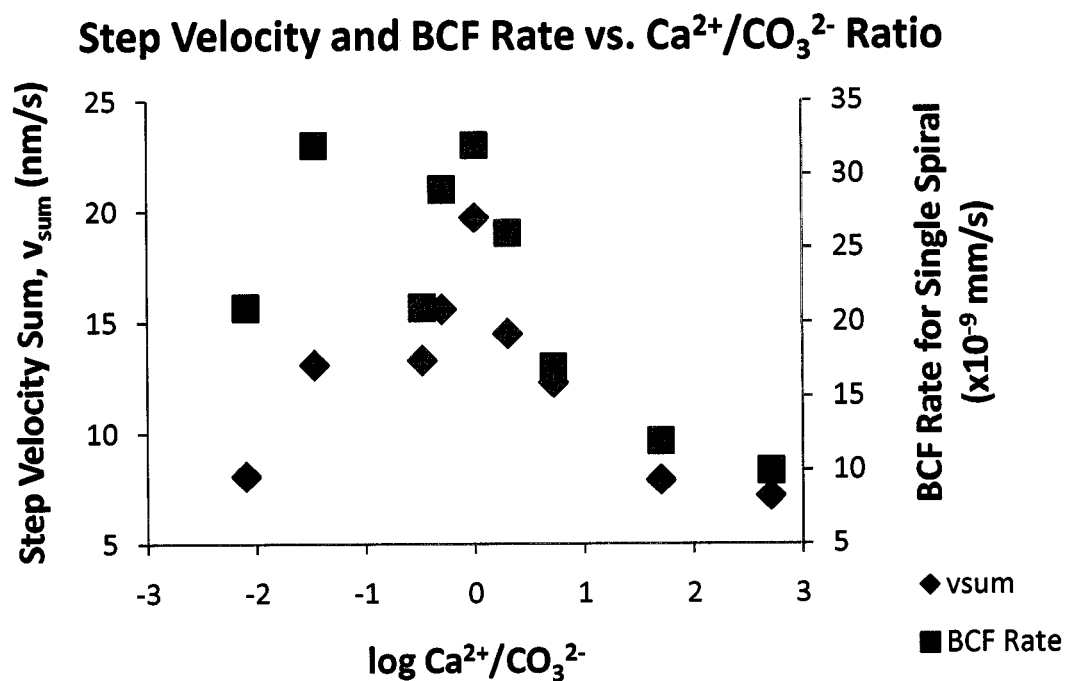


Figure 1.12 – v_{sum} Versus BCF Rate ($R=pv$)

Unlike v_{sum} , the calculated BCF spiral growth rate is not symmetrical on either side of $R=1$. A slower spiral growth rate is observed for $R>1$ due to a disproportionately slower period of spiral rotation.

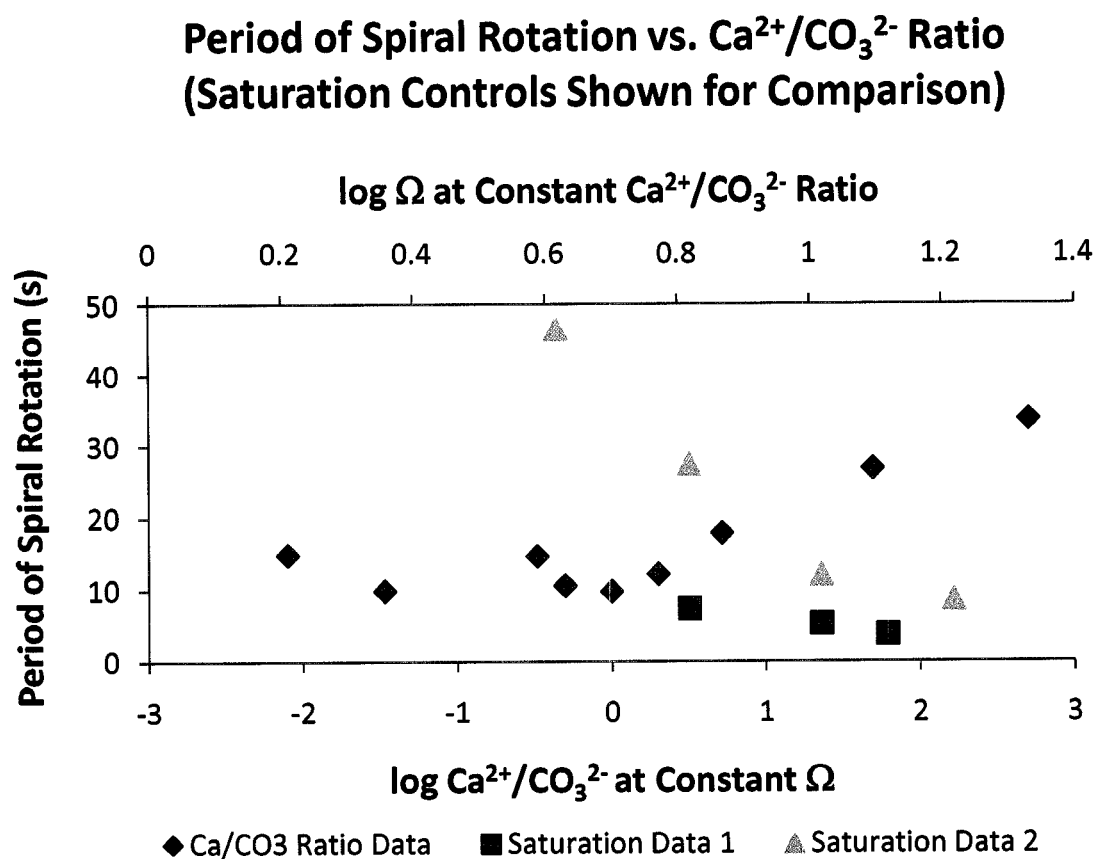


Figure 1.13 – Period of Spiral Rotation Versus Saturation State and $\text{Ca}^{2+}/\text{CO}_3^{2-}$ Concentration Ratio

Increasing $\text{Ca}^{2+}/\text{CO}_3^{2-}$ concentration ratio increases the period of spiral rotation (slows the step generation rate), in a manner similar to that expected from a significant decrease in the saturation state.

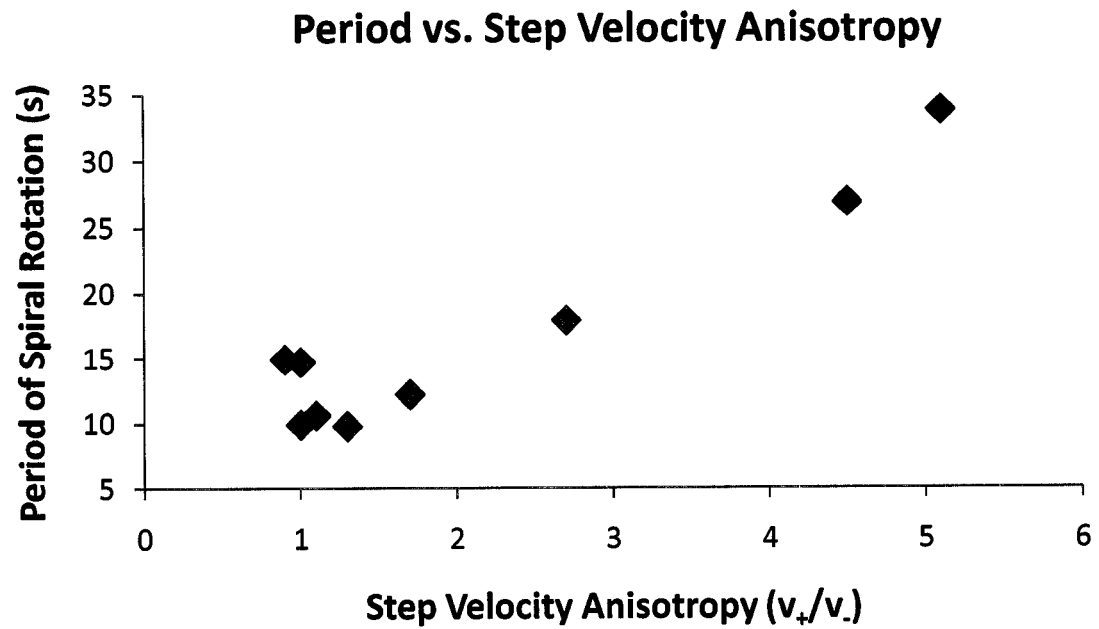


Figure 1.14 – Period of Spiral Rotation Versus Step Velocity Anisotropy

Since spiral periodicity correlates in part with anisotropy, the slower spiral turn rate may be a consequence of strain near the dislocation source.

this important experimental result to large-scale calcite growth required confirmation over greater length-scales using vertical scanning interferometry (VSI) measurements.

1.3.3 Vertical Scanning Interferometry (VSI): Surface Normal Calcite Growth Rates Under Different of $\text{Ca}^{2+}/\text{CO}_3^{2-}$ Concentration Ratios

A rigorous understanding of the mechanisms of crystal growth can only be achieved by linking fundamental measurements of monomolecular step movement with macroscopic observations of growing crystal surfaces. The resultant observational gap between step dynamics and overall reaction rates can be bridged using vertical scanning interferometry (VSI). VSI provides the ability to quantitatively map large areas of a surface while resolving the relative importance of particular growth features. The high vertical resolution and large field of view characteristic of VSI made this technique especially well-suited for imaging calcite growth hillocks while measuring surface normal growth rates relative to masked reference surfaces. After 13 hours in the same experimental solutions used for AFM measurements, VSI imaging demonstrated that calcite growth surfaces were characterized by an array of growth hillocks with different dislocation sources (e.g., Figs. 1.6 and 1.15). Measurements of surface normal growth rates made over this interval (Table 1.4) could be compared to those BCF rates calculated from AFM measurements of step velocity and terrace width (slope) (Table 1.3). As expected, measured VSI rates were greater than those determined for the single-source growth hillocks observed in the AFM experiments (Fig. 1.16). The presence of multiple-source growth hillocks with higher step generation rates provided for faster surface normal growth rates when averaged over large areas of the calcite growth surface. However, the

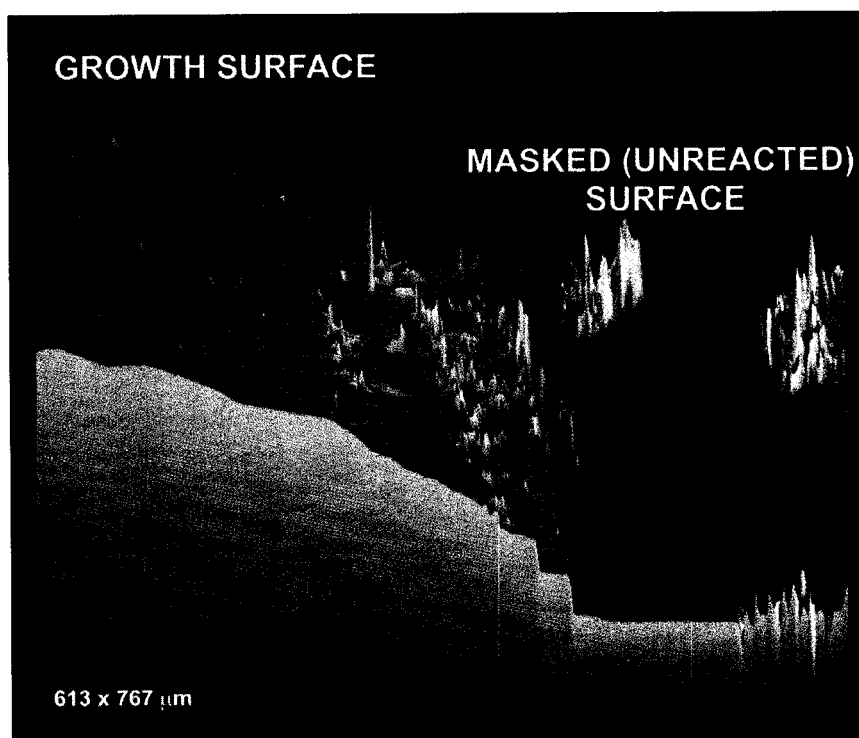


Figure 1.15 – VSI Measurements of Surface Normal Growth

VSI bridges the observational gap between step dynamics and overall reaction rates by measuring the rates of calcite surface growth produced by numerous growth hillocks. Rates are determined by measuring the average height difference between the growth surface and an unreacted (masked surface). This image depicts growth that occurred during a 13.5 hour experiment.

Table 1.4 – VSI Data for the Saturation Controls and Ratio Experiments

Solution ID	σ	$\text{Ca}^{2+}/\text{CO}_3^{2-}$ Ratio	Surface Advance (nm)	Experimental Duration (s)	Rate ($\text{mol cm}^{-2} \text{s}^{-1}$)	Rate ($\times 10^{-9} \text{ mm/s}$)
control 1-1	1.88	1.0	1729	49,440	9.47×10^{-11}	34.97
control 1-2	2.34	1.0	2650	47,624	1.51×10^{-10}	55.64
control 2-4	2.80	1.0	4196	48,733	2.33×10^{-10}	86.10
ratio 1-1	2.34	0.0080	1737	49,921	9.42×10^{-11}	34.79
ratio 1-2	2.34	0.038	1522	49,200	8.38×10^{-11}	30.93
ratio 1-3	2.34	0.33	2231	49,592	1.22×10^{-10}	44.99
ratio 1-5	2.34	1.0	2650	47,624	1.51×10^{-10}	55.64
ratio 1-7	2.34	5.2	2175	49,934	1.18×10^{-10}	43.56
ratio 1-8	2.34	49.7	712	49,401	3.90×10^{-11}	14.41
ratio 1-9	2.34	507.8	588	45,600	3.49×10^{-11}	12.89

Solutions “control 1-2” and “ratio 1-5” are the same experiment.

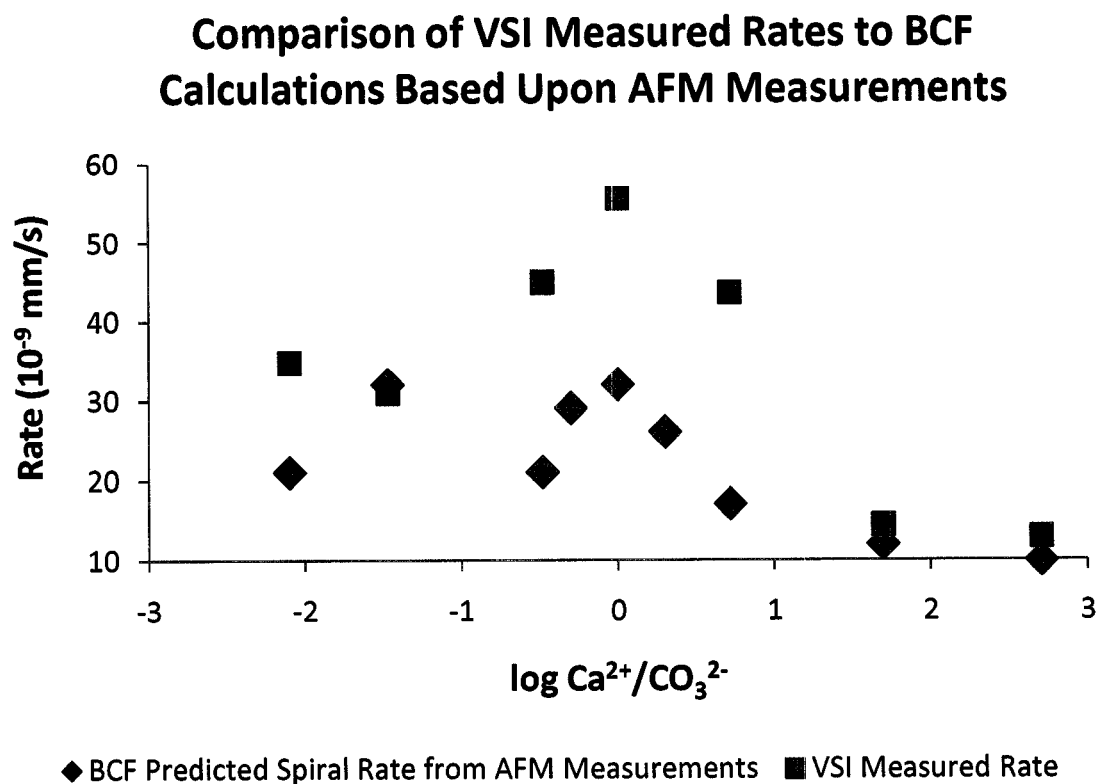


Figure 1.16 – VSI Measurements of Surface Normal Growth

VSI measurements confirm that the general relationship between ratio and the growth rate determined by AFM, including the reduced rates for $R \gg 1$ due to reduced step generation rates.

VSI surface normal growth data supported the AFM observation that the highest calcite growth rates occur in growth solutions with a $\text{Ca}^{2+}/\text{CO}_3^{2-}$ concentration ratio equal to one. As the $\text{Ca}^{2+}/\text{CO}_3^{2-}$ concentration ratio of experimental solutions departed from one, the measured surface normal growth rate decreased. For instance, at $\text{Ca}^{2+}/\text{CO}_3^{2-}$ concentration ratios of either 0.33 or 5.2, the surface normal growth rates decreased by approximately 20%. However, the decline in surface normal growth rates was not completely symmetric about unity. Instead, measured growth rates at higher $\text{Ca}^{2+}/\text{CO}_3^{2-}$ concentration ratios were significantly slower than those measured for the equivalent lower $\text{Ca}^{2+}/\text{CO}_3^{2-}$ concentration ratios. Accordingly, VSI measurements confirm the prediction from AFM observations that reduced step generation rates result in reduced surface normal growth rates from solutions with elevated $\text{Ca}^{2+}/\text{CO}_3^{2-}$ concentration ratios (Fig. 1.16).

1.4 Conclusions

1.4.1 Solution Stoichiometry and Calcite Growth Rate: Implications for the Applicability of Affinity-Based Rate Laws

The results of this study demonstrate that solution stoichiometry plays a fundamental role in determining both the rate and anisotropy of calcite growth. For the first time, the interaction between monomolecular surface steps and the cation/anion ratio in carbonate solutions has been resolved with intriguing results. Changes in the $\text{Ca}^{2+}/\text{CO}_3^{2-}$ concentration ratio were shown to produce changes in calcite growth rate to a degree normally only considered to be achievable through changes in the saturation state.

Further, our experiments demonstrated that the defect itself exerts a primary influence over growth rates in nonstoichiometric solutions. Changes in solution stoichiometry produced differences in step generation rates at growth spirals (period of spiral rotation) that were most pronounced in solutions that yielded highly anisotropic step velocities. These reduced step generation rates were shown to produce decreased surface normal growth rates as measured by longer-duration VSI experiments under the same solution conditions. The fact that the measured decrease in the rate of spiral rotation exhibited a linear dependence on increasing step anisotropy indicated that this phenomenon may be due to the development of strain near the center of the dislocation. This strain may be generated by the stacking of – steps near the dislocation source. Irrespective of the exact molecular-scale mechanism for rate reduction, the fact that highly anisotropic step speeds (as produced by changes in solution chemistry) affect step production at dislocations gives new insight into the dynamics of step generation as well as elucidating a new mechanism of rate modification that extends beyond the simple motion of elementary steps. This novel mechanism of rate modification is not predicted by BCF theory and may need to be included in any future comprehensive theory of crystal growth from nonstoichiometric solutions.

Additionally, the results of this study call into question a common stipulation in geochemistry that the dehydration of the cation may be the rate-limiting step in growth. Our experiments show no such advantage in growth rate under any of the elevated cation concentrations tested, either at the elementary step-scale measured by AFM or the surface-scale measured using VSI. Instead the kinetic limitations induced by nonstoichiometric solutions were found to be predominant in determining the growth rate

of calcite. In fact, high cation concentrations produced slower growth rates than those measured for high carbonate solutions due to the slower step production rate caused by the anisotropic step velocities that occurred in such solutions. The fact that no enhancement in growth rate was found under elevated $\text{Ca}^{2+}/\text{CO}_3^{2-}$ concentration ratios suggests that the long-held belief that the dehydration of the cation is a rate-limiting step for crystallization is erroneous for the calcium carbonate system.

However, our experiments did yield some insight into the kinetics of cation/anion incorporation at step-edges. In fact, our experiments involving changes in the $\text{Ca}^{2+}/\text{CO}_3^{2-}$ concentration ratio at constant saturation served as an effective probe for determining step-specific interactions with the Ca^{2+} and CO_3^{2-} species in solution. The fact that changes in $\text{Ca}^{2+}/\text{CO}_3^{2-}$ concentration ratios produces anisotropy in step velocities reflects fundamental differences in the roles of the cation and anion in determining calcite step dynamics. For instance, at high $\text{Ca}^{2+}/\text{CO}_3^{2-}$ concentration ratio, the – step types were much more kinetically affected than the + step-types. This may indicate that incorporation of CO_3^{2-} ion may be much more rate-limiting at these steps than for the + step-edges. At the other end-member in solution stoichiometry, the lowest $\text{Ca}^{2+}/\text{CO}_3^{2-}$ concentration ratios tested produced slightly anisotropic step velocities, favoring faster – step movement. This may indicate that the + steps are disproportionately affected by lower Ca^{2+} concentrations. This result may be reinforced by the coincident development of a new microfacet or vicinal face on the growth hillock due to a broadening of the +/+ corner. This interesting result may indicate that kink-sites in this location are especially sensitive to low Ca^{2+} concentrations causing the formation of a new slow step-direction. Since reaction mechanisms ultimately involve specific interactions between solution

species and advancing steps, $\text{Ca}^{2+}/\text{CO}_3^{2-}$ ratio experiments may represent the best way to investigate the molecular-scale interactions between step-edge structure and solution chemistry.

1.4.2 Solution Stoichiometry and Calcite Growth Anisotropy: Implications for Carbonate Biomineralization Strategies and Trace/Minor Element Proxies

The results of this study show that the $\text{Ca}^{2+}/\text{CO}_3^{2-}$ concentration ratio in solution is the principal driver of calcite growth anisotropy. While it had been earlier reported that saturation state determines the growth anisotropy of calcite, solution stoichiometry had not previously been considered as a potential factor and so was not investigated. The current investigation, using solutions exhibiting different $\text{Ca}^{2+}/\text{CO}_3^{2-}$ concentration ratios with precise solution chemistry and careful saturation state controls, now clearly demonstrates that $\text{Ca}^{2+}/\text{CO}_3^{2-}$ concentration ratio is a much more important factor in determining step velocity anisotropy and its dependent changes in hillock geometry than the saturation state.

The fact that simple changes in $\text{Ca}^{2+}/\text{CO}_3^{2-}$ concentration ratio significantly alters the anisotropy of calcite growth, suggests that biological control over solution stoichiometry may play a role in the morphological development of biominerals. Perhaps more importantly, this finding also holds important consequences for impurity incorporation in carbonate biominerals. The necessary result of anisotropic growth is that a larger proportion of the new crystal surface is deposited by the advancement of one step-type over another. Since it is well-documented that impurity incorporation in calcite is step-specific, anisotropic step speeds are likely to produce differences in the

partitioning of trace and minor elements in biominerals. Accordingly, this study demonstrates that changes in $\text{Ca}^{2+}/\text{CO}_3^{2-}$ concentration ratio may be a significant factor in impurity incorporation in calcite. For instance, since high $\text{Ca}^{2+}/\text{CO}_3^{2-}$ concentration ratios in solution cause the + steps to move much faster than the – steps, more of the new deposited layers of calcium carbonate are formed by advancing + steps. Since Mg^{2+} has been shown to preferentially incorporate into the – step-type, the resultant crystal would be expected to be relatively depleted in Mg^{2+} under high $\text{Ca}^{2+}/\text{CO}_3^{2-}$ concentration ratios. On the other hand, Sr^{2+} preferentially incorporates into the + steps and would likely be enriched in the solid phase grown under the same solution conditions. It follows that manipulation of $\text{Ca}^{2+}/\text{CO}_3^{2-}$ concentration ratio may be an important mechanism by which different organisms induce different concentrations of minor and trace elements in the same calcium carbonate product. Further investigation is required to determine if $\text{Ca}^{2+}/\text{CO}_3^{2-}$ concentration ratios play a significant role in determining the vital effect. In considering the importance of this study to biomineral systems it must be determined what relevance the calcite cleavage surface has to the vast array of biomineral surfaces found in nature. We know of at least one important biomineral surface in which the results of this study are likely to be directly relevant. The *Emiliani huxleyi* coccolithophore has been shown to exhibit the same {104} surfaces used in this study (Henriksen et al., 2003). However, any system that exhibits anisotropy of layer deposition due to differences in step-edge structure may be expected to be sensitive to the stoichiometry of the solution. Further, since biological control over this quantity is extremely likely during either passive or active biomineralization processes, the

possibilities for consequential biological crystallization mechanisms involving differences in $\text{Ca}^{2+}/\text{CO}_3^{2-}$ concentration ratio are numerous.

1.4.3 The Importance of the Surface in Determining Growth Rates

The results of this study suggest that as the $\text{Ca}^{2+}/\text{CO}_3^{2-}$ concentration ratio deviates from one, calcite growth becomes kinetically-limited and saturation or concentration-based rate laws become less applicable. Further inadequacy of current rate laws for describing calcite growth is indicated by the observation that high $\text{Ca}^{2+}/\text{CO}_3^{2-}$ concentration ratios produce disproportionately slow calcite growth rates due to reduced step generation rates at the dislocation source. This experimental result, confirmed at multiple length-scales, could not have been predicted by consideration of bulk chemistry alone but instead required special consideration of the surface and its interaction with specific chemical species in solution. This study provides an extension of the BCF concept that defects enhance growth rates to include the effect of step velocity anisotropy. Surface defects do not simply enhance growth rates by providing a continuous source of steps, but are a means by which rates are modified by specific interactions with chemical species in solution. We are still learning how key chemical species in solution interact with specific surface sites and defects to produce the complicated array of observed crystallization processes. Nonetheless, this study clearly demonstrates that surfaces play a key role in rate determination that cannot be separated from pure considerations of bulk chemistry. Even in the absence of specific knowledge of the surface, the results of this study suggest that current rate laws should be modified to consider the role of solution stoichiometry in determining calcite growth rates.

CHAPTER 2. Calcite Dissolution in Nonstoichiometric Solutions: A Site-Specific Role for Carbonate Control of Dissolution Rates

Abstract

A rigorous understanding of calcite dissolution rates is necessary for determining the relationship between past changes in the carbonate compensation depth (CCD) and seawater carbonate chemistry that may be used for paleo- $p\text{CO}_2$ reconstruction. Current rate laws assume that calcite dissolution kinetics is governed by the saturation state, ignoring the potential influence of solution stoichiometry ($\text{Ca}^{2+}/\text{CO}_3^{2-}$ ratio) on dissolution rates. Here we determine the effect of solution stoichiometry, at constant saturation state, on calcite dissolution rates under near-equilibrium conditions. Our results demonstrate that the $\text{Ca}^{2+}/\text{CO}_3^{2-}$ solution ratio plays a significant role in calcite dissolution that is comparable to that of saturation state. Further, we show that the influence of solution stoichiometry on calcite dissolution can be reduced to site-specific control by the carbonate ion on particular surface steps. A downstream effect of the role of carbonate ion in determining step dynamics is a significant reduction in step generation rates at dislocation sources in the presence of excess carbonate ions. Accordingly, dissolution rates at constant saturation state are slower in solutions with relatively high $[\text{CO}_3^{2-}]$ (low $\text{Ca}^{2+}/\text{CO}_3^{2-}$ ratio) and are faster in solutions with relatively low $[\text{CO}_3^{2-}]$ (high $\text{Ca}^{2+}/\text{CO}_3^{2-}$ ratio). Further, our data demonstrates additional kinetic limitations on calcite dissolution rates in nonstoichiometric solutions resulting from elevated attachment rates relative to detachment rates in the presence of excess cations or anions. These results indicate that rate laws describing calcite dissolution kinetics should be modified to incorporate the relative concentration of carbonate ion at a given degree of undersaturation as well as other kinetic limitations imposed by nonstoichiometric

solutions. Further, the role of solution stoichiometry on calcite dissolution rates should be included in the assessment of the future impacts of ocean acidification.

2.1 Introduction

Carbonate minerals are principal components of biomineralizing systems and play a central role in a number of important biogeochemical cycles. The relative rates of carbonate mineral precipitation and dissolution determine the preservation and subsequent accumulation of carbonate in the geologic record as well as the sequestration of several coprecipitated trace elements (Morse, 1983; Morse & Mackenzie, 1990; Morse & Arvidson, 2002). In particular, the calcite dissolution rate is critical for determining the location of both the lysocline, which is the depth in the oceans where the rate of carbonate dissolution rapidly increases, and the carbonate compensation depth (CCD), below which carbonate sediments are lacking. Accordingly, the accurate determination of deep-sea calcite dissolution rates are crucial for understanding the role of the marine carbonate system in regulating $p\text{CO}_2$ over the geologic past. Interestingly, a recent study has attempted to reconstruct ocean $[\text{CO}_3^{2-}]$ concentrations and atmospheric CO_2 over the last 100 million years from changes in the CCD and seawater $[\text{Ca}^{2+}]$ concentrations (Tyrrell & Zeebe, 2004). The authors calculated seawater $[\text{CO}_3^{2-}]$ from the calcite saturation state, which is proportional to the product of $[\text{Ca}^{2+}]$ and $[\text{CO}_3^{2-}]$. However, the CCD is rigorously determined by the relative kinetics of calcite precipitation and dissolution rather than the saturation state. The changes in saturation state that have occurred during the geologic past are caused by independent variations in seawater $[\text{Ca}^{2+}]$ and $[\text{CO}_3^{2-}]$ which also produce considerable changes in the

stoichiometric ratio ($[\text{Ca}^{2+}]/[\text{CO}_3^{2-}]$) of seawater (Stanley & Hardie, 1998; Lowenstein et al., 2001; Tyrrell & Zeebe, 2004). While current rate laws express dissolution in terms of the degree of undersaturation, it is likely that significant deviations in solution stoichiometry may impose further kinetic limitations on the dissolution rate.

Accordingly, a precise understanding of calcite dissolution rates under near-equilibrium conditions must include the kinetic role of solution stoichiometry. Here we present measurements of calcite dissolution rates under different $\text{Ca}^{2+}/\text{CO}_3^{2-}$ solution ratios at constant undersaturation in order to determine the precise role of solution stoichiometry in determining calcite dissolution kinetics. In a departure from many previous investigations of calcite dissolution, these measurements were conducted under near-equilibrium conditions by measuring monomolecular step dynamics at dislocation spirals (etch pits) that are thought to be representative of most natural systems. This was achieved through the use of atomic force microscopy (AFM) which allowed for the measurement of fundamental crystal dissolution parameters over the short empirical timescales required to maintain precise control over solution chemistry, that in turn allowed for the decoupling of the roles of solution stoichiometry and saturation state. Our results demonstrate that changes in the $\text{Ca}^{2+}/\text{CO}_3^{2-}$ ratio of carbonate solutions, at constant saturation, play a significant role in the determination of calcite dissolution rates. Further, step-specific measurements made under varying ionic ratios reveal the underlying mechanisms responsible for the role of solution stoichiometry in determining calcite dissolution rates. The novel insight gained in this study suggests that the application of current rate laws to solutions of varying ionic ratios may be limited.

2.2 Materials and Methods

2.2.1 Solution Chemistry Modeling

Experimental investigation of the role of solution stoichiometry in calcite dissolution requires experimental solutions with precisely controlled saturation states and calcium carbonate chemistries. This was achieved using the EQ3NR chemical speciation code (Wolery, 1992) and specially-designed solution preparation schemes. The recipe for each experimental solution was calculated using the numerical code which implemented the B-dot equation for activity determinations. Solutions of the appropriate undersaturation were generated by manually adjusting the solubility product (K_{sp}) of calcite used to determine the activities of calcium and carbonate in solution. The remaining model input parameters included total sodium (Na_T) and total chloride (Cl_T). Additionally, the pH of the system was fixed at 8.5 (control series; ratio series 2) or 8.9 (ratio series 1).

Solutions with different Ca^{2+}/CO_3^{2-} concentration ratios at constant saturation state (IAP) were created by changing the relative concentrations of Na_T and Cl_T , thereby forcing the system to electrochemically balance on the Ca^{2+} and CO_3^{2-} ions while maintaining the constant IAP set by the K_{sp} . In this way, solutions with exact Ca^{2+}/CO_3^{2-} activity ratios were calculated by adjusting Na_T and Cl_T in the numerical code. The activity (concentration) of Ca^{2+} was solved in the model by setting it equal to the ratio of the desired IAP and carbonate ion activity:

$$a_{Ca^{2+}} = \frac{IAP}{a_{CO_3^{2-}}} = R \ a_{CO_3^{2-}}$$

where R is the desired ratio. Thus, $a_{CO_3^{2-}} = \sqrt{IAP/R}$. By fixing pH and carbonate ion activity, the two necessary and sufficient constraints on the carbonic acid are met. In practice, the desired ratio (R) was controlled by adding mineral alkalinity in the form of bicarbonate or introducing negative alkalinity through the addition of mineral acid, HCl (see solution preparation below). The solution compositions that satisfied these conditions were computed using EQ3NR and the critical speciation outputs were the activities of Ca^{2+} and CO_3^{2-} , total Ca (Ca_T), ionic strength (I), and the concentration of bicarbonate ion ($m_{HCO_3^-}$). The degree of undersaturation (Ω) was calculated from the ion activity product (IAP) and the solubility product (K_{sp}) according to:

$$\Omega = \frac{IAP}{K_{sp}} = \frac{a_{Ca^{2+}}a_{CO_3^{2-}}}{K_{sp}}$$

using a K_{sp} equal to $10^{-8.48}$, which was calculated from the activities at which measured step velocities went to zero. While we use Ca^{2+} and CO_3^{2-} activities to compute the saturation state (IAP), we thereafter report the Ca^{2+}/CO_3^{2-} ratio as a concentration ratio, since it is the concentration of these species that controls the kinetics of calcite dissolution. However, it should be noted that the activity coefficients for Ca^{2+} and CO_3^{2-} in this study are nearly identical for all of the experimental solutions employed in this study, and so the reported Ca^{2+}/CO_3^{2-} concentration ratios are numerically equivalent to the Ca^{2+}/CO_3^{2-} activity ratios for the reported number of digits.

2.2.2 Solution Preparation

Undersaturated growth solutions with precisely controlled $\text{Ca}^{2+}/\text{CO}_3^{2-}$ activity ratios were prepared using the results from the chemical speciation calculations, including: Na_T , Cl_T , and Ca_T and pH (Table 2.1). In order for the solutions to be electrochemically balanced as modeled, Na_T and Cl_T had to be independently delivered as acid-base pairs instead of as electroneutral salts. Accordingly, Na and Cl were introduced gravimetrically as NaOH (0.9454 mol/kg soln) and HCl (8.9492×10^{-2} mol/kg soln), respectively. Ca_T was delivered in two different ways for the two experimental series (ratio series 1 and ratio series 2). For the first series (ratio 1-1 through ratio 1-6), Ca_T was delivered gravimetrically from a CaCO_3 solution that had been dissolved under a CO_2 atmosphere. For these solutions, the CaCO_3 solution was also a source of initial carbonate. For the second ratio series (ratio 2-1 through ratio 2-7) as well as the control series, Ca_T was delivered gravimetrically as CaCl_2 (0.4658 mol/kg soln). Additionally, each of the second set of experimental solutions had an initial HCO_3^- concentration of 0.001 mol/kg soln, introduced using a NaHCO_3 solution (0.09917 mol/kg soln). The pH of each solution was adjusted to 8.5 (control series; ratio series 2) or 8.9 (ratio series 1) by sparging with ultrapure CO_2 or N_2 gas as required. This final step produced solutions with precise $\text{Ca}^{2+}/\text{CO}_3^{2-}$ activity ratios that were stable over the experimental durations employed.

Table 2.1 – Solution Speciation for the Saturation Controls and Ratio Experiments with Preparation Parameters

Used to Prepare Solutions												
Solution ID	Calculated by Model (Model Output)					Model Input				Model Output		
	Ω	σ	$a_{\text{Ca}^{2+}}$	$a_{\text{CO}_3^{2-}}$	$\text{Ca}^{2+}/\text{CO}_3^{2-}$ Ratio	I	-K _{sp}	pH	Na _T (mol/kg soln)	Cl _T (mol/kg soln)	Ca _T (mol/kg soln)	m _{HCO₃⁻} (mol/kg soln)
control 1-1	0.26	-1.35	2.9424x10 ⁻⁵	2.9410x10 ⁻⁵	1.00	0.003	-0.6	8.50	0.00326	0.001	4.0174x10 ⁻⁵	2.2x10 ⁻³
control 1-2	0.104	-2.26	1.8557x10 ⁻⁵	1.8565x10 ⁻⁵	1.00	0.003	-1.0	8.50	0.0024149	0.001	2.4001x10 ⁻⁵	1.4x10 ⁻³
control 1-3	0.041	-3.19	1.1752x10 ⁻⁵	1.1673x10 ⁻⁵	1.00	0.003	-1.4	8.50	0.0024	0.00151	1.4941x10 ⁻⁵	8.8x10 ⁻⁴
control 1-4	0.010	-4.57	5.8681x10 ⁻⁶	5.8708x10 ⁻⁶	1.00	0.002	-2.0	8.50	0.0014435	0.001	7.0430x10 ⁻⁶	4.4x10 ⁻⁴
ratio 1-1	0.104	-2.26	1.0167x10 ⁻⁶	3.3892x10 ⁻⁴	0.003	0.013	-1.0	8.90	0.0131	0.001	2.4078x10 ⁻⁶	1.1x10 ⁻²
ratio 1-2	0.104	-2.26	3.2151x10 ⁻⁶	1.0718x10 ⁻⁴	0.03	0.005	-1.0	8.90	0.004599	0.001	5.0927x10 ⁻⁶	3.3x10 ⁻³
ratio 1-3	0.104	-2.26	1.0170x10 ⁻⁵	3.3884x10 ⁻⁵	0.30	0.002	-1.0	8.90	0.002087	0.001	1.3244x10 ⁻⁵	1.0x10 ⁻⁴
ratio 1-4	0.104	-2.26	1.8561x10 ⁻⁵	1.8561x10 ⁻⁵	1.0	0.002	-1.0	8.90	0.0015629	0.001	2.2979x10 ⁻⁵	5.5x10 ⁻⁴
ratio 1-5	0.104	-2.26	3.2151x10 ⁻⁵	1.0718x10 ⁻⁵	3.0	0.001	-1.0	8.90	0.001276	0.001	3.8716x10 ⁻⁵	3.2x10 ⁻⁴
ratio 1-6	0.104	-2.26	1.0205x10 ⁻⁴	3.3760x10 ⁻⁶	30.3	0.001	-1.0	8.90	0.002	0.001125	1.2090x10 ⁻⁴	1.0x10 ⁻⁴
ratio 2-1	0.104	-2.26	8.3927x10 ⁻⁷	4.1058x10 ⁻⁴	0.002	0.038	-1.0	8.50	0.039	0.001	2.6800x10 ⁻⁶	3.5x10 ⁻²
ratio 2-2	0.104	-2.26	2.6382x10 ⁻⁶	1.3062x10 ⁻⁴	0.02	0.012	-1.0	8.50	0.012	0.001	5.0565x10 ⁻⁶	1.0x10 ⁻²
ratio 2-3	0.104	-2.26	8.3119x10 ⁻⁶	4.1448x10 ⁻⁵	0.20	0.004	-1.0	8.50	0.0043	0.001	1.1956x10 ⁻⁵	3.2x10 ⁻³
ratio 2-4	0.104	-2.26	1.8557x10 ⁻⁵	1.8565x10 ⁻⁵	1.0	0.003	-1.0	8.50	0.0024149	0.001	2.4001x10 ⁻⁵	1.4x10 ⁻³
ratio 2-5	0.104	-2.26	4.1400x10 ⁻⁵	8.3215x10 ⁻⁶	5.0	0.002	-1.0	8.50	0.00155	0.001	5.0577x10 ⁻⁵	6.3x10 ⁻⁴
ratio 2-6	0.104	-2.26	1.2996x10 ⁻⁴	2.6509x10 ⁻⁶	49	0.002	-1.0	8.50	0.001	0.0011	1.5475x10 ⁻⁴	2.0x10 ⁻⁴
ratio 2-7	0.104	-2.26	4.1352x10 ⁻⁴	8.3330x10 ⁻⁷	496	0.003	-1.0	8.50	0.001	0.00196	5.1486x10 ⁻⁴	6.3x10 ⁻⁵

Note: Ca_T was delivered as CaCO₃ for the ratio 1-1 through ratio 1-6 solutions. For all other solutions, Ca_T was delivered as CaCl₂

2.2.3 Atomic Force Microscopy (AFM) Experiments

Fluid-cell atomic force microscopy (AFM) was used to make *in situ* observations of CaCO_3 dissolution on the $(10\bar{1}4)$ calcite cleavage surface in a flow-through environment. Dissolution spirals emanating from screw dislocations on the calcite surface were imaged in Contact Mode (Digital Instruments, Santa Barbara) under controlled solution conditions at 25°C. The rate of solution input was adjusted to yield step velocities that were independent of flow rate, thereby ensuring that dissolution was not limited by mass transport to the surface. The resultant flow-rate of 30 mL/hr yielded a residence time of approximately 6 seconds in the 50 μL fluid-cell. Monomolecular step velocities (v_s) were directly measured on the dissolution spirals as the displacement of steps from a fixed reference point (e.g., the dislocation source) per unit time, using landmarks in the step train. The terrace width (λ), or the spacing between adjacent surface steps, was not easily discerned from the AFM images due to the extremely high step density produced by the dislocation. Instead, the terrace widths were calculated from the slope (ρ) of each vicinal face, which was measured as rise over run using the DI AFM software. The terrace width is related to the slope of the dissolution spiral according to:

$$\lambda = \frac{h}{\rho}$$

where h is the monomolecular step height (0.31 nm for calcite surface steps). However, the slope of the (+) vicinal faces was exceedingly steep under most solution conditions due to the bunching of (+) surface steps. This was found to be a source of considerable error as the AFM tip tracks steeper features less well than it tracks shallower features

over such small spatial scales. In order to mitigate this effect, the slope of the (+) vicinal faces was calculated from the terrace width of the (+) steps, which was in turn calculated using the step velocities of the two step-types and the terrace width of the (-) vicinal face which are rigorously related according to:

$$\frac{v_-}{\lambda_-} = \frac{v_+}{\lambda_+}$$

According to BCF theory (Burton et al., 1951), the dissolution rate (R) produced by a dissolution spiral is equal to the product of the step velocity (v_s) and the hillock slope (ρ):

$$R = v_s \rho$$

The rates calculated in this manner should be equivalent for the (+) vicinal faces and the (-) vicinal faces. However, since less error is associated with velocity and slope measurements along the (-) vicinal faces, only rates determined from these measurements were reported. The rate of step production can be quantified from this data set as the period of spiral rotation (τ) in seconds, which is defined as:

$$\tau = \frac{\lambda}{v_s}$$

In this way, the rate by which layer-by-layer dissolution occurs at a dissolution spiral can be thought of as being determined by the period of spiral rotation (the rate at which new steps are created) and the velocity of monomolecular surface steps (the rate at which steps move away from the dislocation source). Importantly, AFM provides for the measurement of these critical kinetic parameters as a function of step-edge structure, enabling an assessment of step-specific interactions between certain step-types and solutions exhibiting different stoichiometries (cation/anion ratios).

2.3 Results and Discussion

2.3.1 Dissolution at Dislocation Spirals

Layer-by-layer dissolution on the ($\bar{1}014$) calcite surface was observed as the migration of atomically flat steps generated a dislocation spirals. At this distance from $\Delta G = 0$, the creation of new dissolution steps was only observed at the bottom of dislocation-created etch pits, as there was apparently not enough thermodynamic driving force to begin new layers of dissolution in the absence of such defects. These solution conditions contrast sharply with previous AFM studies which commonly observed the nucleation of new steps at point defects on the calcite cleavage surface. To our knowledge, these experiments represent the first calcite dissolution experiments to be conducted under the near-equilibrium conditions common in many natural systems, where only steps created at screw dislocations are operative. The advancement of the 3.1 Å monomolecular steps created by the screw dislocation resulted in the formation of polygonal etch pits that reflected the symmetry of the crystal face and were similar in scale to the growth hillocks studied in previous experiments (Fig. 2.1). Each dissolution spiral exhibited four well-formed vicinal faces (Fig. 2.2). Each vicinal face was in turn comprised of relatively straight growth steps of like orientation that ran parallel to periodic bond chains (PBCs) in the calcite lattice (Reeder & Rakovan, 1999). The c -glide plane generates two distinct pairs of crystallographically identical steps, denoted as the positive ($[\bar{4}41]_+$ and $[48\bar{1}]_+$) and negative directions ($[\bar{4}41]_-$ and $[48\bar{1}]_-$) (Fig. 2.2). These two step-types have non-equivalent step-edge geometries and kink-site structures because of differences in the orientation of exposed carbonate groups (Reeder & Rakovan, 1999). The tilt of the

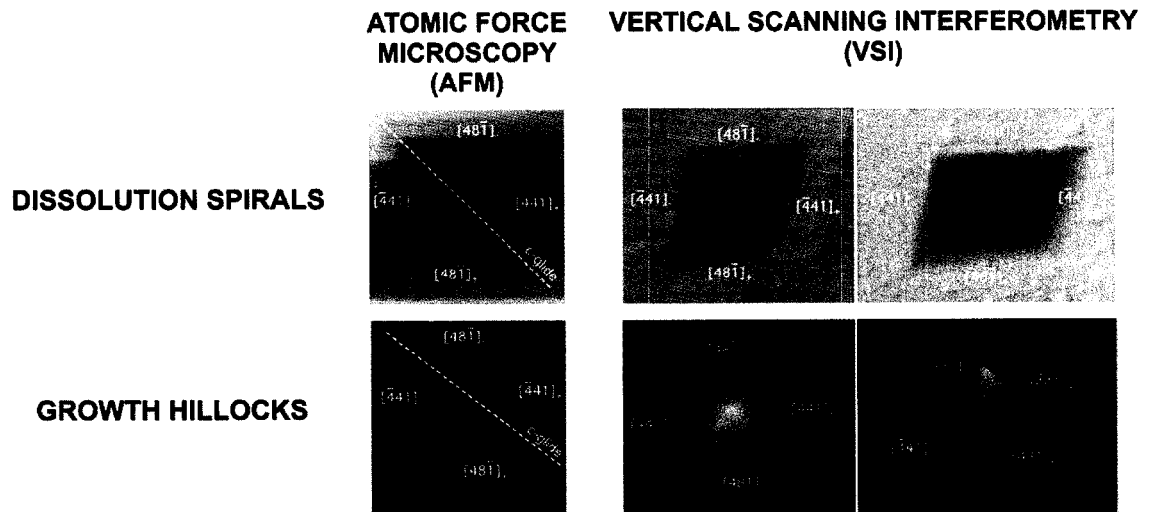


Figure 2.1 – Calcite Growth Hillocks and Dissolution Spirals Showing Anisotropy

AFM and VSI images of calcite growth hillocks and dissolution spirals, showing the crystallographic orientation of monomolecular surface steps. These representations also demonstrate the difference in resolution characteristic of the two techniques. The AFM images for dissolution and growth have scan sizes of 2x2 μm and 3x3 μm , respectively. The VSI images have respective scan sizes of 25x22 μm and 38x33 μm .

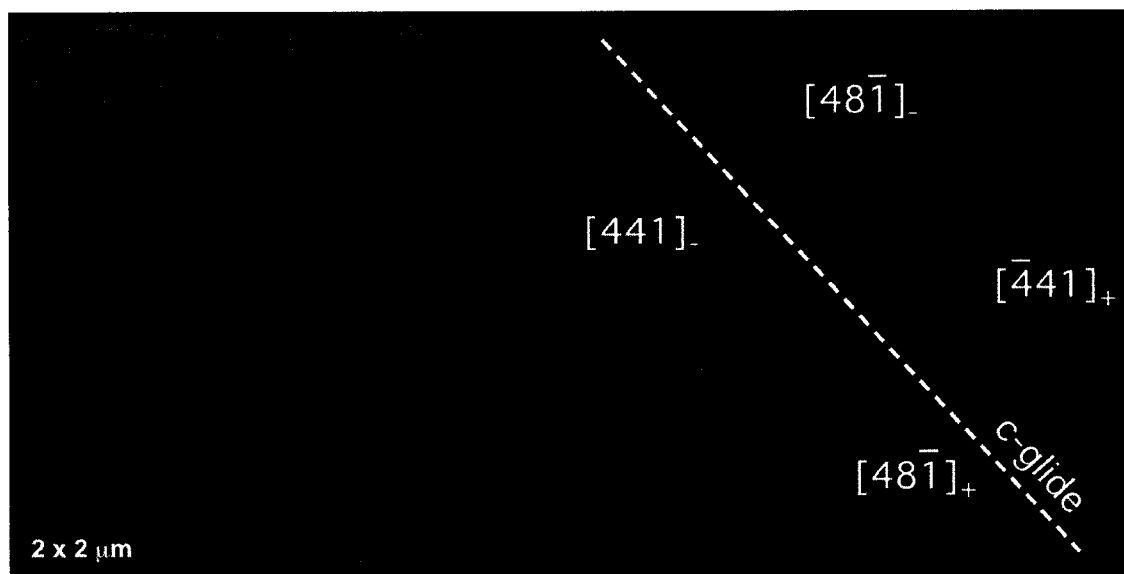


Figure 2.2 – AFM Image of a Calcite Dissolution Spiral

Calcite dissolution spirals exhibit four vicinal faces that in turn are comprised of two pairs of crystallographically equivalent steps that are reflected across the *c*-glide plane. These steps, however, have nonequivalent molecular-scale step-edge geometries denoted as the positive ($[\bar{4}41]_+$ and $[48\bar{1}]_+$) and negative ($[441]_-$ and $[48\bar{1}]_-$) step directions. This anisotropy in step-edge structure results in the different terrace widths evident on this dissolution spiral. Changes in chemistry over time produced the different terrace widths (step-spacings) evident at the bottom 2 microns of this etch pit.

carbonate anions cause the ‘positive steps’ to exhibit a step-edge geometry that is obtuse with respect to the cleavage plane, while the ‘negative steps’ form an acute angle with the cleavage surface. This anisotropy in step-edge structure often results in differential step velocities for the two step-types and accounts for the non-equivalent terrace widths evident on many dissolution spirals as well as differences in etch pit geometry.

Accordingly, anisotropic dissolution is common for calcite, whereby one step-type moves significantly faster than the other step-type and thus is responsible for a greater amount of dissolution. In the absence of step velocity measurements for the two step-types, the anisotropy of a dissolution spiral can be determined by measuring the angle (ϕ) created by the intersection of the positive (+) and negative (-) step-types. For instance, when $\phi > 180^\circ$, the (-) steps travel at a faster rate than the (+) steps and account for the majority of dissolution. Conversely, when $\phi < 180^\circ$ the (+) steps travel at a faster rate than the (-) steps and account for the majority of dissolution. When $\phi = 180^\circ$, isotropic growth predominates as both step-types travel at the same rate and make equivalent contributions to CaCO_3 dissolution. Accordingly, empirical measurements of calcite dissolution rates on dissolution spirals are made in the context of crystallographic orientation allowing for the elucidation of the mechanisms of rate modification by solutions of varying ionic ratios.

2.3.2 Saturation Controls: The Role of Saturation State in Anisotropy

In order to understand how changes in $\text{Ca}^{2+}/\text{CO}_3^{2-}$ concentration ratio at constant saturation affect calcite dissolution, it is necessary to first establish the role of saturation

state in calcite dissolution. Accordingly, calcite dissolution spirals were grown at several near-equilibrium saturation states while maintaining a constant $\text{Ca}^{2+}/\text{CO}_3^{2-}$ concentration ratio equal to 1 (Table 2.2, Fig. 2.3). As expected, steps speeds were generally measured to increase with increasing undersaturation (Fig. 2.4). Coincidentally, the period of spiral rotation decreased (Fig. 2.5), as the dislocation source produced steps at faster rates.

These coupled processes, produced greater calculated rates of dissolution as the degree of undersaturation increased (Fig. 2.6). Along with this expected result of changes in saturation state on calcite dissolution kinetics was an unexpected result as well. In contrast to the results found for growth (Chapter 1), changes in the degree of undersaturation at constant $\text{Ca}^{2+}/\text{CO}_3^{2-}$ concentration ratio were found to have a strong effect on step velocity anisotropy (Fig. 2.7) and the geometry of the dissolution spiral (Fig. 2.3). These effects resulted from a much greater sensitivity of positive (+) step velocities to changes in saturation state than were exhibited by the negative (-) steps. Further from equilibrium, (+) step rates were found to move nearly twice as fast as (-) step speeds (Fig. 2.4). However, as the degree of undersaturation decreased, the (+) step speeds decreased rapidly while the (-) step velocities decreased only marginally, and in some cases were measured to slightly increase. In solutions that were ten times undersaturated ($\Omega = 0.1$), the (+) step only moved 65% as fast as the (-) step-type. Further decreases in undersaturation produced positive step speeds that were only a third as fast as the (-) step-types. This surprising reversal in step velocity anisotropy produced reversed hillock geometries (Fig. 2.3), as the intersecting angle between the two step-types changed from greater than 180° under near equilibrium conditions to less than 180° further from equilibrium. The reversal in step migration rates also produced a reversal in

Table 2.2 – AFM Data for the Saturation Controls and Ratio Experiments

Solution ID	Ω	$\text{Ca}^{2+}/\text{CO}_3^{2-}$ Ratio	ϕ	Terrace Width (nm)			Step Velocity (nm/s)				Period (s)	Slope ($\times 10^{-3}$)		BCF Rate ($\times 10^{-9}$ nm/s)
				T_+	T_-	T_+/T_-	v_+	v_-	v_+/v_-	V_{sum}		P_+	P_-	
control 1-1	0.26	1.0	204	4.0	12.9	0.31	0.23	0.75	0.31	0.98	17.2	78	24	18.0
control 1-2	0.104	1.0	191	5.1	7.8	0.65	0.35	0.54	0.65	0.89	14.4	61	40	21.6
control 1-3	0.041	1.0	180	7.8	5.6	1.4	0.99	0.71	1.4	1.70	7.9	40	55	39.1
control 1-4	0.010	1.0	170	9.0	4.9	1.8	1.14	0.62	1.8	1.76	7.9	34	63	39.1
ratio 1-1	0.104	0.003	227	0.4	18.2	0.02	0.01	0.52	0.02	0.53	35.0	775	17	8.8
ratio 1-2	0.104	0.03	223	1.0	31.0	0.03	0.02	0.61	0.03	0.63	50.8	310	10	6.1
ratio 1-3	0.104	0.30	208	3.4	14.8	0.23	0.13	0.57	0.23	0.70	26.0	91	21	12.0
ratio 1-4	0.104	1.0	203	2.9	14.1	0.21	0.19	0.93	0.20	1.12	15.2	107	22	20.5
ratio 1-5	0.104	3.0	167	19.3	13.5	1.43	0.96	0.67	1.43	1.63	20.1	16	23	15.4
ratio 1-6	0.104	30.3	144	23.6	11.5	2.05	1.15	0.56	2.05	1.71	20.5	13	27	15.1
ratio 2-1	0.104	0.002	241	0.7	34.4	0.02	0.01	0.51	0.02	0.52	67.5	442	9	4.6
ratio 2-2	0.104	0.02	234	1.2	19.4	0.06	0.04	0.66	0.06	0.70	29.4	258	16	10.6
ratio 2-3	0.104	0.20	200	5.0	9.4	0.53	0.36	0.68	0.53	1.04	13.8	62	33	22.4
ratio 2-4	0.104	1.0	191	5.1	7.8	0.65	0.35	0.54	0.65	0.89	14.4	61	40	21.6
ratio 2-5	0.104	5.0	181	8.3	10.7	0.78	0.54	0.70	0.77	1.24	15.3	37	29	20.3
ratio 2-6	0.104	49	198	12.6	8.6	0.58	0.66	0.45	1.5	1.11	19.1	24	36	16.2
ratio 2-7	0.104	496	164	16.1	7.2	2.2	0.85	0.38	2.2	1.23	18.9	19	43	16.3

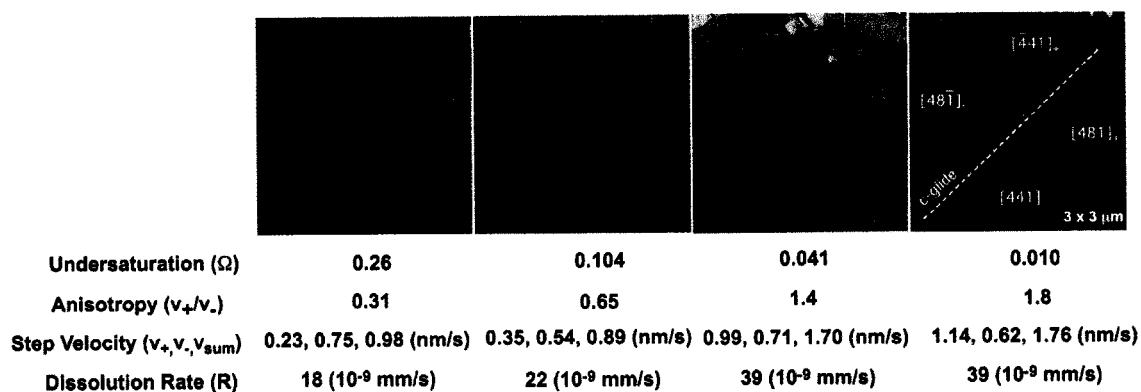


Figure 2.3 – Calcite Dissolution Spirals Grown Under Different Saturation States at Constant $\text{Ca}^{2+}/\text{CO}_3^{2-}$ Concentration Ratio Equal to 1.

Measured step speeds and step generation rates increased with increasing undersaturation, producing greater calculated rates of dissolution. Changes in the degree of undersaturation at constant $\text{Ca}^{2+}/\text{CO}_3^{2-}$ concentration ratio were also found to have a strong effect on step velocity anisotropy and the geometry of the dissolution spiral.

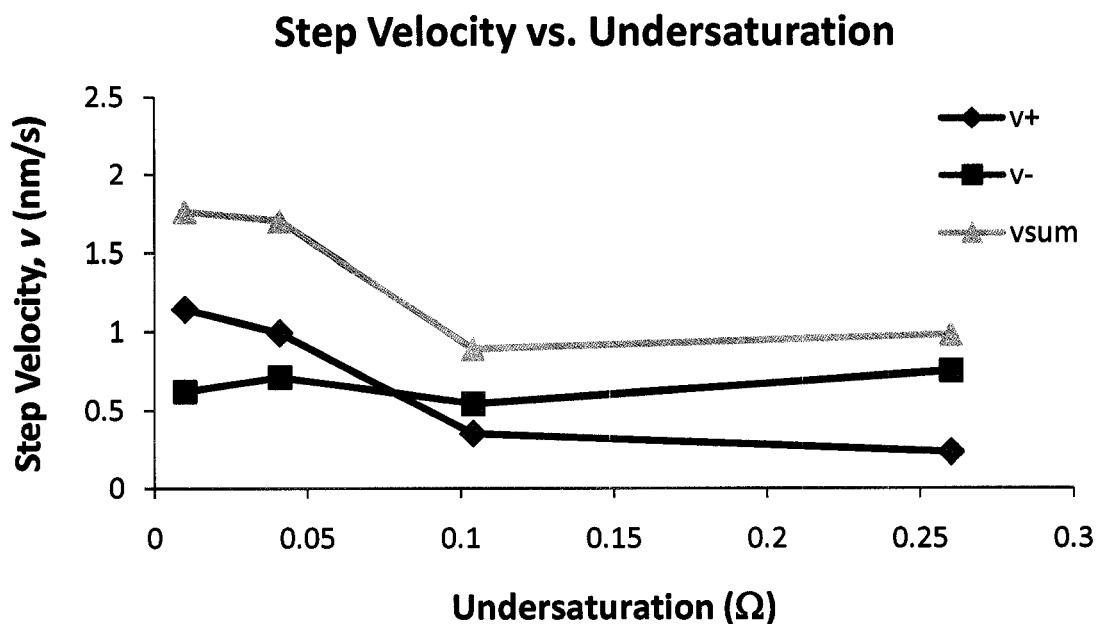


Figure 2.4 – Step Velocity Versus Undersaturation at Constant $\text{Ca}^{2+}/\text{CO}_3^{2-}$ Concentration Ratio

Steps speeds were generally measured to increase with increasing undersaturation. Further from equilibrium, (+) step rates were found to move nearly twice as fast as (-) step speeds. However, as the degree of undersaturation decreased, the (+) step speeds decreased rapidly while the (-) step velocities decreased only marginally, and in some cases were measured to slightly increase. This produced a surprising reversal in step velocity anisotropy.

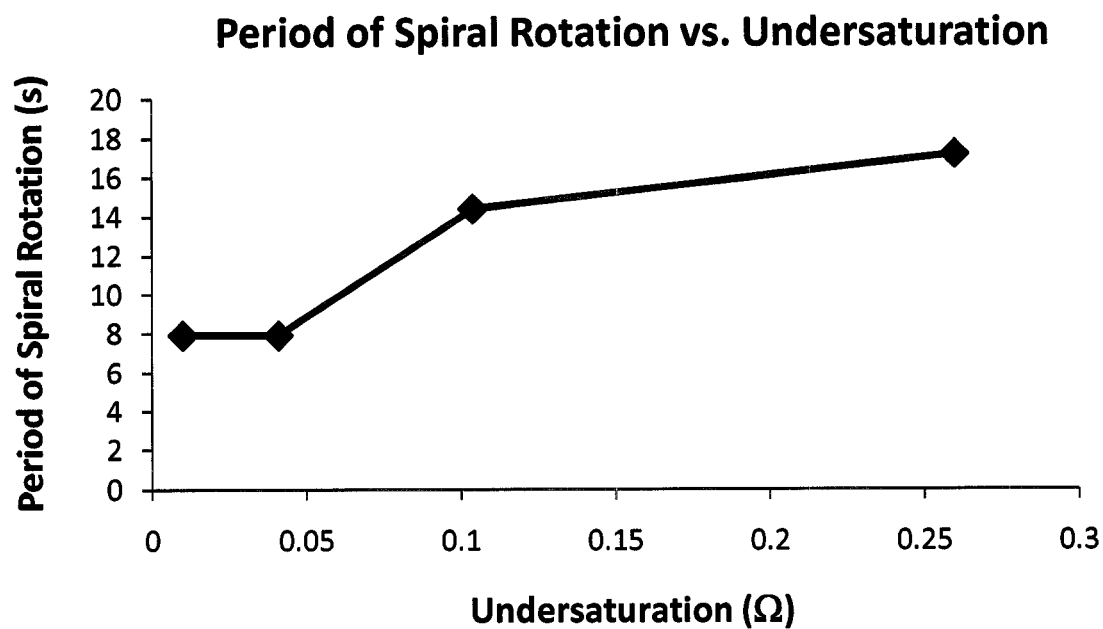


Figure 2.5 – Period of Spiral Rotation Versus Undersaturation at Constant $\text{Ca}^{2+}/\text{CO}_3^{2-}$ Concentration Ratio

The period of spiral rotation was measured to decrease with increasing undersaturation. This increase in the rate of spiral rotation with increasing undersaturation resulted in higher step production further from equilibrium.

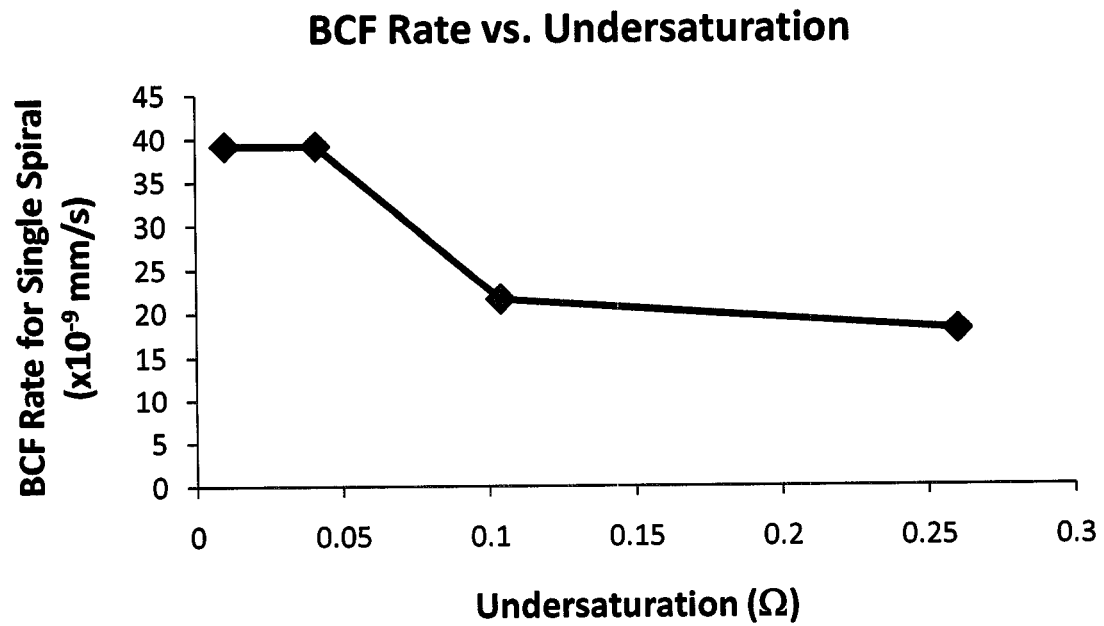


Figure 2.6 – BCF Dissolution Rate Versus Undersaturation at Constant $\text{Ca}^{2+}/\text{CO}_3^{2-}$ Concentration Ratio

Calculated BCF rates of calcite dissolution increased with increasing undersaturation due to the combined contributions of increased step migration rates and increased step generation rates at the dislocation source.

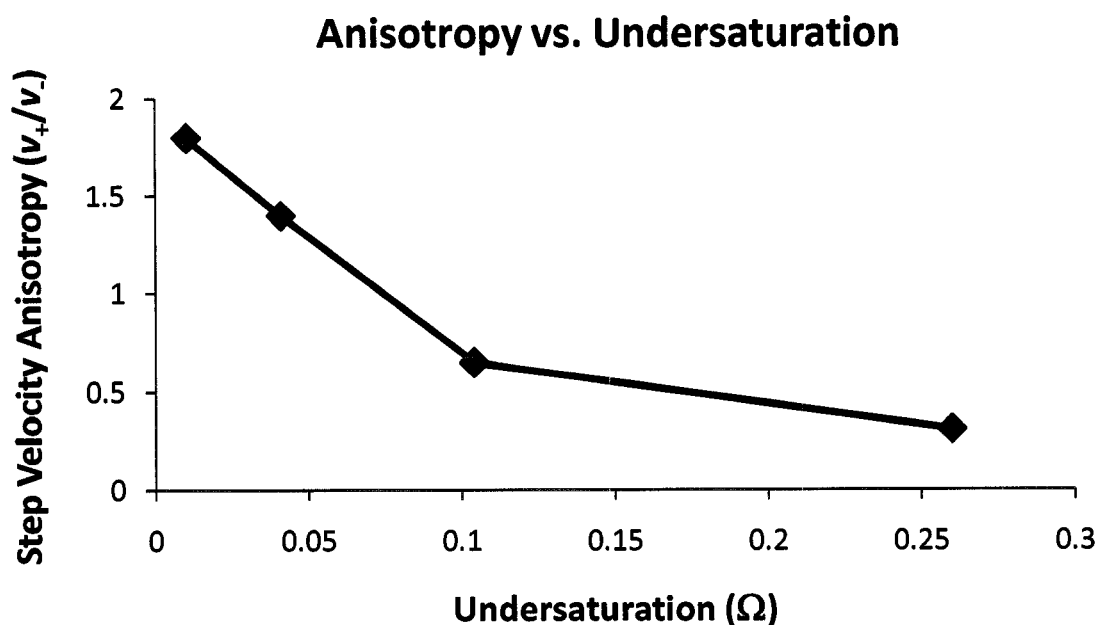


Figure 2.7 – Step Velocity Anisotropy Versus Undersaturation at Constant $\text{Ca}^{2+}/\text{CO}_3^{2-}$ Concentration Ratio

Changes in the degree of undersaturation at constant $\text{Ca}^{2+}/\text{CO}_3^{2-}$ concentration ratio were found to have a strong effect on step velocity anisotropy. These effects resulted from a much greater sensitivity of positive (+) step velocities to changes in saturation state than were exhibited by the negative (-) steps. Further from equilibrium, (+) step rates were found to move nearly twice as fast as (-) step speeds. However, as the degree of undersaturation decreased, the (+) step speeds decreased rapidly while the (-) step velocities decreased only marginally, and in some cases were measured to slightly increase. In solutions that were ten times undersaturated ($\Omega = 0.1$), the (+) step only moved 65% as fast as the (-) step-type. Further decreases in undersaturation produced positive step speeds that were only a third as fast as the (-) step-types.

the three-dimensional profile of the dissolution spiral. Closer to equilibrium, the (+) vicinal face exhibited a much steeper slope than the (-) vicinal face, due to decreased step velocities exhibited by those steps (Fig. 2.8). However, further from equilibrium the (-) vicinal face was much steeper than the (+) vicinal face due to faster (+) step velocities under those conditions. Accordingly, measurements of step dynamics clearly demonstrates that the saturation state determines the anisotropy of step kinetics during calcite dissolution, with (-) steps moving faster than (+) steps under near-equilibrium conditions and (+) steps moving faster than (-) steps further from equilibrium. More importantly, these results may indicate a differential role for the cation (Ca^{2+}) and anion (CO_3^{2-}) during dissolution. Previous AFM studies have shown that the presence of inorganic carbon (CO_3^{2-} species) in solution may preferentially inhibit the movement of (+) steps during layer-by-layer calcite dissolution (Lea et al. 2001; Vinson et al. 2007). Since carbonate ion concentration increases with decreasing undersaturation, the dramatic change in the anisotropy of step-speeds by changes in saturation state may simply be the result of a coincident increase in inhibition of (+) step-types by carbonate ion (Fig. 2.9). In order to further explore the role of carbonate ion in calcite dissolution kinetics, calcite dissolution rates need to be measured at varying stoichiometric ratios at constant undersaturation.

2.3.3 Ratio Experiments: The Role of $\text{Ca}^{2+}/\text{CO}_3^{2-}$ Activity Ratio in Calcite Dissolution

The effect of stoichiometric ratio on calcite dissolution was investigated using AFM observations of calcite crystallization from solutions with strong variation in $\text{Ca}^{2+}/\text{CO}_3^{2-}$ concentration ratio and constant saturation state. Measurements of step dynamics and

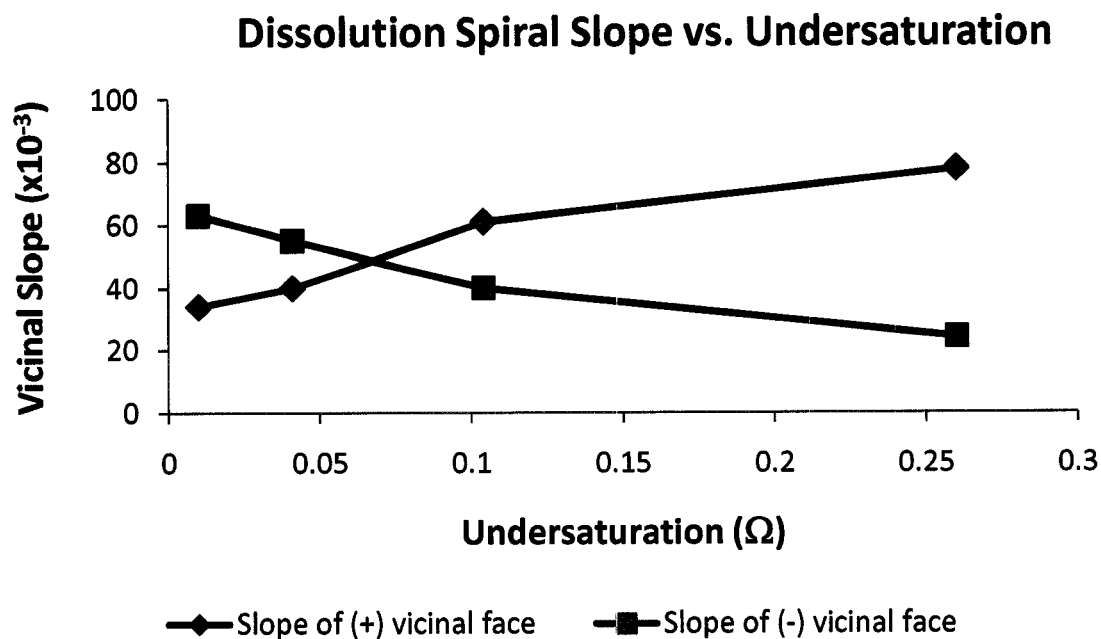


Figure 2.8 – Vicinal Slope Versus Undersaturation at Constant $\text{Ca}^{2+}/\text{CO}_3^{2-}$ Concentration Ratio

The reversal in the relative migration rates of the (+) and (-) step-types produced a reversal in the three-dimensional profile of the dissolution spiral. Closer to equilibrium, the (+) vicinal face exhibited a much steeper slope than the (-) vicinal face, due to decreased step velocities exhibited by those steps (Fig. 8). However, further from equilibrium the (-) vicinal face was much steeper than the (+) vicinal face due to faster (+) step velocities under those conditions.

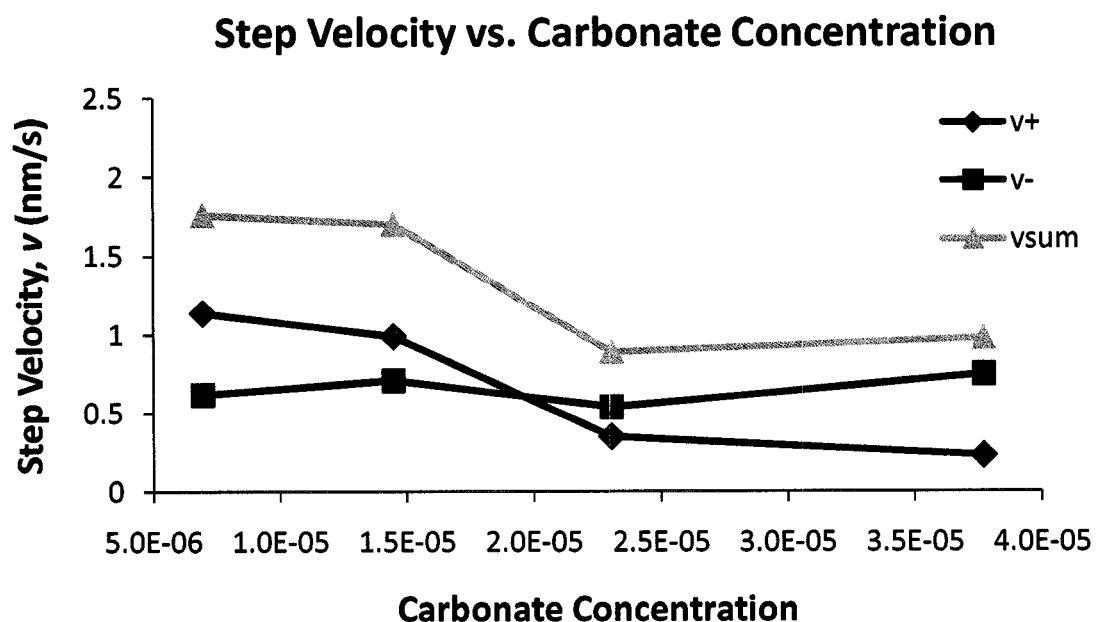


Figure 2.9 – Step Velocity Versus Carbonate Concentration at Constant $\text{Ca}^{2+}/\text{CO}_3^{2-}$ Concentration Ratio

Since carbonate ion concentration increases with decreasing undersaturation, the dramatic change in the anisotropy of step-speeds by changes in saturation state may simply be the result of a coincident increase in inhibition of (+) step-types by carbonate ion.

step production were found to be extremely sensitive to changes in the $\text{Ca}^{2+}/\text{CO}_3^{2-}$ concentration ratio, which in turn produced significant changes in etch pit geometry at different stoichiometric ratios (Fig. 2.10). The ionic ratio-dependent etch pit morphologies were primarily determined by the relative step speeds of the two step-types (Fig. 2.11). At a $\text{Ca}^{2+}/\text{CO}_3^{2-}$ ratio equal to one, the negative (-) steps moved faster than the positive (+) steps, creating an intersecting angle between the two step-types (ϕ) that was greater than 180° . As the $\text{Ca}^{2+}/\text{CO}_3^{2-}$ ratio was decreased below unity, the anisotropy in step velocity increased, with the negative step-types moving progressively faster than the (+) steps. However, at $\text{Ca}^{2+}/\text{CO}_3^{2-}$ ratios greater than one, the anisotropy quickly reversed with (+) steps moving increasingly faster than (-) steps, creating an intersecting angle (ϕ) that was less than 180° . Further insight into these changes in step-speed anisotropy and therefore the nature of step-specific ion interactions during calcite dissolution can be gained by individually examining the dynamics of each step-type in the context of varying ionic ratio. Of the two step-types, the dynamics of the (-) step-type was much less sensitive to changes in ionic ratio than the (+) step-type (Figs. 2.12 and 2.13). In the case of the first data set, the maximum (-) step velocity occurred at a ratio equal to one and decreased nearly symmetrically as the ratio moved towards increasingly nonstoichiometric values. The second data set yielded a maximum (-) step velocity at a ratio of 5, with a similar velocity decrease on either side of this value. These measurements seem to indicate that the stoichiometric ratio imposes a kinetic limitation on the dissolution rate at increasingly nonstoichiometric values. This finding matches the general behavior predicted for rates of step movement in nonstoichiometric solutions by Zhang and Nancollas (1998) as a result of the enhancement of lattice ion attachment rates

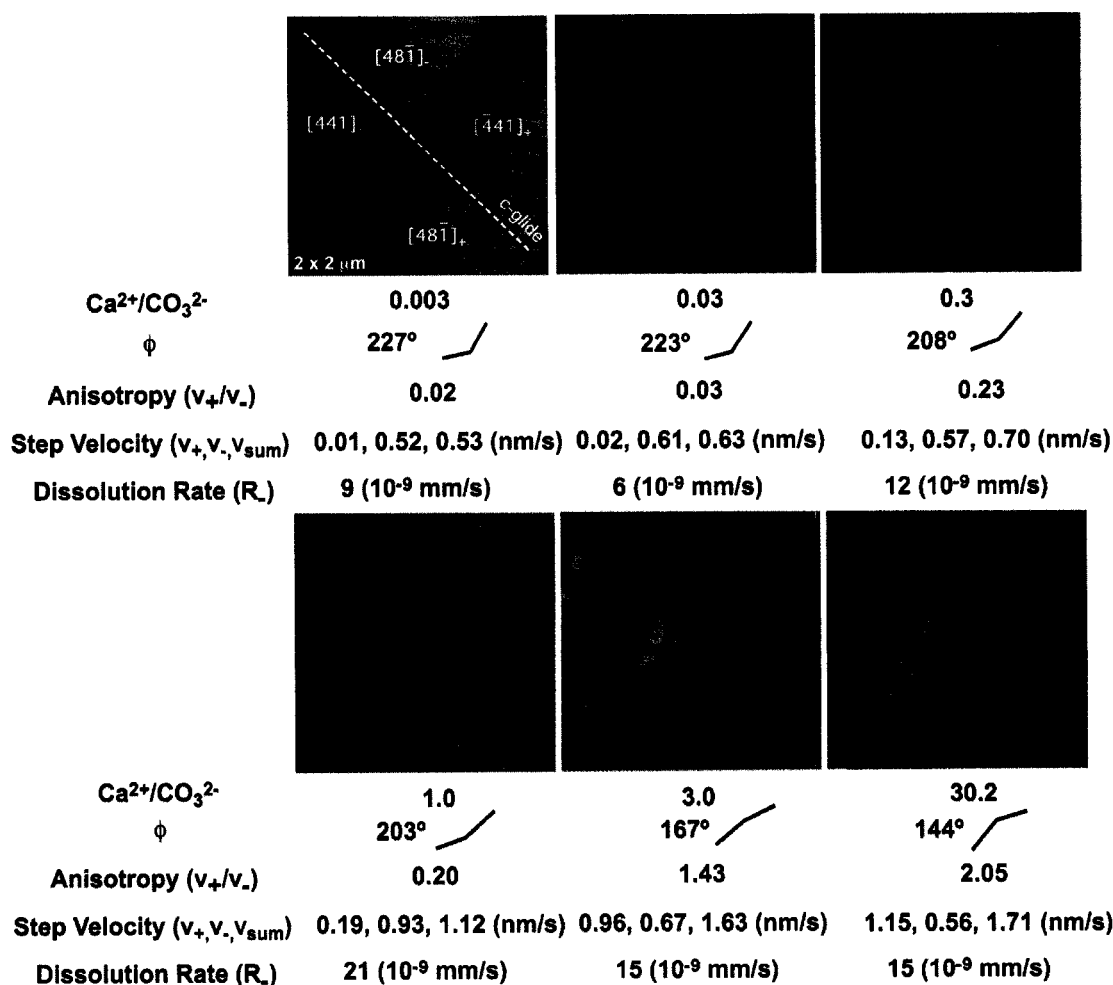


Figure 2.10 – Calcite Growth Hillocks Grown Under Different $\text{Ca}^{2+}/\text{CO}_3^{2-}$ Concentration Ratios at Constant Undersaturation State ($\Omega = 0.1$).

AFM images demonstrating the dependence of etch pit (dissolution spiral) morphology on $\text{Ca}^{2+}/\text{CO}_3^{2-}$ ratio for the ‘ratio 1-1’ through ‘ratio 1-6’ experiments (see Table 2.2). These images show the bottom 2x2 microns of the same dissolution spiral actively dissolving in solutions with different ionic ratios. At $\text{Ca}^{2+}/\text{CO}_3^{2-} = 1$, the negative (-) steps moved faster than the positive (+) steps creating an intersecting angle between the two step-types (ϕ) that was greater than 180°. At $\text{Ca}^{2+}/\text{CO}_3^{2-} < 1$, the anisotropy in step velocity increased with (-) step-types moving progressively faster than the (+) steps. However, at $\text{Ca}^{2+}/\text{CO}_3^{2-} > 1$, the anisotropy quickly reversed with (+) steps moving increasingly faster than the (-) steps, creating an intersecting angle (ϕ) that was less than 180°.

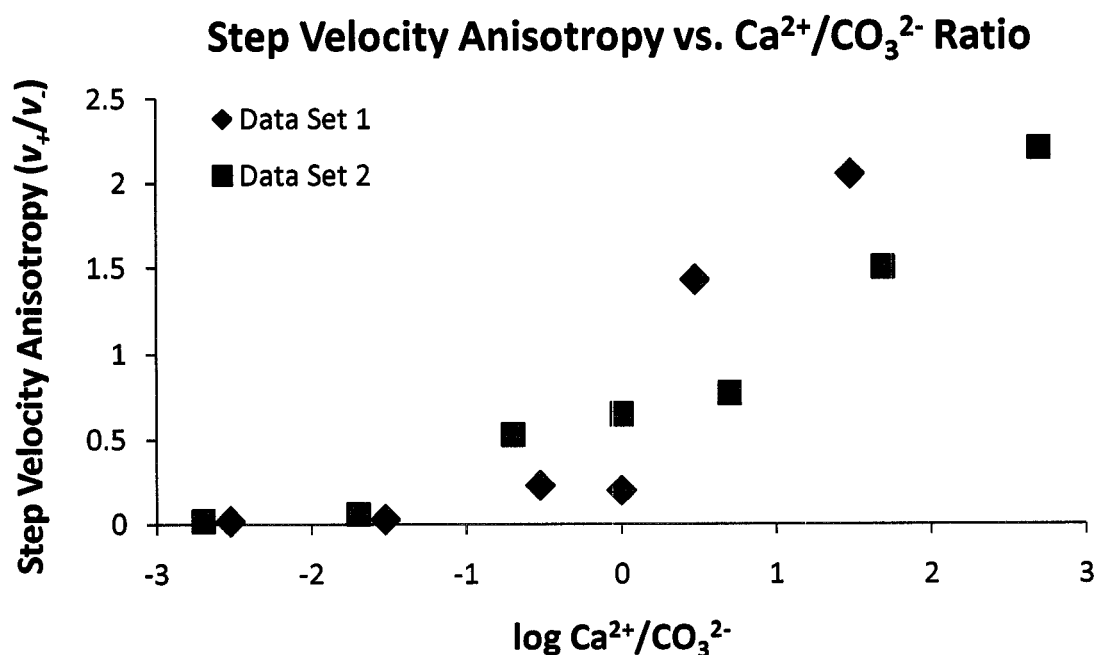


Figure 2.11 – Step Velocity Anisotropy Versus $\text{Ca}^{2+}/\text{CO}_3^{2-}$ Concentration Ratio at Constant Undersaturation

The relative speeds of the two step-types were controlled by the $\text{Ca}^{2+}/\text{CO}_3^{2-}$ ratio at constant undersaturation. At a $\text{Ca}^{2+}/\text{CO}_3^{2-}$ ratio equal to one, the negative (-) steps moved faster than the positive (+) steps. As the $\text{Ca}^{2+}/\text{CO}_3^{2-}$ ratio was decreased below unity, the anisotropy in step velocity increased, with the negative step-types moving progressively faster than the (+) steps. However, at $\text{Ca}^{2+}/\text{CO}_3^{2-}$ ratios greater than one, the anisotropy quickly reversed with (+) steps moving increasingly faster than (-) steps.

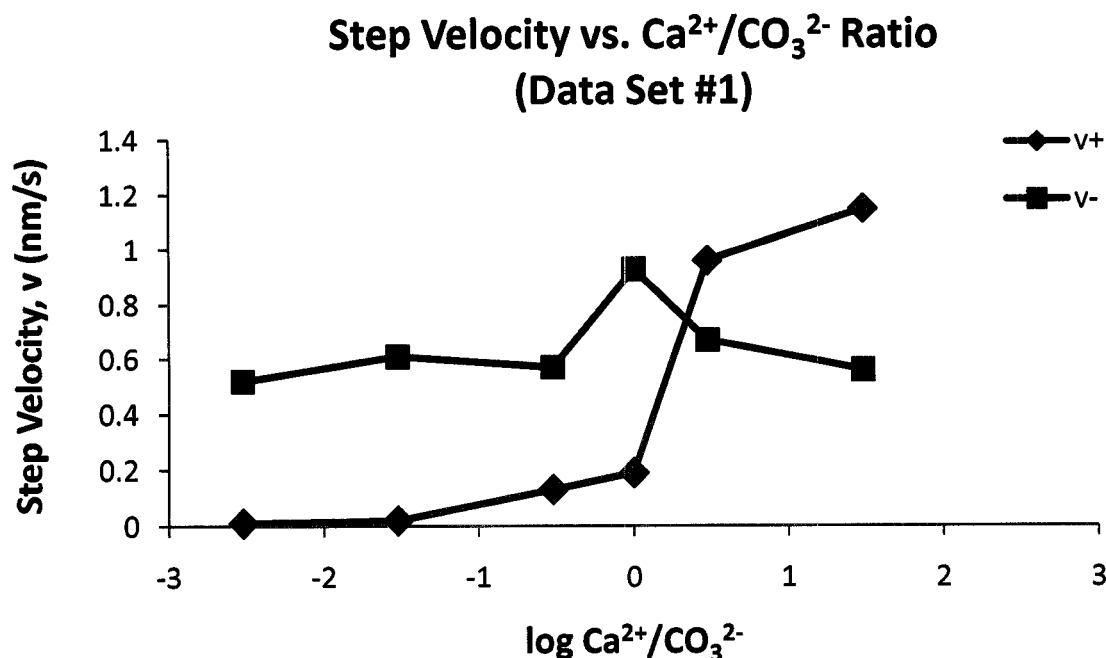


Figure 2.12 – Step Velocity Versus $\text{Ca}^{2+}/\text{CO}_3^{2-}$ Concentration Ratio at Constant Undersaturation

The velocity of the (-) step-type was much less sensitive to changes in $\text{Ca}^{2+}/\text{CO}_3^{2-}$ ratio than the (+) step-type. In Data Set #1, the maximum (-) step velocity occurred at a ratio equal to one and decreased nearly symmetrically as the ratio moved towards increasingly nonstoichiometric values. These measurements seem to indicate that the stoichiometric ratio imposes a kinetic limitation on the dissolution rate at increasingly nonstoichiometric values. In contrast, (+) step dynamics were much more sensitive to changes in ionic ratio. As the $\text{Ca}^{2+}/\text{CO}_3^{2-}$ ratio increased above one, (+) step velocities increased rapidly, while at $\text{Ca}^{2+}/\text{CO}_3^{2-}$ ratios below one (+) step velocities decreased equally rapidly. At low $\text{Ca}^{2+}/\text{CO}_3^{2-}$ ratios, nearly all calcite dissolution occurred as a result of the movement of (-) steps.

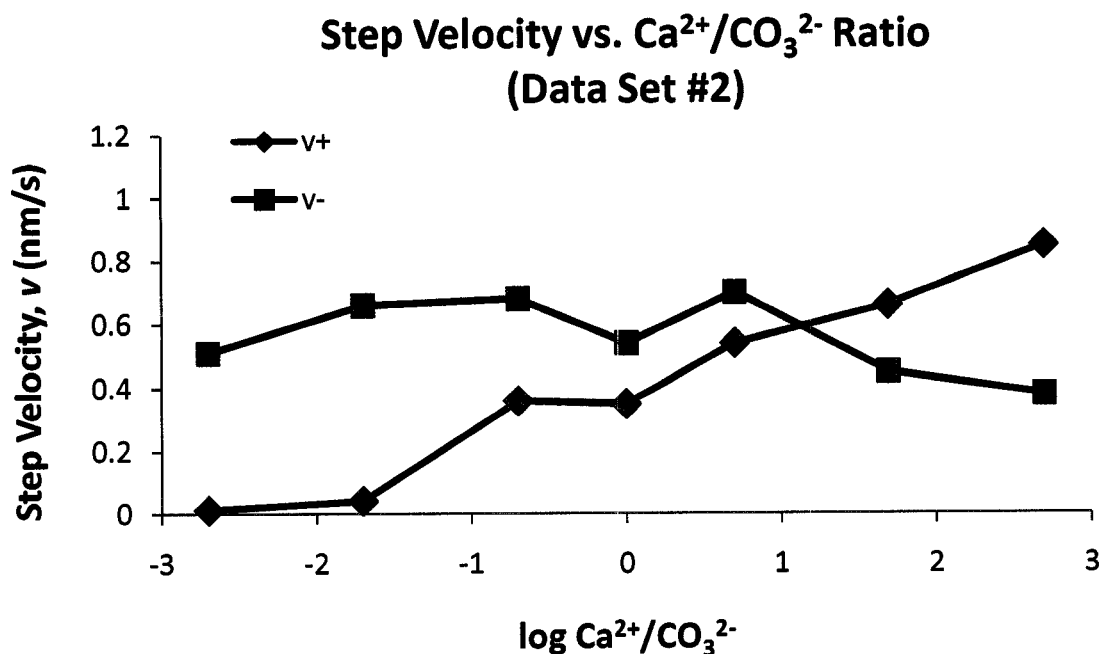


Figure 2.13 – Step Velocity Versus $\text{Ca}^{2+}/\text{CO}_3^{2-}$ Concentration Ratio at Constant Undersaturation

The velocity of the (-) step-type was much less sensitive to changes in $\text{Ca}^{2+}/\text{CO}_3^{2-}$ ratio than the (+) step-type. In Data Set #2, a maximum (-) step velocity occurred at a ratio of 5, with a similar velocity decrease on either side of this value. These measurements seem to indicate that the stoichiometric ratio imposes a kinetic limitation on the dissolution rate at increasingly nonstoichiometric values. In contrast, (+) step dynamics were much more sensitive to changes in ionic ratio. As the $\text{Ca}^{2+}/\text{CO}_3^{2-}$ ratio increased above one, (+) step velocities increased rapidly, while at $\text{Ca}^{2+}/\text{CO}_3^{2-}$ ratios below one (+) step velocities decreased equally rapidly. At low $\text{Ca}^{2+}/\text{CO}_3^{2-}$ ratios, nearly all calcite dissolution occurred as a result of the movement of (-) steps.

relative to detachment rates in the presence of excess cation or anion. In contrast, (+) step dynamics were much more sensitive to changes in ionic ratio. The velocity data for this step-type exhibited sigmoidal behavior with respect to $\text{Ca}^{2+}/\text{CO}_3^{2-}$ ratio. As the $\text{Ca}^{2+}/\text{CO}_3^{2-}$ ratio increased above one, (+) step velocities increased rapidly, while at $\text{Ca}^{2+}/\text{CO}_3^{2-}$ ratios below one (+) step velocities decreased equally rapidly. At low $\text{Ca}^{2+}/\text{CO}_3^{2-}$ ratios, nearly all calcite dissolution occurred as a result of the movement of (-) steps. This behavior is consistent with the previously demonstrated inhibition of (+) step movement in the presence of elevated carbonate ion concentrations (Lea et al., 2001; Vinson et al., 2007). The net sum of these differential effects on step dynamics for the two step-types can be quantified as the simple sum of the velocities of dissolution steps on the calcite surface, v_{sum} (Fig. 2.14). Due to the dominant sensitivity of the (+) steps to changes in $\text{Ca}^{2+}/\text{CO}_3^{2-}$ ratio, the sum of the dissolution step velocities (v_{sum}) exhibited a similar sigmoidal behavior as did the velocity of the (+) steps. Accordingly, the net movement of dissolution steps on the calcite surface increased dramatically with increasing $\text{Ca}^{2+}/\text{CO}_3^{2-}$. The step-specific measurements in this study further indicate that this relationship between $\text{Ca}^{2+}/\text{CO}_3^{2-}$ and step velocity likely results from the site-specific interaction of carbonate ions with kink-sites on the (+) step-type resulting in the inhibition of (+) steps at lower $\text{Ca}^{2+}/\text{CO}_3^{2-}$ ratios.

According to BCF theory, the overall dissolution rate at a dislocation etch pit is determined by the product of the monomolecular step velocities and the slope of the vicinal faces of the dissolution spiral. The slope is in turn determined by the ratio of how fast steps move away from the dislocation to the rate at which new steps are created at the

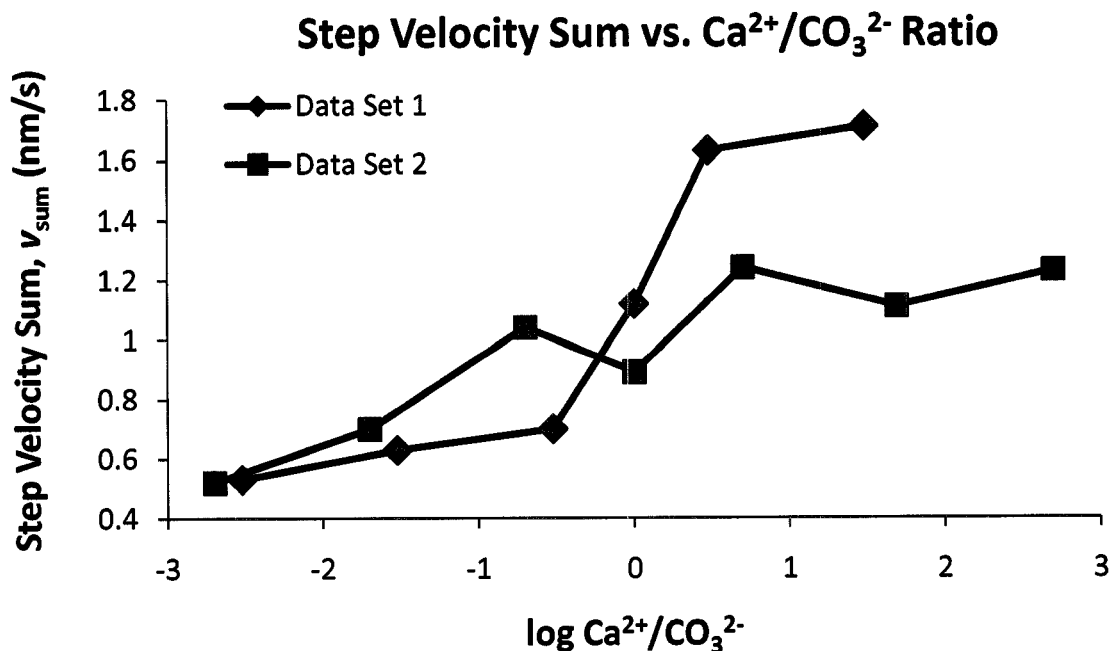


Figure 2.14 – Step Velocity Sum Versus $\text{Ca}^{2+}/\text{CO}_3^{2-}$ Concentration Ratio at Constant Undersaturation

The sum of the velocities of dissolution steps on the calcite surface, v_{sum} exhibited a similar sigmoidal behavior as did the velocity of (+) steps. Accordingly, the net movement of dissolution steps on the calcite surface increased dramatically with increasing $\text{Ca}^{2+}/\text{CO}_3^{2-}$. The step-specific measurements in this study further indicate that this relationship between $\text{Ca}^{2+}/\text{CO}_3^{2-}$ and step velocity likely results from the site-specific interaction of carbonate ions with kink-sites on the (+) step-type resulting in the inhibition of (+) steps at lower $\text{Ca}^{2+}/\text{CO}_3^{2-}$ ratios.

dislocation source. The faster the relative rates of step production to step velocity, the steeper the slope of the dissolution spiral. Accordingly, the independent measurement of vicinal slope and monomolecular step velocities allows for the calculation of the rate of step generation at the dislocation, expressed as the period of spiral rotation. Such measurements of the step production rate at the dislocation source were also found to be extremely sensitive to changes in $\text{Ca}^{2+}/\text{CO}_3^{2-}$ ratio at constant undersaturation (Fig. 2.15). In general, step production rates were measured to be fastest (shorter period) near a ratio of 1. (For data set 2, $\text{Ca}^{2+}/\text{CO}_3^{2-} = 0.2$ exhibited a slightly faster step production rate.) As the $\text{Ca}^{2+}/\text{CO}_3^{2-}$ ratio departed from one, step production decreased significantly. This decrease in step generation rates in nonstoichiometric solutions was asymmetric in nature, with step production decreasing much faster at low $\text{Ca}^{2+}/\text{CO}_3^{2-}$ ratios than at high $\text{Ca}^{2+}/\text{CO}_3^{2-}$ ratios. Possible insight into the mechanism underlying this kinetic behavior may be seen by plotting the period of spiral rotation versus step velocity anisotropy (Fig. 2.16). Because the low $\text{Ca}^{2+}/\text{CO}_3^{2-}$ ratios also exhibit the greatest step velocity anisotropy, there is a near linear relationship between the period of spiral rotation and step velocity anisotropy. This finding may indicate that strain at the dislocation source may be responsible for the slower step generation rates exhibited at lower ratios.

The combined contributions of step generation rate and step velocity to the overall rate of calcite dissolution (BCF rate) are plotted for the two data sets in Fig. 2.17. The highest overall rates were achieved at ionic ratios near one (stoichiometric solutions), for both data sets. When dissolution occurred in nonstoichiometric solutions, the rates were much reduced. At higher ratios, the faster step velocities (v_{sum}) were outweighed by the effects of longer period (slower step generation rates), resulting in reduced dissolution

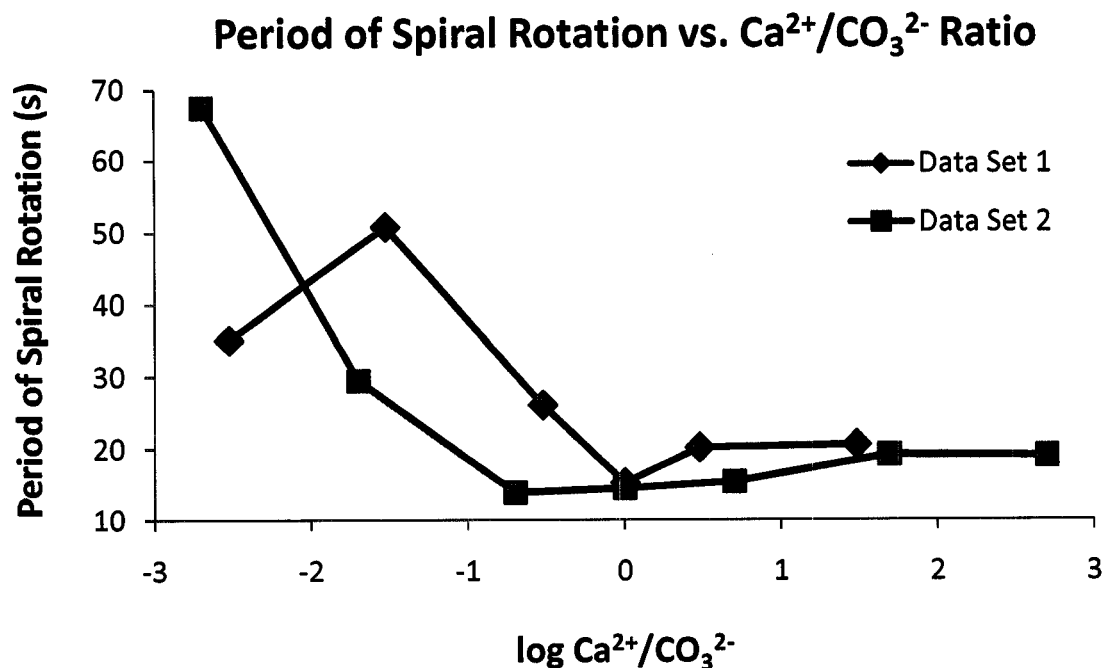


Figure 2.15 – Period of Spiral Rotation Versus $\text{Ca}^{2+}/\text{CO}_3^{2-}$ Concentration Ratio at Constant Undersaturation

Measurements of the step production rate at the dislocation source were found to be extremely sensitive to changes in $\text{Ca}^{2+}/\text{CO}_3^{2-}$ ratio at constant undersaturation. In general, step production rates were measured to be fastest (shorter period) near a ratio of 1. (For data set 2, $\text{Ca}^{2+}/\text{CO}_3^{2-} = 0.2$ exhibited a slightly faster step production rate.) As the $\text{Ca}^{2+}/\text{CO}_3^{2-}$ ratio departed from one, step production decreased significantly. This decrease in step generation rates in nonstoichiometric solutions was asymmetric in nature, with step production decreasing much faster at low $\text{Ca}^{2+}/\text{CO}_3^{2-}$ ratios than at high $\text{Ca}^{2+}/\text{CO}_3^{2-}$ ratios.

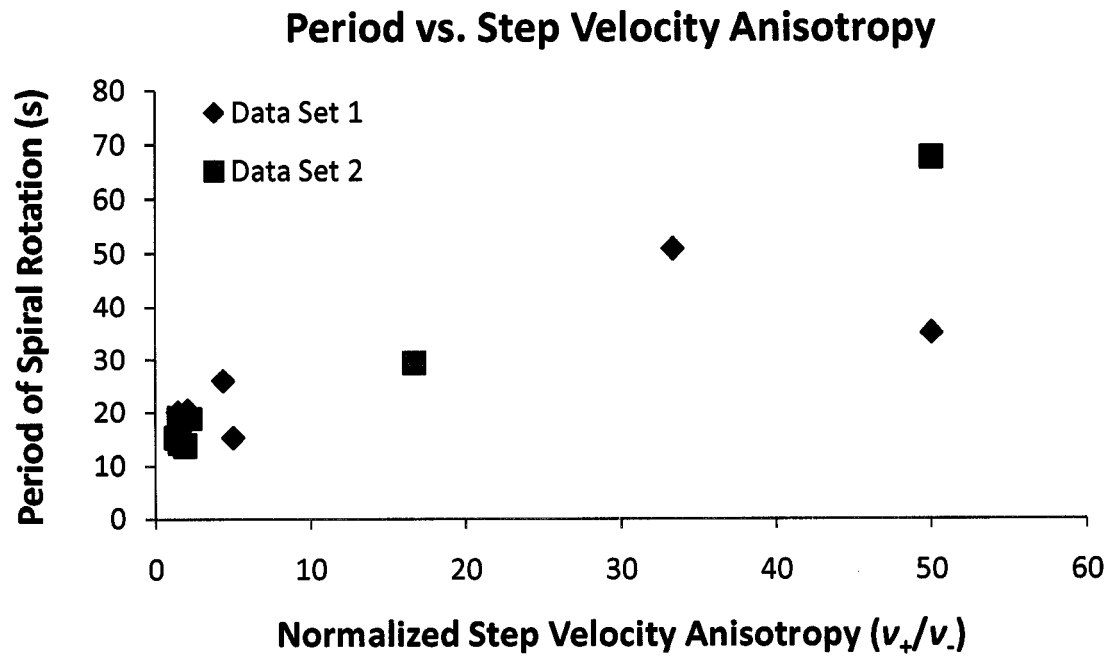


Figure 2.16 – Period of Spiral Rotation Versus Normalized Step Velocity Anisotropy at Constant Undersaturation

A plot of the period of spiral rotation versus step velocity anisotropy exhibits a near linear relationship between the period of spiral rotation and step velocity anisotropy.

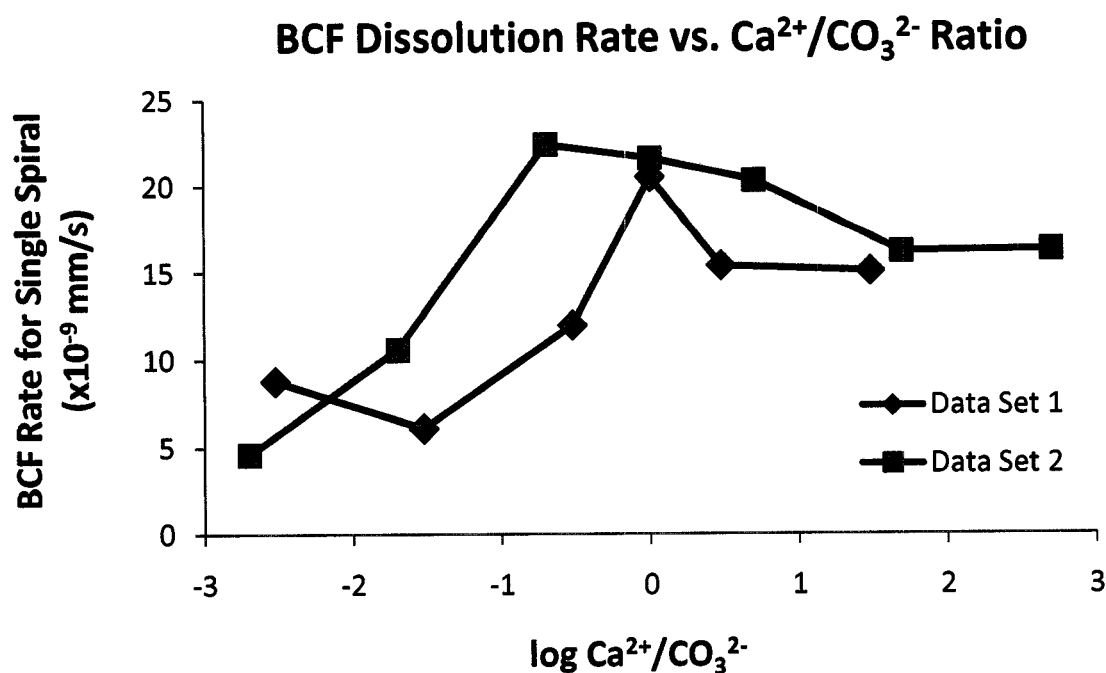


Figure 2.17 – BCF Dissolution Rate Versus $\text{Ca}^{2+}/\text{CO}_3^{2-}$ Concentration Ratio at Constant Undersaturation

The combined contributions of step generation rate and step velocity to the overall rate of calcite dissolution (BCF rate) are plotted for the two data sets. The highest overall rates were achieved at ionic ratios near one (stoichiometric solutions), for both data sets. When dissolution occurred in nonstoichiometric solutions, the rates were much reduced. At higher ratios, the faster step velocities (v_{sum}) were outweighed by the effects of longer period (slower step generation rates), resulting in reduced dissolution rates.

rates. It is clear from this data that the dominant contribution to the overall rate at stoichiometric ratios above one was the reduced step generation rate (longer period of spiral rotation), resulting in a kinetic limitation on dissolution at these nonstoichiometric solutions. However at the highest ratios, the change in step generation rate decreased and was balanced by increasing step velocities. Therefore, the decrease in dissolution rate under nonstoichiometric solutions above one was more pronounced at ratios near unity and leveled off at higher ratios. This trend in measured calcite dissolution rates was different than those rates measured in solutions with ionic ratios less than one. In these solutions, the sum of the step velocities (v_{sum}) decreased significantly due to increasing inhibition by carbonate ion on the (+) steps and due to kinetic limitations imposed on the (-) steps at nonstoichiometric ratios. Further, the step production rate decreased to a much larger degree under lower ratios. The combined effect of these two processes resulted in much lower calculated overall dissolution rates at ratios less than one.

It is clear from the measurements in this study that much of the modification of calcite dissolution rates in nonstoichiometric solutions occurs as a result of site-specific inhibition of the (+) step-type by carbonate ions. The magnitude of the role of carbonate ion in controlling overall dissolution rates can be assessed by plotting the measurements of this study relative to carbonate ion concentration for both the ratio experiments and saturation controls. Figures 2.18-2.23 demonstrate that the saturation control data follows the trend of the ratio experiments with respect to carbonate ion concentration, indicating that dissolution rates may be principally controlled by the concentration of carbonate ions under near-equilibrium conditions. Comparison of Figs. 2.18 and 2.19 show that the inhibition of surface steps by carbonate ion is site-specific in nature, being

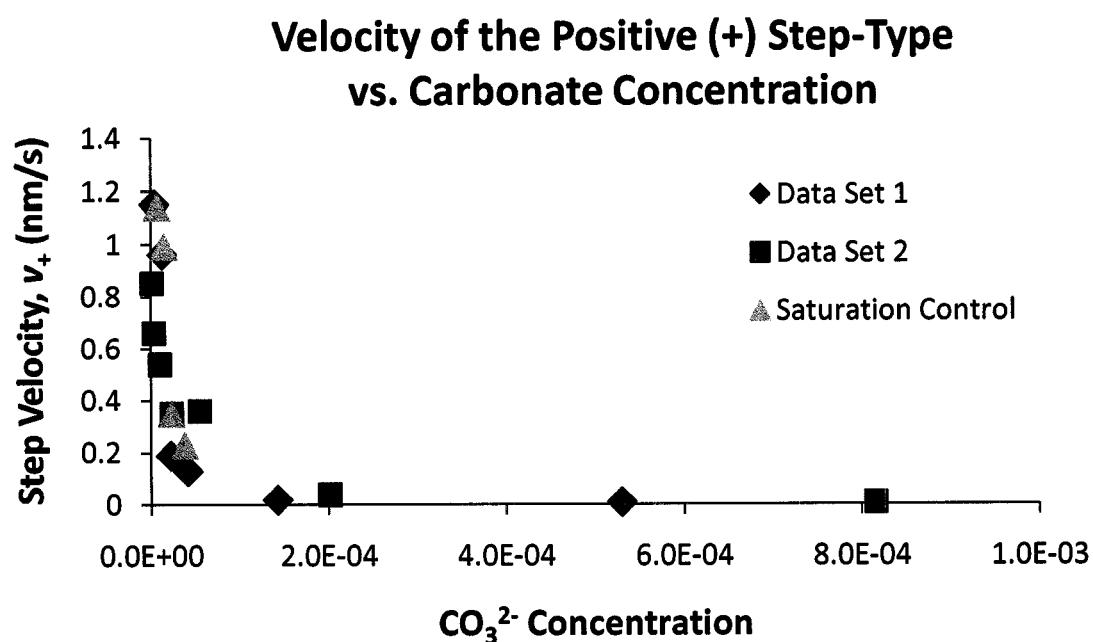


Figure 2.18 – Velocity of the Positive (+) Step-Type Versus Carbonate Concentration

Increasing carbonate ion concentrations result in reduced (+) step velocities. Comparison with Fig. 19 indicates that the inhibition of calcite dissolution by carbonate ion is site-specific in nature, being limited to the (+) step-type.

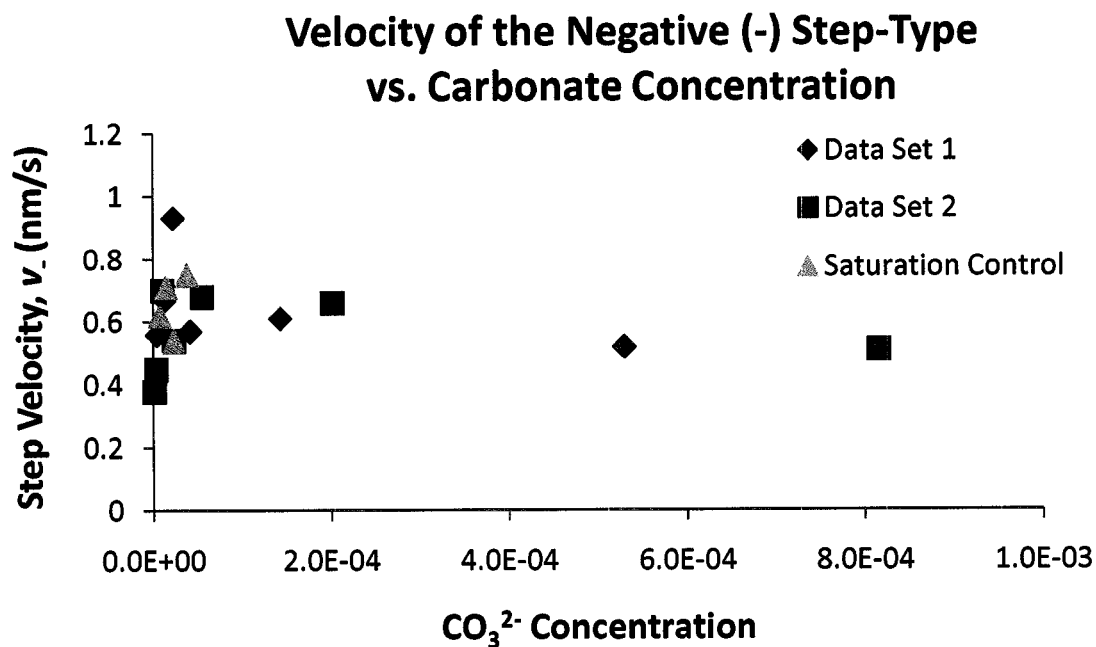


Figure 2.19 – Velocity of the Negative (-) Step-Type Versus Carbonate Concentration

Increasing carbonate concentration produces only a very small decrease in (-) step velocity. Comparison with Fig. 18 indicates that the inhibition of calcite dissolution by carbonate ion is site-specific in nature, being limited to the (+) step-type.

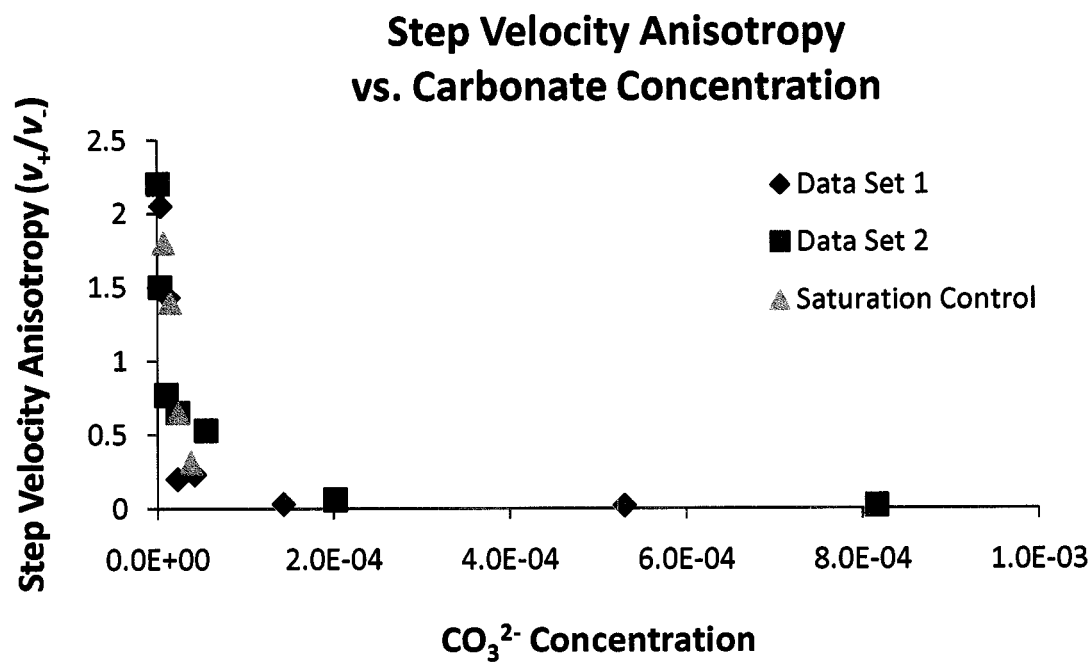


Figure 2.20 – Step Velocity Anisotropy Versus Carbonate Concentration

The anisotropy of step migration is controlled by carbonate ion concentration.

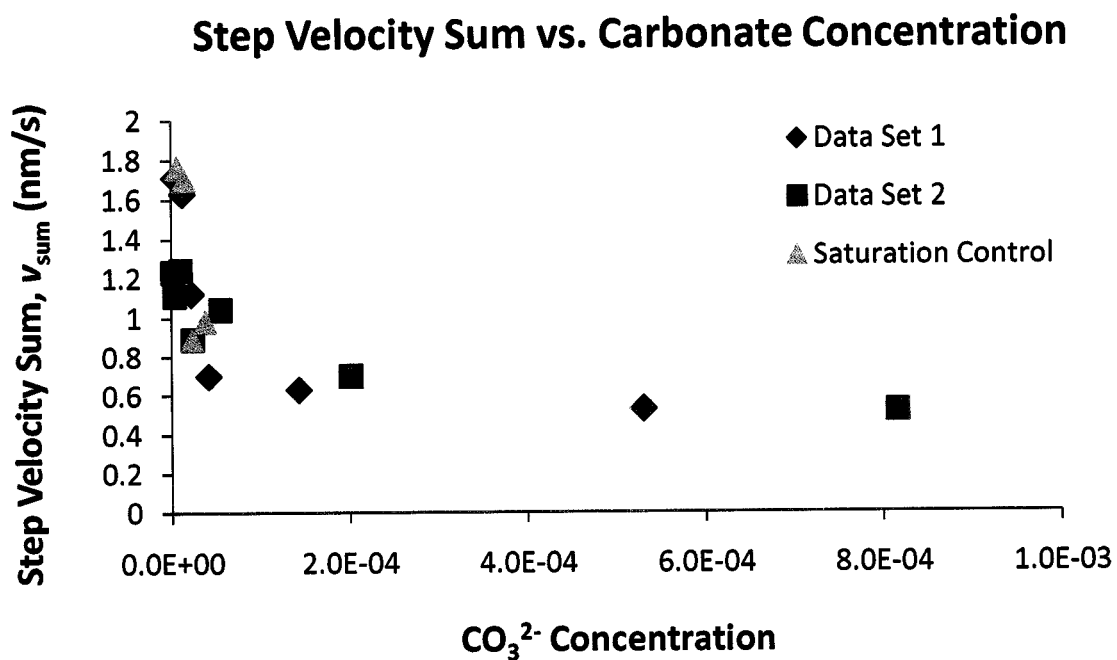


Figure 2.21 – Step Velocity Sum Versus Carbonate Concentration

This sum of step velocities on the calcite surface decreases with increasing carbonate ion concentration.

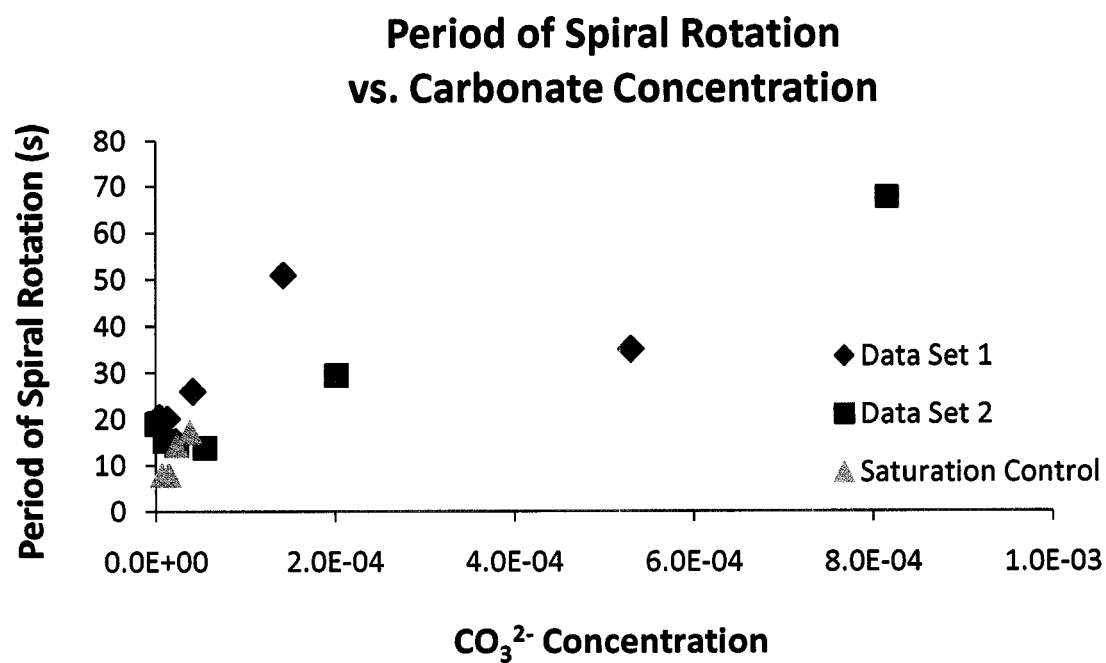


Figure 2.22 – Period of Spiral Rotation Versus Carbonate Concentration

The period of spiral rotation increases with increasing carbonate ion concentration, resulting in reduced step generation rates.

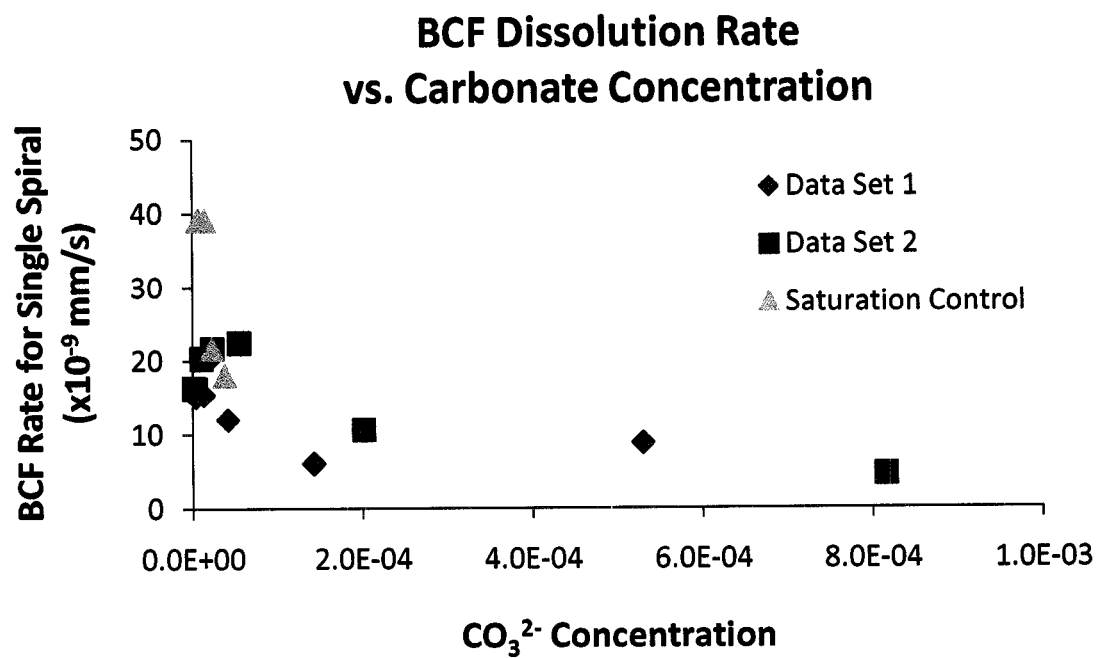


Figure 2.23 – BCF Dissolution Rate Versus Carbonate Concentration

Calculated BCF dissolution rates decrease with increasing carbonate ion concentration.

limited to the (+) step-type. Figure 2.20 shows that this site-specific control over the migration rates of the (+) step-type controls the anisotropy of step velocity on the calcite surface. Figures 2.21 and 2.22 show that the decrease in surface step velocities and step generation rates corresponds with increasing carbonate ion concentration, resulting in decreased calculated BCF spiral dissolution rates (Figure 2.23).

2.4 Conclusions

The results of this study demonstrate that solution stoichiometry plays a fundamental role in determining the dissolution rate of calcite under near-equilibrium conditions. For the first time, the interaction between monomolecular surface steps and the cation/anion ratio in carbonate solutions has been resolved yielding novel insight into the dominant mechanisms of calcite dissolution. Changes in the $\text{Ca}^{2+}/\text{CO}_3^{2-}$ ratio at constant undersaturation were shown to produce significant changes in the calcite dissolution rate that are normally only associated with changes in the saturation state. This rate modification occurred due to ratio-dependent changes in both monomolecular step velocities and step generation rates at screw dislocations. Step-specific velocity measurements revealed two primary mechanisms by which solution stoichiometry affected the migration rates of calcite surface steps. For the (-) step-type, nonstoichiometric solutions produced a kinetic limitation on dissolution due to an increase in the relative attachment rates of lattice ions at kink-sites as compared to detachment rates. In contrast, (+) steps appeared to be inhibited by the presence of carbonate ion, producing a non-symmetric relationship between step migration rates and solution stoichiometry. Accordingly, the results of this study demonstrate a differential

kinetic role for the cation and anion during dissolution. Dissolution rates are slowest at low $\text{Ca}^{2+}/\text{CO}_3^{2-}$ ratios, corresponding to high carbonate concentrations. This control over dissolution rates by ionic ratio can be further reduced to site-specific inhibition of (+) steps by carbonate ion. However, changes in the step generation rate at dislocations dominated the BCF-calculated dissolution rates. Here again, the presence of excess carbonate ion produced disproportionately slower rates of step production as compared to higher $\text{Ca}^{2+}/\text{CO}_3^{2-}$ ratios.

While much of the effect of solution stoichiometry on calcite dissolution rates can be assigned to site-specific inhibition by carbonate ion, this study also provides clear evidence of further kinetic limitations imposed by nonstoichiometric solutions on calcite dissolution. Measured rates of both (-) step advancement and step generation reached a maximum at a $\text{Ca}^{2+}/\text{CO}_3^{2-}$ ratio equal to one (stoichiometric ratio). Nonstoichiometric ratios produced slower rates that were nearly symmetric on either side of unity. These observations confirm the predictions of Zhang and Nancollas (1998) that under near-equilibrium conditions, the presence of excess lattice ions in solution may increase the rates of attachment to kink-sites enough so as to effectively compete with detachment rates, resulting in reduced dissolution rates. This result demonstrates the importance of conducting dissolution experiments close to equilibrium. Experimental designs that measure dissolution rates far from equilibrium with the intention of extrapolating saturation-based rate laws to natural systems will not account for this important mechanistic result.

At all solution stoichiometries, $\text{Ca}^{2+}/\text{CO}_3^{2-}$ ratio-induced changes in step production rates dominated BCF-calculated dissolution rates when compared to changes

in monomolecular step velocities. This important result indicates that surface defects not only enhance dissolution rates by providing a continuous source of steps, but are a means by which rates are modified by specific interactions with chemical species. Accordingly, the relationship between solution stoichiometry and calcite dissolution rates demonstrated in this study could not have been predicted from consideration of bulk chemistry alone, but instead require special consideration of the surface and its interaction with specific chemical species in solution.

The results of this study demonstrate that the mechanisms underlying calcite dissolution are more complicated than previously thought. Indeed, a major source of error and variation in empirically-determined calcite dissolution rates may be related to differences in ionic ratio and specific interactions between the surface and key ionic species. Caution should especially be exercised when applying rate laws that were derived far from equilibrium to near-equilibrium natural systems, because they do not account for kinetic limitations imposed by excess lattice ions or the disproportionate role of dislocation-controlled step generation rates in determining dissolution rates. In the future, saturation-based rate laws describing calcite dissolution should be modified to include the relative concentrations of reactive species so as to account for the kinetic effects imposed by nonstoichiometric solutions and for rate inhibition by carbonate ion.

If the role of solution stoichiometry ($\text{Ca}^{2+}/\text{CO}_3^{2-}$ ratio) in determining calcite dissolution rates demonstrated in this study can be confirmed for seawater systems, it may impact our understanding of how changes in the CCD reflect independent variations in seawater $[\text{Ca}^{2+}]$ and $[\text{CO}_3^{2-}]$ during the geologic past, which would in turn influence paleo- pCO_2 reconstructions. The results of this study are also interesting in the

context of the future impacts of ocean acidification. While it is clear that the $\text{Ca}^{2+}/\text{CO}_3^{2-}$ ratio changes along with the saturation state during ocean acidification, it is less clear whether the role of solution stoichiometry may enhance or mitigate the effects of decreased saturation state on carbonate dissolution. However, the potential role of solution stoichiometry should be considered in determining the potential impacts of anthropogenic forcing of atmospheric CO_2 or the potential consequences of deep-sea injection as a possible carbon mitigation strategy.

2.5 Chapter Appendix

2.5.1 *The Difference Between Growth and Dissolution at Near-Equilibrium Conditions*

The dissolution experiments presented in this study were conducted close to equilibrium, at precisely the same distance from $\Delta G = 0$ as previously published growth experiments (Davis et al., in preparation). This allows for a rare comparison between growth and dissolution processes at the same distance from equilibrium. The measured step velocities were much slower during dissolution than during growth at the same distance from equilibrium. Growth steps were 20 times faster than the dissolution steps under these conditions. However, the period of spiral rotation was only about 1.5 times faster. Therefore, the ratio at which steps were produced to the speed at which steps moved away from the dislocations was much greater for dissolution than for growth. This smaller ratio of step velocity to step generation rates created much steeper etch pits than growth spirals at the same distance from equilibrium. Accordingly, the step spacing (terrace width) of the dissolution steps were much smaller than the growth steps. While

the growth steps were spaced at an average of 100 nm, the dissolution steps were only spaced about 7 nm on average. This small step spacing made the dissolution spirals (etch pits) much steeper than growth hillocks grown at the equivalent distance from equilibrium. The slopes for dissolution spirals was an order of magnitude greater than for the growth hillocks (e.g., 40×10^{-3} versus 4×10^{-3}). Therefore the difference in calculated BCF rates between growth and dissolution are fairly comparable at 30×10^{-9} mm/s for growth and 20×10^{-9} mm/s for dissolution. However the nature of the growth and dissolution processes were very different when viewed using VSI after 13 hours of reaction time. While no global dissolution was detectable after this period of reaction, a global growth rate was easily measured. This was because dissolution was restricted to deep etch pits rather than shallow growth hillocks with high step speeds. The dissolution steps did not reach the edges of the crystal (or mask) at a rate approaching that of the growth steps, when the defect density is low enough that adjacent dissolution spirals do not coalesce. The kinetic results for dissolution and growth are very different as a function of both saturation state and solution stoichiometry. Therefore the results of these experiments argue that dissolution and growth are very different processes at the near-molecular and surface scales and may require different theoretical frameworks for their complete explanation.

CHAPTER 3. Quantifying the Relationship Between Microbial Attachment and Mineral Surface Dynamics Using Vertical Scanning Interferometry (VSI)

This chapter is a reproduction of Davis & Lüttge (2005) from the *American Journal of Science* (305, 727-751).

Abstract

A major challenge of biogeochemistry is to resolve the precise manner by which microbial activity influences mineral-surface reactions. Although a prerequisite for biological activity at a surface is substrate recognition and attachment, probing the nature of this biological-geological interface is inherently difficult. While atomic force microscopy (AFM) is a powerful high-resolution imaging technique capable of quantifying mineral-surface and microbial cell structure, it suffers from the invasive nature of tip-sample interactions and a limited field of view. A noninvasive imaging technique is needed that can detect the microbe at the surface and quantify any resulting changes in mineral-surface topography, while maintaining both a high spatial resolution and a large field of view. Vertical scanning interferometry (VSI) meets these requirements and enables the measurement of both local dissolution (etch pits) and global dissolution rates (surface normal retreat). Here we use AFM and VSI as complementary techniques to evaluate the influence of mineral-surface dynamics on the surface colonization of carbonate surfaces by *Shewanella oneidensis* MR-1. It was found that 1) surface colonization occurred more slowly on actively dissolving calcite surfaces than on

the less dynamic dolomite and magnesite surfaces; 2) cell attachment reduced calcite dissolution rates by more than 40% relative to cell-free controls; 3) surface microtopographical features such as etch pits provide high-energy sites that favor microbial attachment. These results indicate the existence of a complex relationship between microbial surface colonization and mineral-surface dynamics that deserves additional study. Further, this study demonstrates that VSI is an effective method for quantifying mineral-reaction rates in the context of microbial attachment. Direct comparisons with atomic force microscope (AFM) measurements also established VSI as a capable technique for making *ex situ* measurements of cell and biofilm dimensions on the surface. Accordingly, VSI should be considered a valuable complement to those powerful tools already available to the geomicrobiologist for quantification of processes occurring at the microbe-mineral interface.

3.1 Introduction

3.1.1 Importance of Microbial Attachment in Biogeochemical and Engineered Systems

While microorganisms are routinely maintained and studied in the laboratory as liquid cultures, it is well-established that the majority of bacteria in natural and engineered systems exist attached to surfaces (Korber and others, 1995; Fletcher, 1996; Mills & Powelson, 1996; Fortin and others, 1997; Little and others, 1997; Fletcher & Murphy, 2001). From the initial stages of surface colonization through the development of mature biofilms and microbial mats, the presence of microbes on surfaces has

profound impacts on both the organisms themselves as well as the substratum. Attached bacteria reside and multiply within microenvironments that confer added survival benefits to the biota while producing specialized conditions that affect industrial and biogeochemical processes at the substrate interface. Often the simple presence of biofilms on engineered surfaces interrupts critical industrial processes. This biofouling causes such disparate problems as reduced heat transfer on heat exchangers, increased fluid frictional resistance on pipelines and ship hulls, and infections on implant surfaces (Characklis, 1990; Flemming & Schaule, 1996; Geesey & Bryers, 2000). The ability of attached microorganisms to alter the physical and chemical environment at inorganic interfaces further disrupts engineered processes by degrading the material itself. Biocorrosion or microbiologically influenced corrosion (MIC) occurs when microbes initiate, facilitate, or accelerate the corrosion reaction, enhancing the damage to the metal (Little and others, 1990; Hamilton, 1995; Videla, 1996; Wagner and others, 1996; Geesey and others, 2000). The widespread economic implications of these collective processes have driven intense interdisciplinary research in the biological, medical, materials, and engineering sciences over the past 30 years, with the goal of achieving a basic understanding of the factors that govern cell attachment and elucidating the mechanisms by which surface colonization affects reactions occurring at inorganic surfaces (Lens and others, 2003).

Over this same period, there has evolved an increasing realization in the earth sciences that many critical geochemical mineral-surface processes are mediated by microbial activity (Banfield and others, 1998, Ehrlich, 1998, Ehrlich, 1999). While microorganisms can modify mineral reaction rates by altering the chemical environment,

physical attachment to the mineral-substrate may be of the most direct consequence to surface-controlled processes. Microbes attach to mineral surfaces for a variety of reasons. First, many nutrients tend to concentrate at surfaces (ZoBell, 1943). Surface-associated bacteria are able to utilize these nutrients for growth allowing them to multiply at the solid-water interface under conditions in which they are unable to multiply in the bulk aqueous phase (Marshall, 1996). Secondly, some minerals themselves serve as energy sources for microbial metabolism. The best-known example of this is the coupling of organic carbon oxidation to the dissimilatory reduction of Fe and Mn (Lovely & Phillips, 1988, Nealson & Myers, 1992). Microbial attachment to metal oxide surfaces is often requisite for taking advantage of this metabolic pathway (Arnold and others, 1988, DiChristina & Delong, 1994), although extracellular electron shuttle compounds, such as humics (Lovley and others, 1996, Lovley & Blunt-Harris, 1999) and quinones (Newman & Kolter, 2000, Rosso and others, 2003), also play a role. Additionally, microbes colonize surfaces as a general response to a range of environmental stresses where surface attachment offers protection and the opportunity for synergistic relationships with other cells (Dawson and others, 1981; Kjelleberg & Hermansson, 1984). Whatever the primary cause of microbial attachment, surface colonization generally results in degradation of the mineral surface and a considerable increase in the total reactive surface area. During this process, microbes produce acids, bases, and ligands that interact with the mineral surface, promoting mineral dissolution and the formation of secondary mineral phases (Bennett and others, 1996; Barker and others, 1997; Ehrlich, 1998). Where conditions in the natural environment favor microbial

surface colonization, microbial processes can be expected to influence observed mineral dissolution rates.

3.1.2 Critical Questions that Require Further Study

Resolving the role of microbial surface colonization in mediating mineral dissolution rates is requisite for understanding the reactivities of biogeochemically-significant materials. However, basic gaps in our understanding of the mechanisms by which microorganisms mediate the evolution of natural surfaces have slowed the establishment of quantitative models describing mineral weathering rates in the context of microbial attachment. Some key questions that have yet to be answered in a comprehensive manner are:

1. How do the properties of the mineral surface influence bacterial attachment? In other words, what are the surface-structural controls on bacterial attachment?

The majority of experimental work has been carried out to discern the environmental and metabolic conditions that favor microbial attachment to various substrates (Grasso and others, 1996). However, little is known about the controls exerted by the microstructure of the surface on surface colonization. Engineering studies have correlated microbial attachment with the surface roughness of industrially significant materials (Scheuerman and others, 1998). Likewise, the degree to which environmental samples are etched has been shown to affect bacterial colonization (Bennett & Hiebert, 1992; Hiebert & Bennett, 1992; Bennett and others, 1996). However, microbial interactions with specific topographic features, especially submicron features, remain

largely unresolved. While atomic force microscopy (AFM) has been used with considerable success to measure forces between bacteria and various substrates (Lower and others, 2000; Lower and others, 2001a; b), this technique has only recently been applied to discern attachment forces between bacteria and certain topographic features (Boyd and others, 2002). It is critical that such studies begin to yield a mechanistic understanding of the interaction between microbes and microtopography, so that the precise role that surface microstructure plays in directing bacterial colonization may be resolved.

2. What is the mechanism by which bacterial attachment modifies mineral dissolution rates? What are the consequences of bacterial attachment on the microtopographic features known to control abiotic dissolution rates?

Just as important as understanding microtopographical controls on surface colonization, is determining the manner by which microbial attachment, in turn, modifies the structure and development of the surface. This is especially significant given the known dependence of surface-controlled mineral reaction rates on the microstructure of the surface. Numerous AFM studies have demonstrated the dependence of layer-by-layer growth or dissolution on the formation of growth spirals and etch pits at surface defects (Gratz and others, 1993; Liang and others, 1996; Jordan and Rammensee, 1998; Pina and others, 1998; Teng and others, 1998; Davis and others, 2000; Higgins and others, 2000; Teng and others, 2000; Risthaus and others, 2001; Davis and others, 2004). The more recent use of vertical scanning interferometry (VSI) has successfully correlated observations of etch pit formation with surface normal retreat and global dissolution rates (Arvidson and others, 2003; Arvidson and others, 2004; Lüttge and others, 1999). A

conceptual model for mineral dissolution has been inferred from these interferometric measurements of surface topography (Lasaga & Lüttge, 2001; Lasaga & Lüttge, 2003). The resultant comprehensive dissolution rate theory successfully integrates individual surface reactions into an overall rate. These studies provide a conceptual abiotic framework by which the biological influence on mineral-dissolution rates may be compared.

3. How does the dynamic nature of the actively dissolving mineral surface affect bacterial attachment. For instance, can the dissolving surface retreat beneath the attached bacteria, thereby enhancing the probability of detachment? Additionally, what is the relationship between mineral solubility and the role of microbial surface colonization in weathering reactions?

To date, most investigations have studied microbial attachment to either inert surfaces or slowly dissolving surfaces. The precise role of mineral solubility, and hence dissolution rate, in determining the extent and rate of microbial surface colonization is largely unknown.

3.1.3 Quantifying Microbe-Mineral Interactions – A Challenge

Determining experimental answers to these questions has been slowed by difficulties inherent to measuring processes occurring at the microbe-mineral interface. Probing the nature of microbe-surface interactions in a quantifiable manner has principally been achieved through the use of atomic force microscopy (AFM). The

power of this method lies in its ability to image live cells *in situ* and its exquisite spatial resolution of changes in microtopography as well as of microbial cell structure.

However, this technique suffers from the invasive nature of tip-sample interactions and its limited field of view. For instance, direct measurement of global surface dissolution rates is largely unattainable using AFM. A complementary noninvasive imaging technique is needed that can both detect the microbe at the surface and quantify any resulting changes in mineral-surface topography, while maintaining both a high spatial resolution and a large field of view. Vertical scanning interferometry (VSI) meets these requirements and enables the measurement of both local dissolution (etch pits) and global dissolution rates (surface normal retreat) (Lüttge and others, 1999; 2003).

3.2 Vertical Scanning Interferometry (VSI)

Interferometry is an optical technique that is commonly used to measure surface topography with very high precision. Interferometers produce surface height maps by splitting a beam of light exiting a single source into two separate beams. One beam is reflected from the sample surface while the other is reflected from a reference mirror. When the two beams are recombined, interference phenomena produce an interferogram consisting of fringes that reflect the topography of the sample surface. Modern interferometers use a charge coupled device (CCD) detector to register and feed the

interferogram to a computer where phase-mapping programs produce a topographic image of the surface.

Vertical scanning interferometry (VSI) is a type of interferometry that is optimized for the wide dynamic range needed to image rough surfaces. It typically uses a white light illumination source, which allows for large vertical scans (up to 100 μm with better than 2 nm resolution). Since the coherence length is short due to the wide spectral bandwidth of the white-light source, good contrast fringes are only obtained when the two path lengths of the interferometer are closely matched in length. Therefore, the interferometer is aligned so that the interference intensity distribution along the vertical scanning direction has its peak (best contrast fringes) at the best focus position. While many algorithms are employed to analyze white light interferograms, all of them generally detect the coherence peak.

Although VSI is primarily used for non-destructive testing of semiconductors, it has also been used with considerable success to measure mineral-surface kinetics (Lüttge and others, 1999; 2003; Arvidson and others, 2003; Arvidson and others, 2004). This success stems from the speed, precision and versatility by which VSI produces quantitative topographic maps of the mineral surface. Images made at 50x magnification using white-light illumination provide a lateral resolution of $\sim 0.5 \mu\text{m}$, while maintaining a vertical resolution on the order of 1-2 nm. The scan size at this magnification is 165 x 125 μm , a little larger than the maximum AFM scan size of 130 x 130 μm . However, interference objectives can be easily switched via a turret providing, for instance, 10x magnification with a field of view of 845 x 630 μm . When larger scan areas are needed, a “stitching” procedure can be employed in which a number of overlapping

measurements are combined into one surface profile using an automated positioning stage and sub-pixel registration techniques. VSI employs a 2 $\mu\text{m/s}$ vertical scan rate allowing for extremely fast data acquisition. For instance, a surface area of 1 mm^2 with 20 μm of surface relief can be quantified in less than ten seconds.

Since interferometry measures relative surface height, absolute changes in mineral-surface topography must be measured relative to a reference surface. This is achieved by placing an inert mask on the surface. By measuring the average height difference between the reacted and unreacted surfaces, an absolute value of surface normal retreat may be determined. Thus, during dissolution, changes in average height $\Delta\bar{h}$ made at time intervals Δt yields a surface normal retreat velocity, $v_{[hkl]}$:

$$\frac{\Delta\bar{h}}{\Delta t} = v_{[hkl]}$$

Dividing this velocity by the molar volume \bar{V} (cm^3/mol) gives a global dissolution rate in the familiar units of moles per unit area per unit time:

$$r = v_{[hkl]} \bar{V}^{-1}.$$

This approach allows a simple and straightforward calculation of surface-area retreat or advance rates from measurements of average surface heights ($\Delta\bar{h}$) (Lüttge and others, 1999). In addition to these global dissolution rates, local dissolution rates at etch pits can be quantified by monitoring changes in the volume and density of etch pits across the surface over time.

The key to achieving accurate measurements of mineral-reaction rates using this masking technique is the large vertical scan range and field of view available using VSI. For instance, AFM can in principal be used to measure surface retreat rates relative to a

masked reference surface. However, the relatively small vertical scan range ($\sim 7 \mu\text{m}$) and lateral scan size of AFM makes it impossible to achieve accurate measurements of surface reaction rates. Even using VSI it is clear that the 10x objective provides a much more accurate measurement of surface normal retreat than is determined using the 50x objective. This is because the limited field of view provided by the 50x objective is more sensitive to influences from local dissolution features and reaction artifacts associated with the mask edge.

3.3 The Application of VSI to the Quantification of Mineral Surface Dynamics in the Context of Microbial Attachment

While VSI is becoming a standard technique for the quantification of mineral-surface reactions in inorganic systems, its application to microbial systems has not been fully evaluated. Only one previous study has attempted to use VSI to investigate microbe-mineral interactions (Lüttge & Conrad, 2004). In this work, surface colonization by *Shewanella oneidensis* MR-1 was observed to prevent the opening of etch pits on the calcite surface, despite undersaturated solution conditions. The authors hypothesized that this dissolution mechanism was dependent upon both the biomass to surface area ratio and the rate at which the etch pits opened. Unfortunately, these experiments used a high cell titer and small reaction volume, thereby precluding any possibility of large-scale calcite dissolution from occurring. Yet, this study raises an interesting question: what is the relationship between microbial surface colonization and the dynamics of the surface (i.e. dissolution rate)? If microbial attachment influences the dissolution of the surface, can surface dissolution, in turn, affect microbial attachment?

Here we further investigate the relationship between microbial surface colonization and mineral-surface dynamics by examining three key interactions:

1. The rate of cell attachment as a function of carbonate dissolution rate
2. Calcite dissolution rate in the presence of microbial cells vs. a cell-free control
3. The role of mineral-surface topography in determining cell attachment

A second goal of this paper is to further evaluate the applicability of VSI to the quantitative study of mineral-surface reactions in the context of microbial attachment. To this end, VSI measurements of cell and biofilm dimensions will be directly compared to those obtained using the more commonly used quantitative imaging technique, AFM.

3.4 Experimental Methods

3.4.1 Mineral-Surface Selection and Preparation

The carbonate mineral system (calcite, dolomite, magnesite) was selected as the ideal set of substrates for testing the dynamic relationship between microbial attachment and mineral dissolution in a laboratory setting. Calcite crystals dissolve readily in aqueous solutions while dolomite and magnesite surfaces are relatively inert over the short experimental durations employed in this paper. However, these three minerals present similar crystal chemistries to the cells in solution and are not part of any known microbial respiratory pathway. Cleavage surfaces of calcite, magnesite and dolomite were prepared using a razor blade and mounted on glass coverslips using sealing wax. The glass coverslips were in turn mounted on stainless steel coupons similar to those

commonly used for AFM analysis. The purpose of the glass coverslip was to minimize metal exposure to the test solutions during the course of the experiments. Additional dolomite and barite (001) cleavage surfaces were prepared and mounted in a similar fashion to be used in pre-etching experiments. Here, barite was chosen for its tendency to form elongated polygonal etch figures with a symmetry that is distinct from those that form on the dolomite surface. The dolomite surfaces were pre-etched in 1M HCl for 30 minutes, while the barite surface was etched in deionized water (DIW) for approximately ten days prior to exposure to the experimental solutions. At least two reference masks were applied to each crystal surface prior to reaction and allowed to cure for 24 hours. The masks used in this study were made using Permatex (www.permatex.com), a commercially-available high-temperature silicone gasket making compound. This type of mask has previously been used in abiotic calcite dissolution experiments where it was found to have no measureable effect on solution chemistry or observed rates (Arvidson and others, 2003, Lüttge & Conrad, 2004).

3.4.2 *Shewanella* Culture Preparation and Controls

We chose *Shewanella oneidensis* MR-1 (formerly *Shewanella putrefaciens* strain MR-1) for our attachment studies due to its propensity to form biofilms, ubiquity in the natural environment, and its use as a model microbe for bioremediation studies (Tiedje, 2002). In addition, *S. oneidensis* exhibits both motile (flagellated) and nonmotile phases,

and shares cell surface similarities with *Pseudomonas*, the focus of many adhesion studies (Bakke and others, 1990; Prince, 1996).

Shewanella oneidensis MR-1 cultures were obtained from Kenneth Nealson's lab (University of Southern California) and aerobically cultured in a pH 7.4, low-nutrient medium, prepared to 1L using: 200 mg yeast extract, 100 mg peptone, 10 mL 1M HEPES, 10 mL 0.2M bicarbonate and 20 mL 1M lactate. The culture was allowed to enter stationary phase as monitored by spectrophotometric absorbance measurements, with a final A600 reading of 0.15, corresponding to a cell titer of 3×10^8 cells/mL. Two portions of this culture were used as control solutions. The first control was a cell-free extract that was prepared through centrifugation of the culture at 9000 rpm for 30 min. The supernatant was decanted from the pellet and the centrifugation step repeated twice more. Following this procedure, the spectrophotometric absorbance A600 of the solution fell to 0. A second dead-cell control was prepared by heat-killing the cells through incubation above 45°C and below 55°C for 2.5 hours and then allowing the culture to cool and repeating the cycle two more times. The measured spectroscopic absorbance A600 of the solution fell to 0.12 during this procedure. Viability of the dead-cell control was assessed by counting the number of colony-forming units (cfu) per volume plated on Luria-Bertani (LB) agar plates. It was determined that less than 1 bacterial cell per mL of culture was microbiologically viable.

3.4.3 Reaction Conditions

Crystals were reacted in 100x15mm Petri dishes containing 50 mL of cell culture or control solution. The Petri dishes were placed on a platform shaker set to 25 rpm for the duration of the experiment. The lids of the dishes were left slightly ajar so that aerobic conditions were maintained throughout the experiment. For each experiment, multiple crystals of each species were reacted in each test solution. Further, each crystal had multiple masked regions for maximum internal controls. When comparing different mineral surfaces in the same test solution, all crystal species were placed in the same Petri dish and therefore exposed to the same experimental conditions. Due to the high number of complexation sites present on the microbe surfaces and organic species in solution, it was not possible to monitor calcium or carbonate species in solution during the course of the experiment. Following the 35 hour reaction period, the solutions were decanted from the Petri dishes containing the crystals and re-measured for pH and absorbance. The pH of the live *Shewanella* culture remained at 7.4, while the cell-free and dead-cell controls rose slightly to 7.5. The measured absorbance of the live *Shewanella* cultures fell to 0.11 during the experiment, most likely as a result of attachment to the crystals surfaces and the bottom of the Petri dish. The absorbance of the cell-free and dead-cell controls were measured to be the same as at the beginning of the experiments. The crystals were washed in a standardized fashion necessary for accurate cell density measurements. Each stainless steel coupon (containing the test crystal) was lodged vertically in a 15 mL centrifuge tube using a pair of tweezers. The

tube was gently filled with DIW, capped, rotated end-over-end and emptied. This procedure was repeated two more times for each crystal prior to imaging.

3.4.4 VSI And AFM Imaging and Measurements

A commercially-available MicroXAM MP-8 (ADE Phase-shift, Tucson, AZ) vertical scanning interferometer (VSI), equipped with 10x and 50x Nikon Mirau objectives, was used to image the crystal surfaces. The 10x interferometric objective yields a 845 x 630 μm field of view, while the 50x objective allows for scan sizes of 165x124 μm . There are two basic types of images that can be generated from data sets acquired using VSI. The standard data file is a 2-dimensional (2D) topographic image similar to height images obtained using AFM, where topographic information is conveyed according to a color scale. In these images, bright colors typically indicate higher surface features on the image. The second image type used in this study is a 3-dimensional (3D) solid-model representation of the topographic information contained in the VSI data file.

Measurements of cell densities on the carbonate surfaces were made by counting the number of cells per area in randomly selected images or portions of images. Averages of at least 20 separate counts are reported in tables 1 and 3. When available, AFM observations were found to confirm the VSI cell density measurements. Global dissolution rates were measured after 35 hours for at least two masks per mineral species and for at least two crystals for each mineral species. At least ten transects were

measured along each mask, paying careful attention to taking transects along a single continuous terrace to avoid error from natural surface steps.

A Multimode Nanoscope III AFM (Digital Instruments, Santa Barbara, CA, USA) was used to make the *ex situ* (in air) observations of mineral surfaces used in this study. This instrument was equipped with a J piezoelectric scanner with a maximum range of 130 x 130 μm . While Tapping Mode is often the preferred technique for imaging biological materials, the *Shewanella* cells were found to be attached strongly enough to the crystal surface to allow for Contact Mode imaging using minimal contact forces. It was found that this imaging technique provided the best resolution of both surface topography and attached cells.

3.5 Results and Discussion

3.5.1 Surface Colonization on Carbonate Surfaces

S. oneidensis surface colonization was monitored at time intervals using the interferometer. Each carbonate crystal was observed immediately after it had been washed using the standardized procedure described in the methods section. Time-series analyses demonstrated that the carbonate surfaces underwent continuous surface colonization during the course of the 35 hour exposure period studied (figure 3.1). The early stages of surface colonization were characterized by the formation of a honeycomb-shaped network of attached cells surrounding cell-free portions of the crystal surface

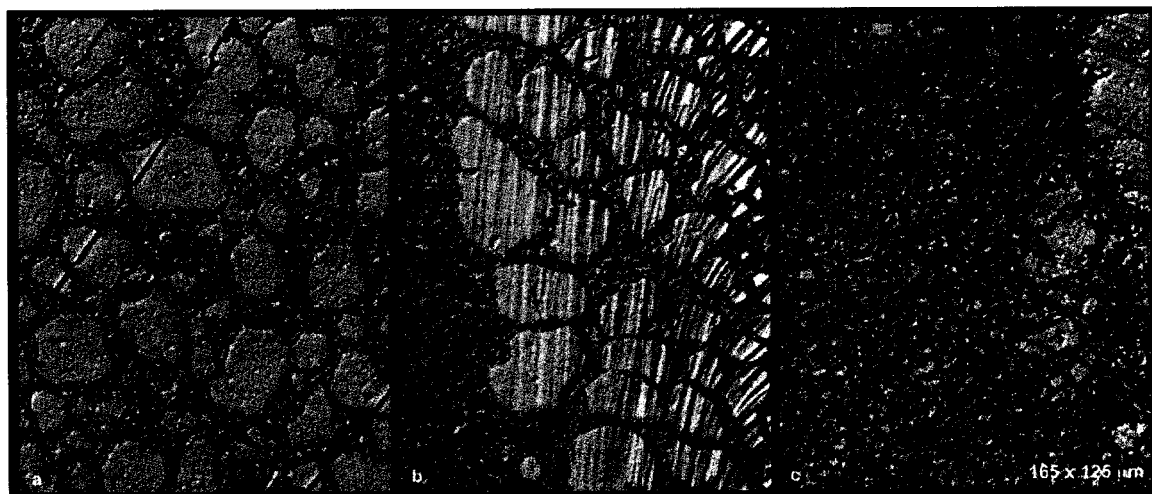


Figure 3.1

3D plots of VSI data sets showing progressive surface colonization by *Shewanella* on dolomite over 35 hours. a) honeycomb morphology after 9 hours b) beginning of monolayer surface coverage after 18 hours of exposure c) after 25 hours, most of the central regions of the crystal surface were covered by a continuous monolayer of cells. (All images were captured using a 50x interferometric objective yielding image sizes of 165 x 125 μm .)

(figure 3.1A). During this period, attached cell density was found to be highest on the interior portions of the crystals and lowest near the crystal edges. While attachment rates varied to some degree between crystals and locations on the same crystal, most of the crystal surfaces were nearly completely covered by a monolayer biofilm after the 35 hour observational period (figure 3.1C). It was apparent from the topographic images acquired using VSI that the attached cells were surrounded by organic material, possibly a conditioning film or the result of early extracellular polysaccharide (EPS) production (figure 3.2). The physical dimensions of this associated organic material as well as of the cells themselves could be directly determined from the VSI images (figure 3.3). The cells were found to range from 2 to 3 microns in length and from 400 to 650 nm in diameter. The associated organic material was consistently measured to rise 200 to 250 nm above the surface of the crystal. It was found that much of the organic material associated with the attached cells could be removed if the crystal surfaces were exposed to a direct stream of DIW from a wash bottle soon after removal from the bacterial cultures. Subsequent VSI imaging revealed clearly visible entrenched cells arranged in the same patterns as previously observed, but less obscured by associated organic material (figures 3.4 and 3.5). However, this washing step also caused some of the attached cells on the surface to lyse, as was evidenced by measured cell dimensions (cell diameters on the order of 100 nm) that were significantly smaller than undamaged cells.

In general, cells were found to attach to the carbonate substrates in essentially a random orientation. The lack of preferred alignment on the surface provided no evidence that mineral-surface microtopography played a definitive role in *Shewanella* surface colonization. However, as figure 3.6 demonstrates, some cells were observed to align



Figure 3.2

2D VSI image of *Shewanella* surface colonization on a magnesite surface after 9 hours. This early biofilm consists of taller (bright-yellow) cells and associated lower (dark yellow) organic material.

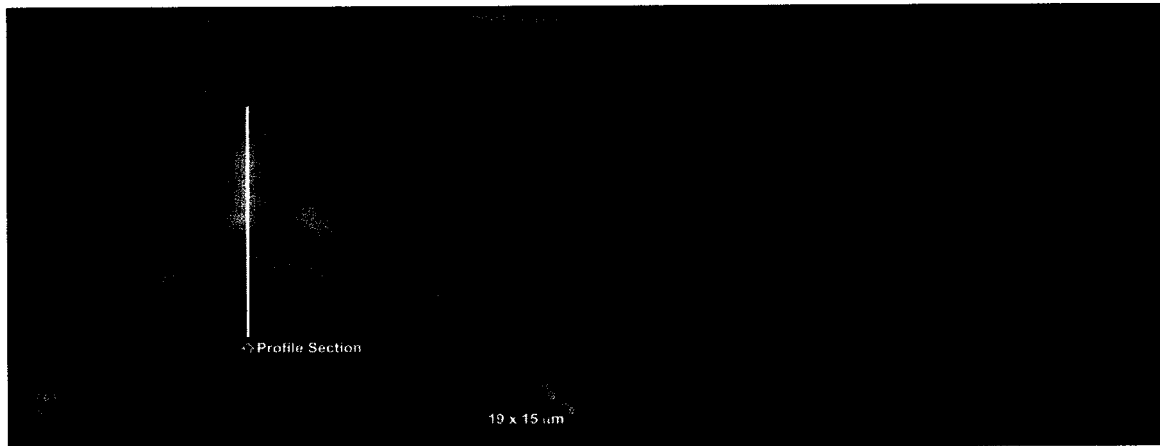


Figure 3.3

Cross-section measurements of a single *Shewanella* cell on a dolomite surface and its associated organic material. Here, the cell is 650 nm in diameter, 3 microns long, and the associated organic material rises 200 nm above the crystal surface.

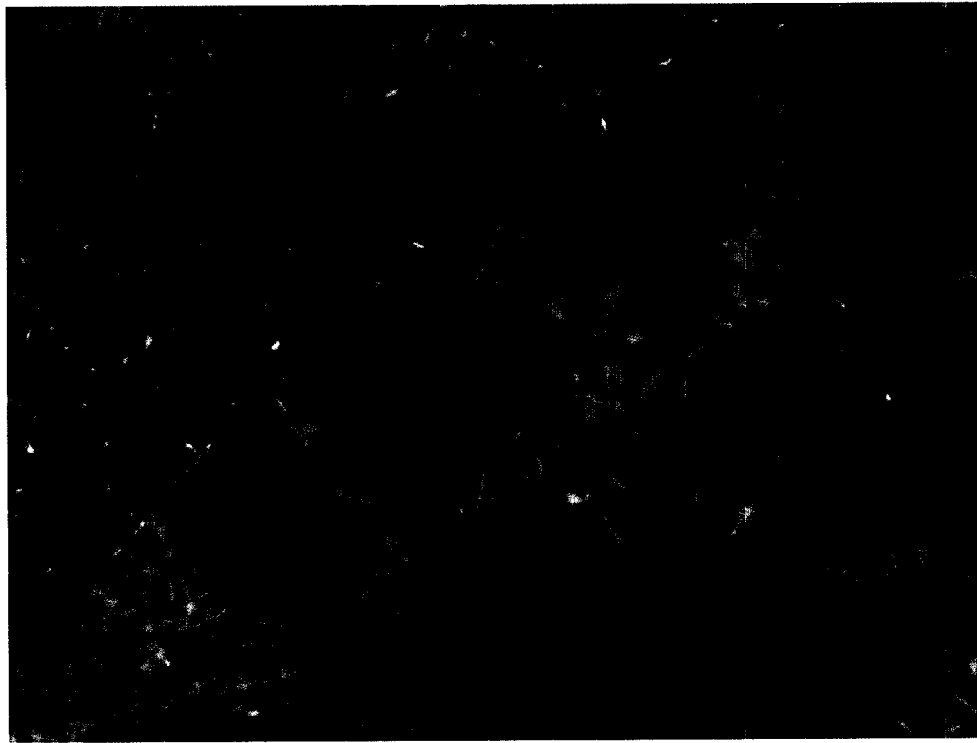


Figure 3.4

2D VSI image of entrained cells on calcite following the removal of associated organic material. (9 hours exposure to *Shewanella* culture.)

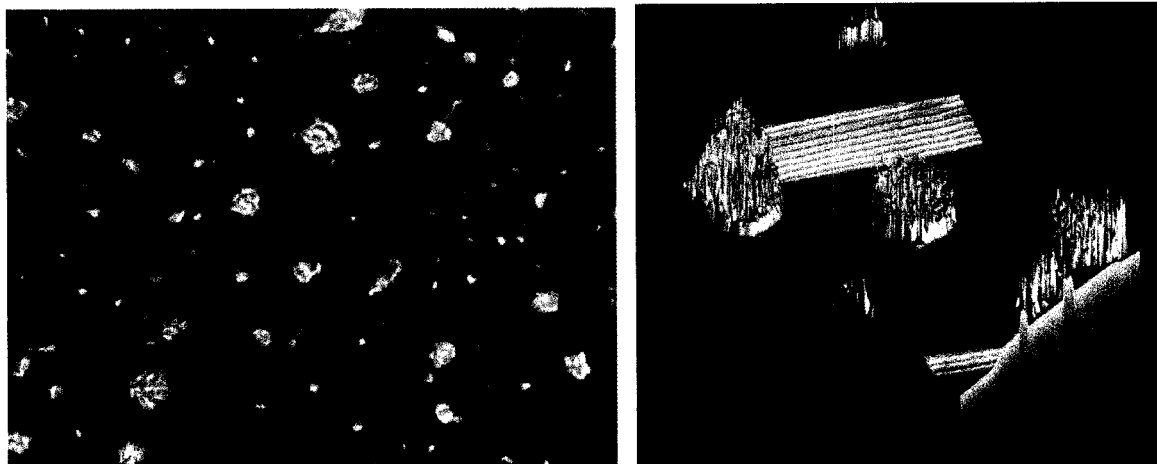


Figure 3.5

The removal of associated organic material revealed the clear presence of *Shewanella* microcolonies on the calcite surface. The initial stages of surface colonization were often characterized by microcolony formation. a) 2D VSI image b) 3D reconstruction of microcolonies in the context of natural surface topography. (8 hours of exposure to *Shewanella* cultures.)

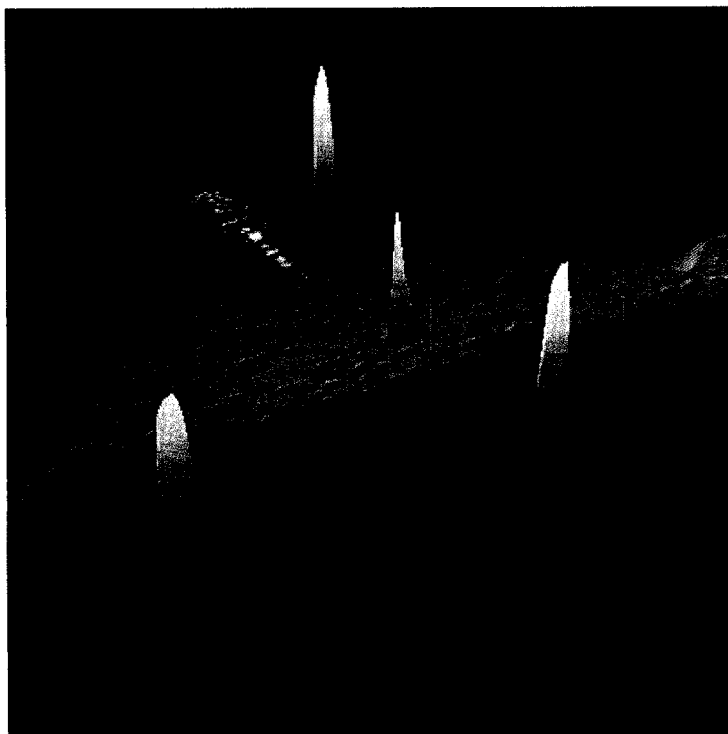


Figure 3.6

The role of mineral-surface microtopography in determining cell attachment on calcite. This image is a 3D representation of a VSI data set that was generated using the SPIP 3.0 software package (www.imagemet.com). The bright-yellow peaks are bacterial cells. Two cells are attached lengthwise along a macrostep; one cell is attached to the center of an etch pit; one cell is attached to a flat terrace. The etch pits are between 75 and 142 nm deep. The macrostep is 230 nm tall. The microbe in the center of the etch pit is 560 nm tall and 3.5 microns in length. The microbe attached to the surface is 325 nm tall and 2.0 microns in length. The two cells attached lengthwise to the step are between 475 and 525 nm in height and 2.0 to 2.75 microns in length. This image indicates that while cell alignment may occur along energetically favorable attachment sites, the availability of such sites did not limit surface colonization. The image is 30x30 μm .

along suitable topographic features. Nonetheless, it must be concluded that under the experimental conditions studied, *Shewanella* surface colonization was not limited by the availability of energetically favorable attachment sites.

3.5.2 Comparison of VSI and AFM Imaging Techniques and Measurements

Many of the same crystal surfaces that had been exposed to the *Shewanella* cultures were imaged on the AFM immediately after analysis on the interferometer. While Tapping Mode (Acoustic AC Mode) AFM can be used for *in situ* imaging of biological materials, *ex situ* (in air) Contact Mode imaging was found to yield the best resolution of both attached cells and underlying crystal microtopography. Additionally, these imaging conditions were most similar to those employed using VSI, making possible direct comparisons between AFM and VSI measurements. For imaging ease, only those crystal surfaces that had most of the associated organic material washed away were imaged on the AFM.

While bacterial cell dimensions are near the lateral resolution limits of the 50X interferometric objective used in VSI, higher-resolution AFM imaging provided concise images of microbes at the mineral-surface (figures 3.7 and 3.8A). In fact cell structures such as flagella are easily resolved using AFM (figure 3.8B). However, despite the resolution difference between the two techniques, VSI measurements of cell diameter and length (figure 3.9) were found to be very comparable to those measured using AFM. This is an interesting result given that the lower resolution of VSI causes the shape

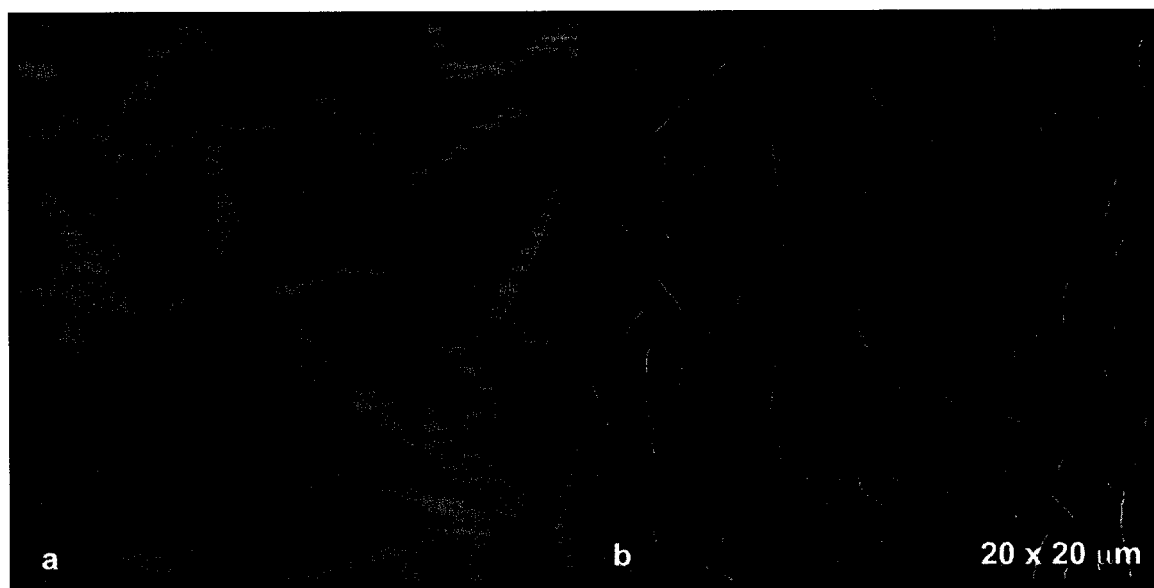


Figure 3.7

AFM images of *Shewanella* surface colonization on a dolomite surface after 35 hours. a) height image b) deflection (amplitude) plot.

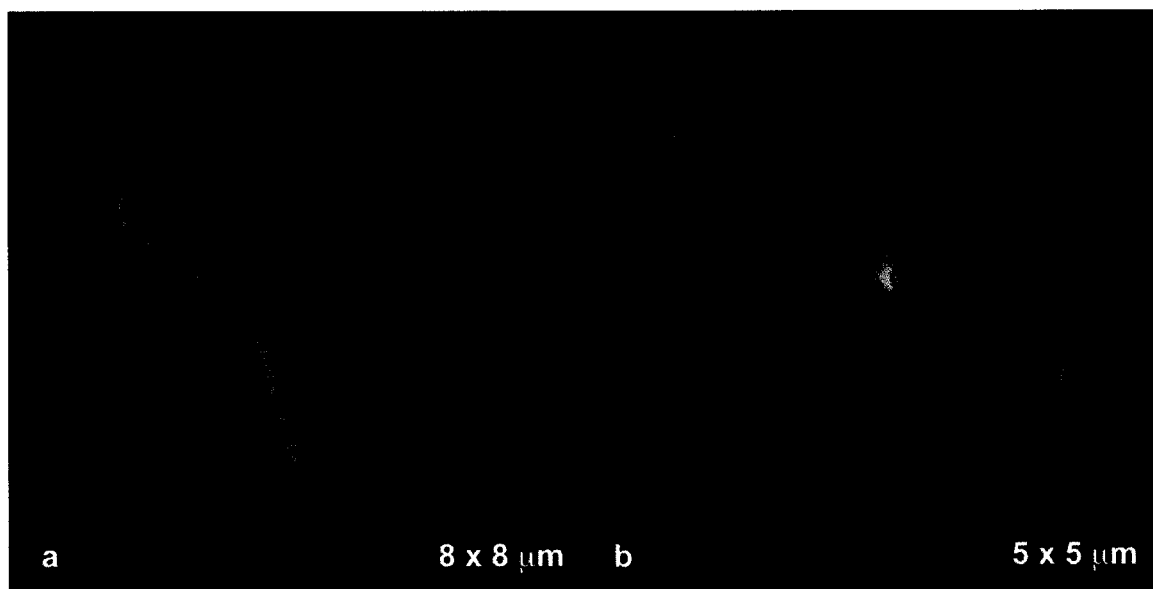


Figure 3.8

High-resolution deflection AFM images of *Shewanella* cells on a dolomite surface. a) a recently divided cell b) a rare example of a flagellum that is still attached to a *Shewanella* cell.

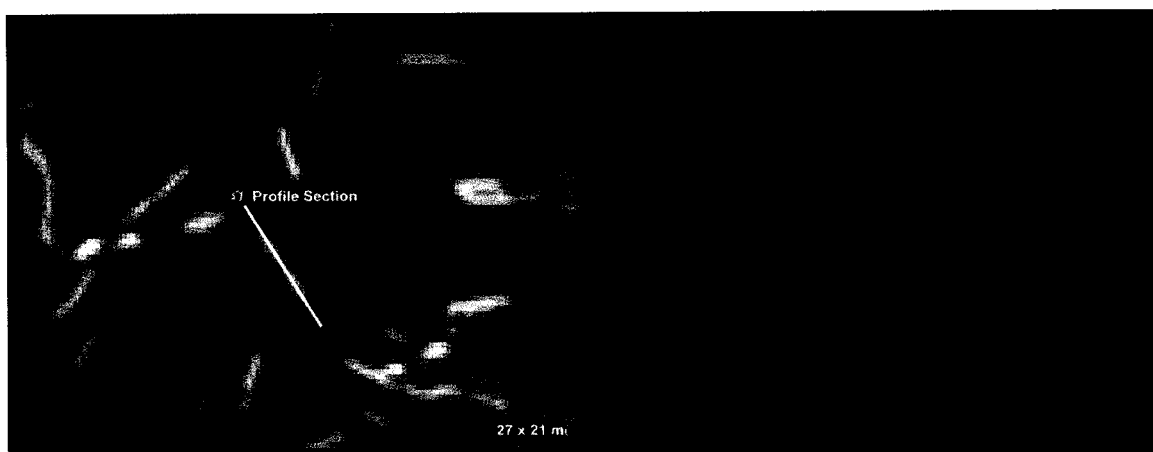


Figure 3.9

Cross-section of a recently divided cell on a calcite surface. The individual cells measure 400 and 440 nm in diameter and 2.5 microns in length. VSI measurements such as these can yield accurate measurements of cell dimensions that compare favorably with those obtained using more common *ex situ* AFM techniques.

outline of the cells to appear somewhat diffuse. Fortunately, the optical nature of VSI that is responsible for such limitations in lateral resolution also confers certain advantages to VSI over AFM. The noninvasive nature of VSI imaging does not suffer from the tip-sample interactions inherent to AFM imaging that can cause bacterial cells to dislodge from the surface during imaging. Further, the large field of view and fast data acquisition allows VSI to quickly assess attached cell density over the entire crystal surface. Although not studied here, the large vertical scan range characteristic of VSI may even allow for the quantification of developing biofilm structures up to 100 μm above the surface. These capabilities make VSI a strong complement to the *in situ* high-resolution imaging abilities of AFM. The coupling of these two techniques allows for mineral-surface reactions and cell-mineral interface processes to be quantified at multiple length-scales.

3.5.3 Role of Mineral-Surface Dynamics in Surface Colonization

As expected, the solubility differences between the carbonate minerals used in this study resulted in significantly different dissolution rates as monitored by VSI. Etch pits were visible on the calcite surfaces within ten minutes of reaction with either the cell-free control solutions or the *Shewanella* cultures. In contrast, no dissolution was observed on the dolomite or magnesite surfaces during the 35 hour experiment. This difference in reactivity was most notable when comparing masked and unmasked regions of the crystal surfaces (figures 3.10 and 3.11). Accordingly, the use of these different carbonate surfaces offered the opportunity to examine the

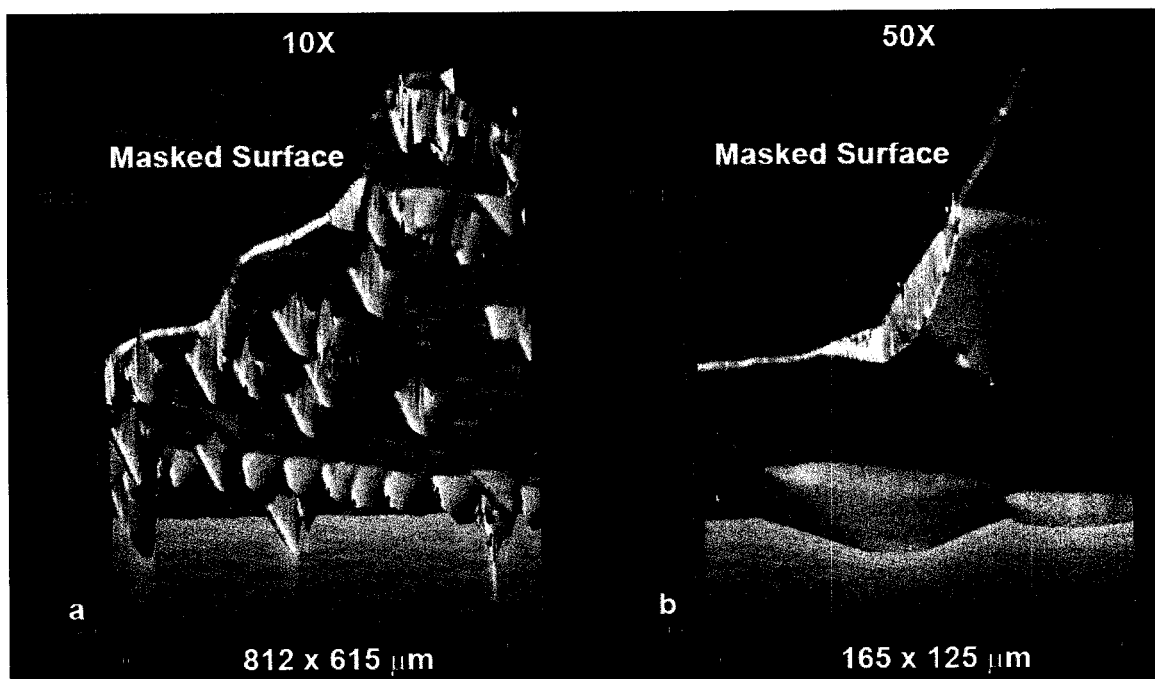


Figure 3.10

Images showing the extent of dissolution between masked and unmasked areas of a calcite crystal following 4 hours of reaction in the cell-free control solutions. Both images show portions of the same masked area with the only difference being the magnification of the interferometric objective used. The previously masked portion of the calcite surface is apparent as the smooth (unetched) surface in the upper-left quadrant of the image.

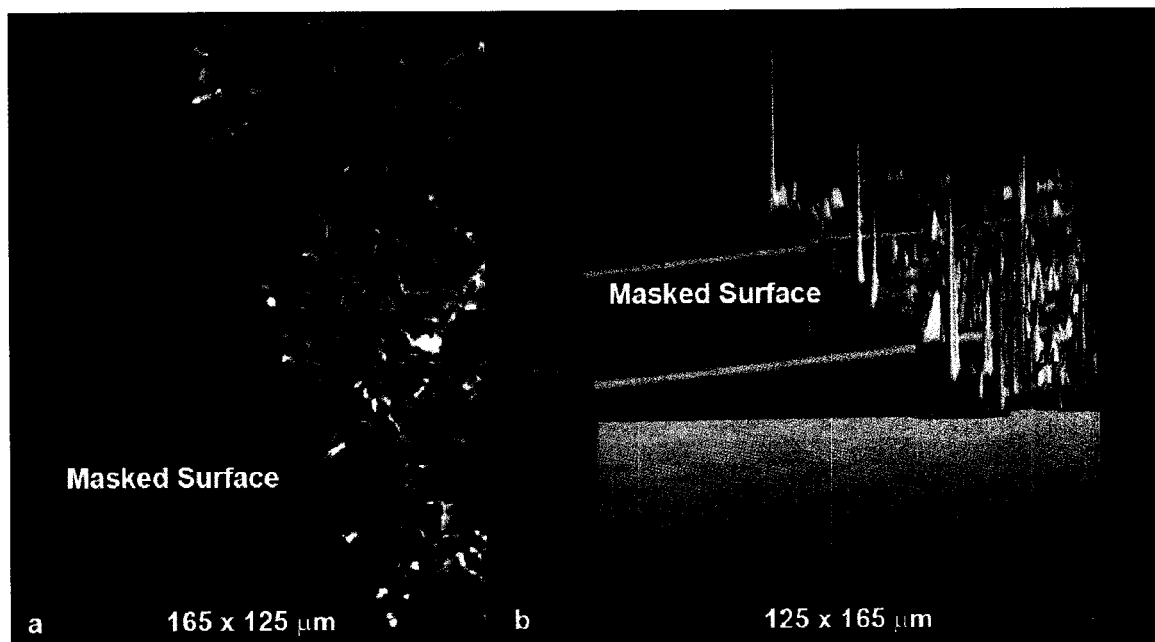


Figure 3.11

Images showing the masked and unmasked regions of a dolomite crystal surface following 4 hours of exposure to *Shewanella* cells. These VSI images reveal that no dolomite dissolution occurred during the reaction period. Instead, a number of *Shewanella* cells have deposited on the surface along with a thin organic film. The unreacted surface (previously masked) is apparent as the smooth surface on the left side of these images.

role of mineral-surface dynamics in microbial surface colonization while still presenting relatively similar surface chemistries and crystal structures to the attaching cells.

Surface colonization rates on the various carbonate surfaces were determined by simply counting the numbers of attached cells per unit area on the crystal surfaces after 8 and 35 hours of exposure to the *Shewanella* cultures. The results of these surface cell density measurements are given in table 1 and representative images are shown in figure 3.12. At both the 8 and 35 hour time points, the attached cell density on the calcite surfaces was found to be approximately half of those measured on the dolomite and magnesite surfaces. This finding indicates that cell attachment occurred more slowly on actively dissolving calcite surfaces than on the less dynamic dolomite and magnesite surfaces. Further, after the 35 hour experiments, it was clear that the majority of visible cells on the calcite surfaces were attached to the rims of large etch pits (figure 3.13). This observation may further indicate that conditions for microbial attachment are less favorable near the centers of dissolution where the surface is most dynamic.

3.5.4 Role of Surface Colonization in Determining Calcite Dissolution Rate

Calcite dissolution rates were measured in the context of microbial attachment by comparing masked portions of the crystal surface to those regions exposed to the experimental test solutions (figure 3.14). Table 3.2 contains the measured surface normal retreats and corresponding dissolution rates for calcite surfaces exposed to both the cell-free control and *Shewanella* cultures for 35 hours. These measurements indicate that calcite dissolution in the presence of live *Shewanella* cells was almost 40% slower than the dissolution rate observed for the cell-free control solutions. This difference in reaction is easily visualized by comparing the masked surfaces to the reacted surfaces in the 3D models shown in figure 3.14. Insight into the

Table 3.1 – Average Measured Attached Cell Densities (Cells/100 μm^2)

	Calcite	Dolomite	Magnesite
8 Hours	2.11	4.26	3.45
35 Hours	3.12	6.24	9.89

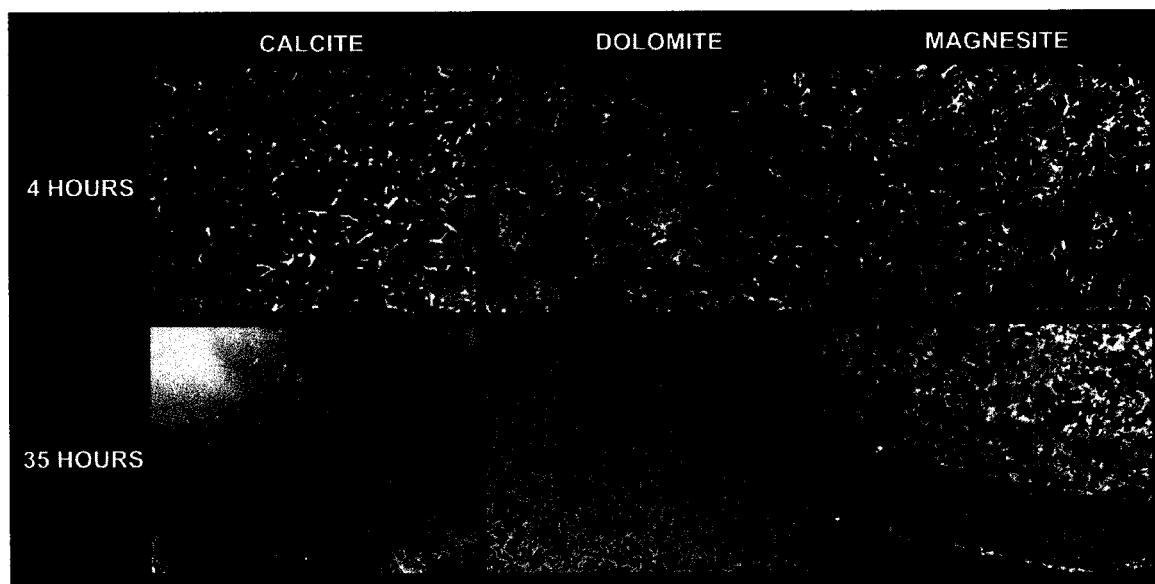


Figure 3.12

VSI images showing differences in *Shewanella* surface colonization on calcite, dolomite and magnesite surfaces after 8 and 35 hours of exposure to microbial cultures. Average measured cell densities for the respective crystal surfaces are given in table 1. Here, only images that have had most of the associated organic material removed are shown. Counts were primarily conducted on crystal surfaces that had only undergone the initial standardized washing procedure, although no statistical difference in cell density measurements was observed following the second washing procedure. (All images are 125 x 165 μm .)



Figure 3.13

VSI image of *Shewanella* surface colonization on the calcite surface after 35 hours. The majority of cells were found to occupy the rims of large etch pits, indicating that microbial attachment may be less favorable near dissolution centers where the surface is most dynamic.

Table 3.2 - Calcite Dissolution Measurements After 35 Hours

	Surface Normal Retreat (μm)	Global Dissolution Rate ($\text{mol}\cdot\text{cm}^{-2}\cdot\text{s}^{-1}$)
Cell-Free Control	2.83	6.1×10^{-11}
Heat-Killed Cells	2.71	5.8×10^{-11}
<i>Shewanella</i> Culture	1.64	3.5×10^{-11}

Global dissolution rates were calculated using a calcite molar volume of $36.93\text{ cm}^3/\text{mol}$.

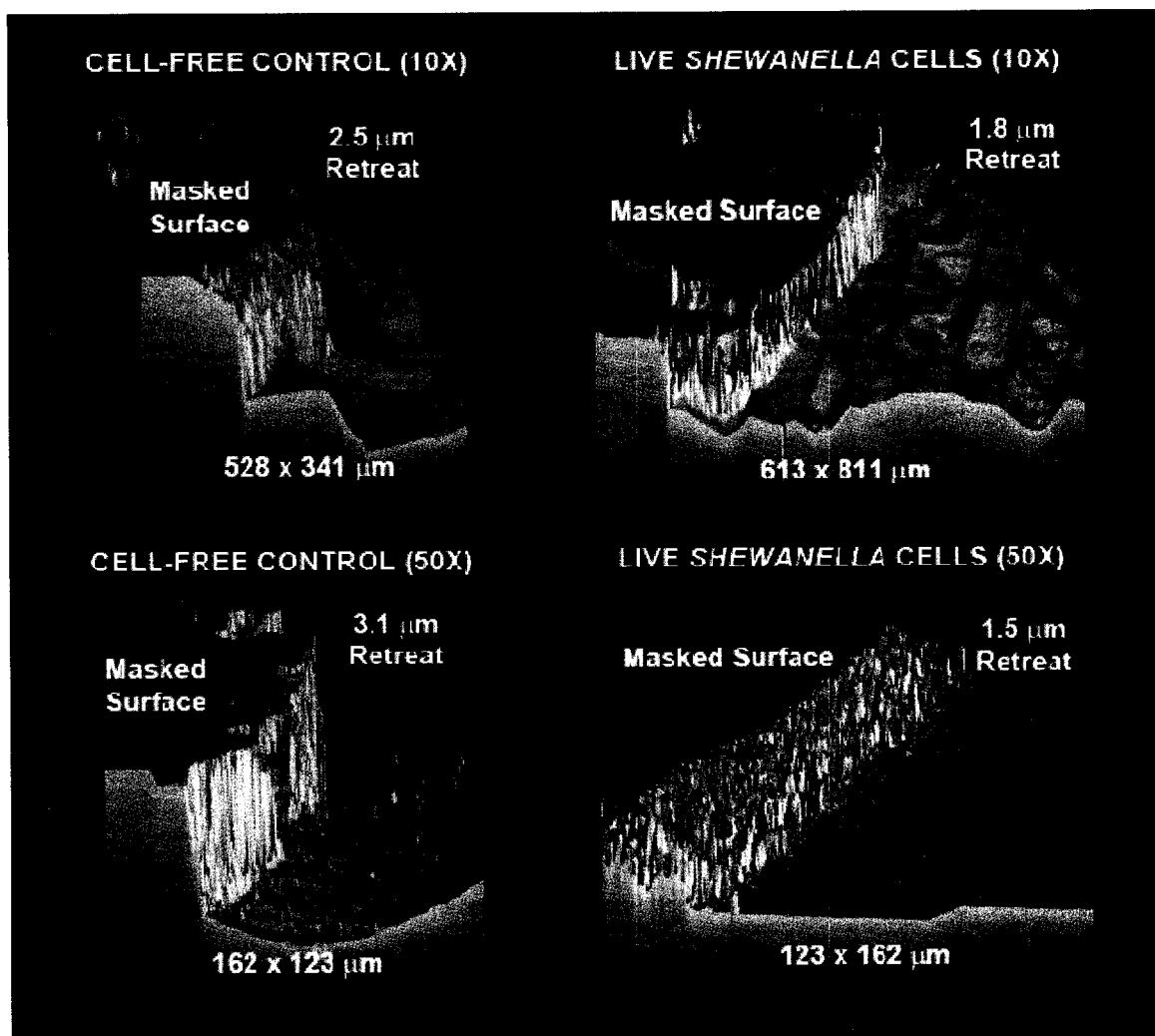


Figure 3.14

VSI data of calcite dissolution relative to masked portions of the crystal surface after 35 hours of exposure to cell-free controls and *Shewanella* cell cultures. 10X and 50X images of the same masked region are shown for comparison. Average measurements of calcite dissolution for the two systems are given in table 2. Here the unreacted portions of the surface occupy the left side of the images.

mechanism by which the *Shewanella* cultures retarded calcite dissolution may be gained by looking at the results for the heat-killed *Shewanella* control solutions given in table 3.2. The measured calcite dissolution rate in solutions containing heat-killed *Shewanella* cells was similar to the rate measured for the cell-free control. Since the heat-killed cells were not found to attach to the surface, it seems that the measured inhibition of calcite dissolution in the presence of live *Shewanella* cells resulted from the physical attachment of cells to the surface. This attachment may have slowed calcite dissolution by interfering with the development of etch pits on the crystal surface, as has been previously described by Lüttge and Conrad (2004).

3.5.5 Role of Mineral-Surface Topography in Determining Surface Colonization

The role of mineral-surface microtopography in determining cell attachment was tested by exposing pre-etched dolomite and barite crystals to *Shewanella* cultures and comparing the measured surface cell densities to those of pristine cleavage surfaces exposed to the same solutions. Dolomite and barite surfaces were chosen due to their slow dissolution kinetics relative to the studied exposure times, so that the effect of mineral-surface microtopography on cell attachment could be isolated. It was immediately obvious after short exposure periods that attached cell densities were much greater on the pre-etched surfaces than the pristine cleavage surfaces (figure 3.15). Table 3.3 gives average measurements of cell density for several crystals and indicates that pre-etching resulted in a 2.5 to 5-fold increase in cell attachment during the 4 hour exposure period. While it appears from VSI imaging alone that cell attachment is uniform across the pre-etched surfaces while etch pit density is not, higher resolution AFM images (figure 3.16) of dolomite and barite surfaces revealed the presence of additional dissolution features including smaller etch pits that were below the lateral resolution limits of VSI. These

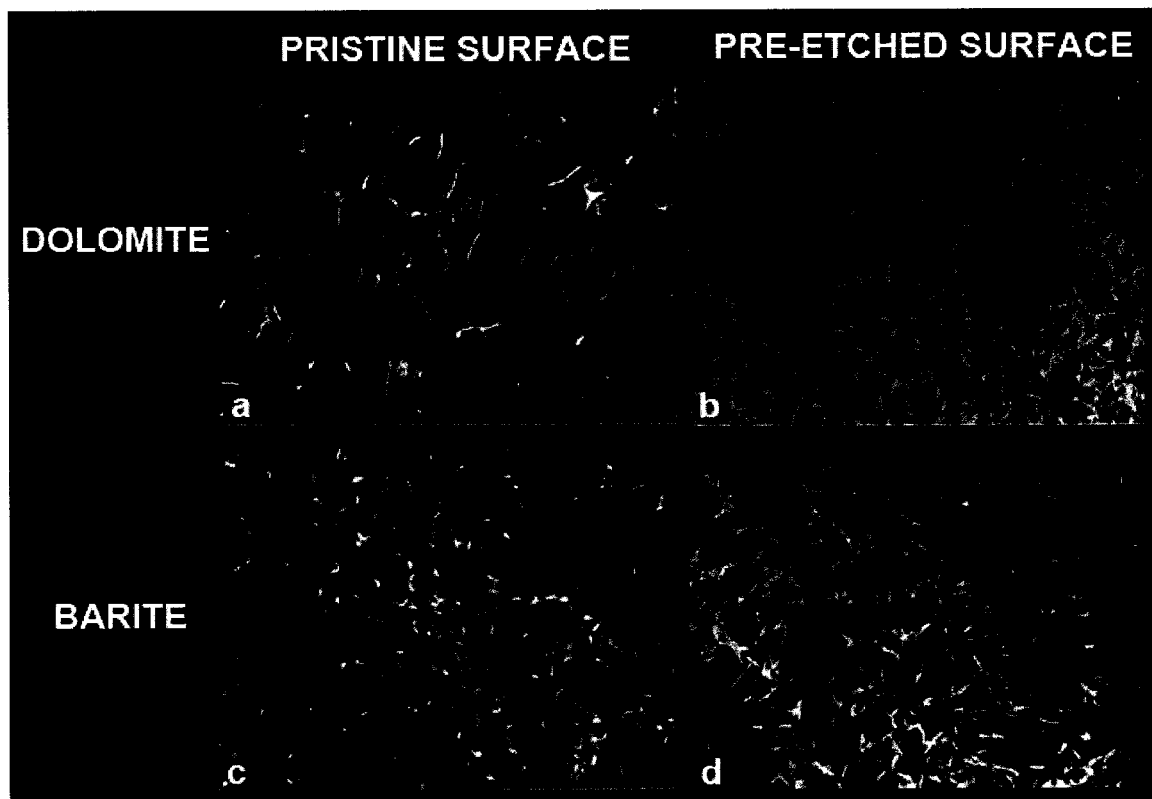


Figure 3.15

VSI images of surface colonization on barite and dolomite surfaces after 4 hours. Attached cell density was significantly higher on the pre-etched surfaces than on the pristine cleavages surfaces. Average measurements of attached cell densities are given in table 3. (All images are 125x165 μm).

Table 3.3 – Measured Attached Cell Densities on Pristine and Pre-Etched Surfaces after 4 Hours (Cells/100 μm^2)

	Dolomite	Barite
Pristine Surfaces	1.10	2.00
Pre-Etched Surfaces	5.96	5.06

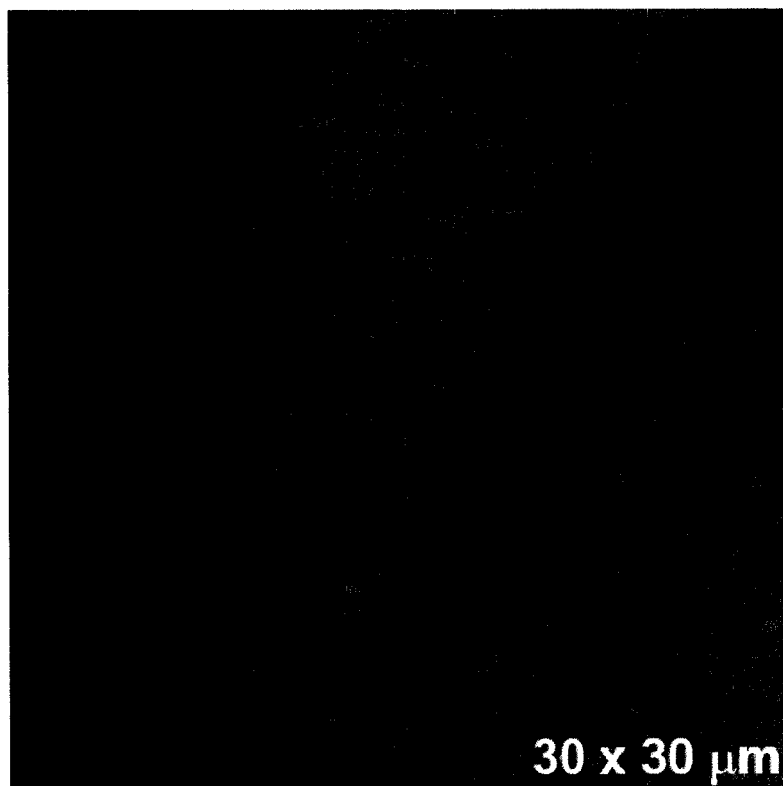


Figure 3.16

AFM image of pre-etched dolomite surface revealing extremely rough surface steps that are not observable using VSI.

microtopographical features facilitated widespread surface colonization (figure 3.17) over much shorter time periods than was required for similar microbial attachment to occur on pristine cleavage surfaces. This result contrasts sharply with observations of the actively dissolving calcite surface, where the presence of etch pits was correlated with lower attached cell density. This observational disparity provides further evidence that surface dynamics plays a definitive role in microbial attachment.

3.6 Summary and Conclusions

Vertical scanning interferometry (VSI) has previously been shown to be extremely useful for making quantitative measurements of inorganic mineral-surface reactions. Here we establish VSI as a powerful tool for quantifying surface reaction rates in the context of microbial surface colonization. Additionally, VSI was shown to be capable of accurately measuring attached cell dimensions and biofilm thicknesses relative to a masked surface. The noninvasive imaging characteristic of VSI, along with fast data acquisition, a large field of view, and large vertical scan range, makes VSI a strong complement to the *in situ* high-resolution imaging capabilities of atomic force microscopy (AFM). The combination of these two quantitative imaging techniques is well-positioned to provide the critical information needed to resolve microbe-mineral interactions across multiple length-scales. The power of these techniques would be further amplified when used in conjunction with *in situ* optical techniques, such as confocal laser scanning microscopy (CLSM), that use fluorescent probes to monitor chemical and physiological aspects of biofilms.

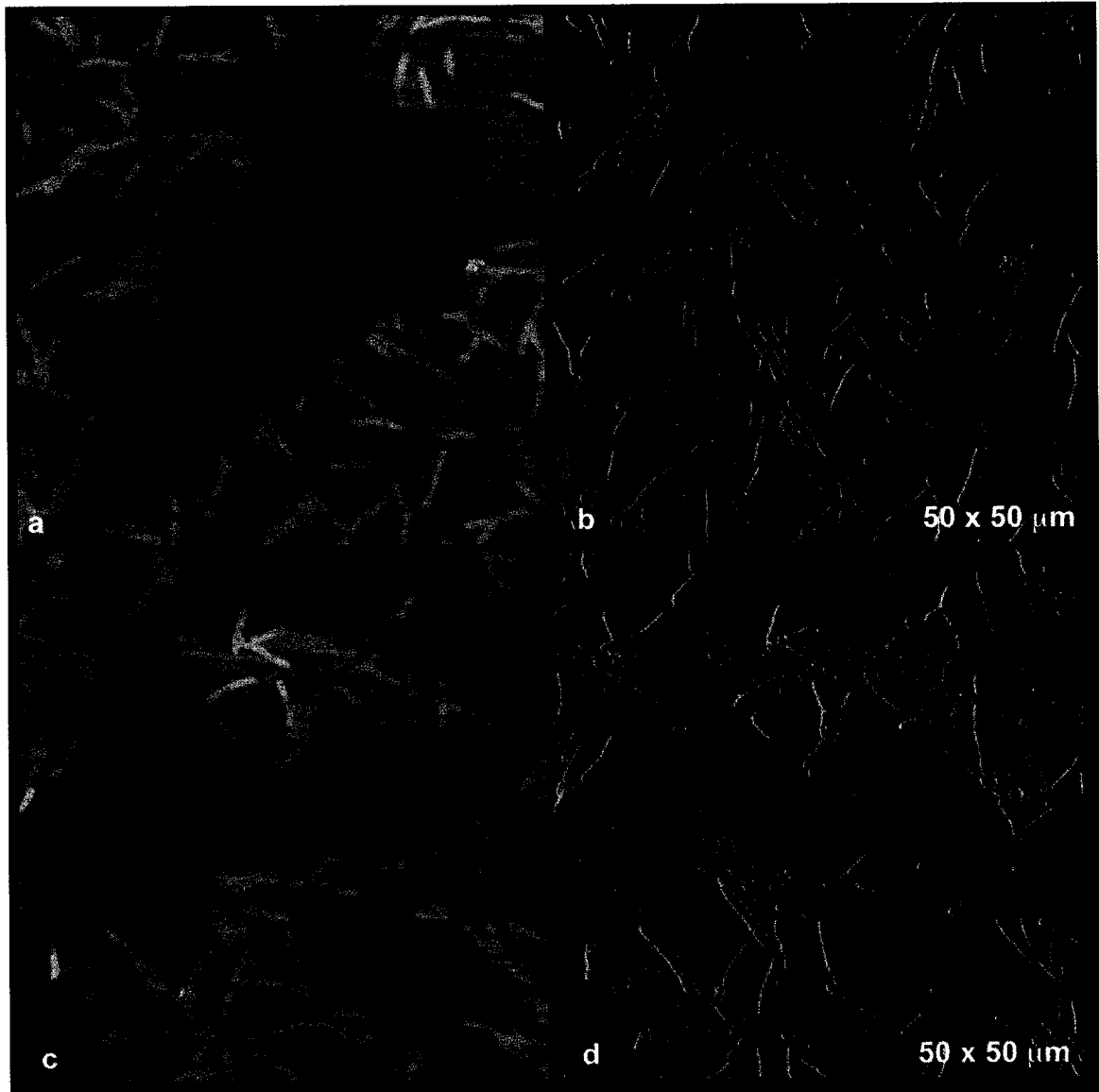


Figure 3.17

AFM images of cell attachment on pre-etched dolomite and barite surfaces. Dissolution features like those shown in figure 16 are not visible in these images because of the much greater vertical scale employed to accommodate both bacterial cells and surface features
a) height image of dolomite surface b) corresponding deflection (amplitude) plot c)
height image of barite surface d) corresponding deflection (amplitude) plot

In this study, AFM and VSI were used in synergistic fashion to achieve a beginning understanding of the interplay between mineral-surface dynamics and microbial attachment. Our results indicate that when the dissolution rate of the surface is comparable to the rate of surface colonization, surface dynamics may be a significant factor in determining cell attachment. This was found to be the case for calcite where significant surface retreat resulted in reduced *Shewanella* surface colonization. In further support of this finding, the most dynamic areas of the surface (etch pits) were found to provide additional local barriers to cell attachment. However, the cells that did attach to the calcite surface affected surface dynamics by reducing the overall far from equilibrium dissolution rate. In contrast to the findings for calcite, dissolution features on the slower-dissolving dolomite and barite surfaces actually resulted in faster surface colonization rates by providing energetically favorable sites for cell attachment. This complicated relationship between surface colonization and mineral-surface development reinforces the central theme of biogeochemistry that the evolution of geological surfaces and biological systems are intertwined. However, the significance of these relationships to biogeochemical and engineered systems requires further investigation.

CHAPTER 4. Calcite and Dolomite Dissolution Rates in the Context of Microbe-Mineral Surface Interactions

This chapter is a reproduction of Davis, Nealson and Lüttge (2007) from *Geobiology* (5, 191-205).

Abstract

Although microbes have been shown to alter the dissolution rate of carbonate minerals, a mechanistic understanding of the consequences of microbial surface colonization on carbonate dissolution has yet to be achieved. Here we report the use of vertical scanning interferometry (VSI) to study the effect of *Shewanella oneidensis* MR-1 surface colonization on the dissolution rates of calcite (CaCO_3) and dolomite ($\text{CaMg}(\text{CO}_3)_2$) through qualitative analysis of etch pit development and quantitative measurements of surface-normal dissolution rates. By quantifying and comparing the significant processes occurring at the microbe-mineral interface, the dominant mechanism of mineral dissolution during surface colonization was determined. MR-1 attachment under aerobic conditions was found to influence carbonate dissolution through two distinct mechanistic pathways: 1. inhibition of carbonate dissolution through interference with etch pit development and 2. excavation of carbonate material at the cell-mineral interface during irreversible attachment to the mineral surface. The relative importance of these two competing effects was found to vary with the solubility of the carbonate mineral studied. For the faster-dissolving calcite substrates, inhibition of dissolution by attachment and

subsequent extracellular polysaccharide (EPS) production was the dominant effect associated with MR-1 surface colonization. This interference with etch pit development resulted in a 40-70% decrease in the surface normal dissolution rate relative to cell-free controls, depending primarily upon the concentration of cells in solution. However, in the case of the slower-dissolving dolomite substrates, carbonate material displaced during the entrenchment of cells on the surface far outweighed the abiotic dissolution rate. Therefore, during the initial stages of surface colonization, dolomite dissolution rates were actually enhanced by MR-1 attachment. This study demonstrates the dynamic and competitive relationship between microbial surface colonization and mineral dissolution that may be expected to occur in natural environments.

4.1 Introduction

Carbonate minerals are principal components of biomineralizing systems and play a central role in a number of important biogeochemical cycles. The relative rates of carbonate mineral precipitation and dissolution determine the preservation and subsequent accumulation of carbonate in the geologic record as well as the sequestration of several coprecipitated trace elements. Accordingly, a thorough understanding of carbonate dissolution rates is critical to the successful modeling of the global carbon cycle and its use in predicting the fate of fossil fuel carbon dioxide. To this end, numerous laboratory studies have been conducted to determine the dissolution rates of carbonates under various conditions (for a review see Morse & Arvidson, 2002; Morse & Mackenzie, 1990; Morse, 1983).

Enhanced dissolution of carbonate minerals has been associated with the activity of microorganisms since the pioneering study of Paine et al. (1933). While this early study focused on the biodegradation of limestone building-materials, similar processes are known to occur on natural carbonates such as corals and beachrock (e.g., Ehrlich, 1996). Carbonate biodegradation in marine surface waters is particularly intriguing since these solutions are generally supersaturated with respect to carbonate minerals. Insight into this process may be found in a recent field study that observed calcite dissolution proximal to the cell-mineral interface in supersaturated groundwater solutions (Bennett et al., 2000). This study confirms that the chemistry at the microbe-mineral interface differs substantially from that of the bulk solution, producing microscale dissolution features coincident with macroscale precipitation (Bennett et al., 2000). Despite these important observations, a mechanistic understanding of the consequences of microbial surface colonization on carbonate dissolution rates remains largely unresolved.

While microorganisms can modify abiotic mineral reaction rates by altering the chemical environment, physical attachment to the mineral-substrate may be of the most direct consequence to surface-controlled processes. Microbes attach to surfaces for a variety of reasons. First, many nutrients tend to concentrate at surfaces (ZoBell, 1943). Surface-associated bacteria are able to utilize these nutrients for growth allowing them to multiply at the solid-water interface under conditions in which they are unable to multiply in the bulk aqueous phase (e.g., Marshall, 1996). Secondly, some minerals themselves, serve as energy sources or electron acceptors for microbial metabolism. The best-known example of this is the coupling of organic carbon oxidation to the dissimilatory reduction of Fe and Mn (Lovley & Phillips, 1988, Nealson & Myers, 1992). Microbial attachment to

metal oxide surfaces is generally requisite for taking advantage of this metabolic pathway (Arnold et al., 1988, DiChristina & Delong, 1994), although extracellular electron shuttle compounds, such as humics (Lovley et al., 1996; Lovley & Blunt-Harris, 1999) and quinones (Newman & Kolter, 2000; Rosso et al., 2003), may also play a role.

Additionally, microbes colonize surfaces as a general response to a range of environmental stresses where surface attachment offers protection and the opportunity for synergistic relationships with other cells (e.g., Dawson et al., 1981, Kjelleberg & Hermansson, 1984). Whatever the primary cause of microbial attachment, surface colonization generally results in degradation of the mineral surface and a considerable increase in the reactive surface area. During this degradation process, microbes produce acids, bases, or ligands that interact with the mineral surface, promoting mineral dissolution and the eventual formation of secondary mineral phases (e.g., Bennett et al., 1996; Barker et al., 1997, Ehrlich, 1998). Thus, whenever conditions in the natural environment favor microbial surface colonization, microbial processes are likely to influence mineral dissolution (weathering) rates.

One of the most important pathways by which microbial attachment may influence mineral reaction rates is by modifying mineral-surface structure or otherwise interfering with the development of microtopographical surface features (e.g., etch pits at lattice defects). This is especially significant given the known dependence of surface-controlled mineral reaction rates on the microstructure of the surface. Numerous AFM studies have demonstrated the dependence of layer-by-layer growth or dissolution on the formation of growth spirals and etch pits at surface defects (e.g., Gratz et al, 1993; Liang et al., 1996; Jordan & Rammensee, 1998; Pina et al., 1998; Teng et al., 1998; Davis et al., 2000;

Higgins et al., 2000; Teng et al., 2000; Risthaus et al., 2001). The more recent use of vertical scanning interferometry (VSI) has successfully correlated observations of etch pit formation with surface normal retreat and “global” dissolution rates (Lüttge et al., 1999; Arvidson et al., 2003; Arvidson et al., 2004). A conceptual model for mineral dissolution has been inferred from these interferometric measurements of surface topography (e.g., Lasaga & Lüttge, 2001; Lasaga & Lüttge, 2003). In this model, mineral dissolution is not dominated by etch pit formation itself, but rather by extensive dissolution stepwaves that originate at the outskirts of etch pits. These stepwaves control the overall dissolution rate as well as the dependence on temperature and saturation state (Lasaga & Lüttge, 2004a,b; Lasaga & Lüttge, 2005). Most recently, VSI work has confirmed the importance of etch pit (defect) distribution as a controlling mechanism in calcite and dolomite dissolution (Arvidson et al., 2003; Lüttge et al., 2003). These studies provide a conceptual abiotic framework by which the biological influence on mineral-dissolution rates may be compared. They further predict that any microbial surface activity that modifies the influence of surface topography on dissolution rates will hold substantial implications for the mechanism of carbonate dissolution.

Since much of natural mineral dissolution is surface-controlled, it is of paramount importance to resolve any interaction between microbial attachment and the high-energy sites that produce etch pits. However such considerations must take into account the dynamic nature of the actively dissolving surface; i.e., during dissolution, the substrate may retreat beneath the attached bacteria. To this end, we present here some experiments aimed at achieving a beginning understanding of the interplay between biofilm formation and mineral-surface dynamics. Because of its relatively expedient dissolution and growth

kinetics, its mineral characteristics that allow for the preparation of smooth cleavage surfaces, and its biogeochemical significance, the calcite-dolomite mineral system was chosen as the substrate on which to test dynamic microbe-mineral interactions in a laboratory setting. Therefore, calcite and dolomite provide chemically and crystallographically similar surfaces with different solubilities and reactivities.

Careful consideration was also given to the selection of an experimental technique that could measure carbonate dissolution rates in the context of microbial attachment. Probing the nature of microbe-surface interactions in a quantifiable manner has previously only been achievable through the use of scanning probe microscopy (SPM) techniques. The power of these methods lies in their *in situ* ability to image live cells and their exquisite resolution of changes in microtopography as well as of microbial cell structure. However, these techniques suffer from the invasive nature of tip-sample interactions and their limited field of view. For instance, direct measurements of global surface dissolution rates are largely unattainable using SPM. A noninvasive imaging technique is needed that can both detect the microbe at the surface and quantify any resulting changes in mineral-surface topography, while maintaining both a high spatial resolution and a large field of view. Vertical scanning interferometry (VSI) meets these requirements and enables the measurement of both local dissolution (etch pits) and global dissolution rates (surface normal retreat) through comparison to a masked reference surface. Only one previous study has attempted to investigate microbe-mineral interactions using VSI (Lüttge and Conrad, 2004), in which surface colonization by *Shewanella oneidensis* MR-1 (hereafter called MR-1) was observed to largely prevent the

opening of etch pits on the calcite surface, despite undersaturated solution conditions. The authors hypothesized that this mode of dissolution inhibition was dependent upon both the biomass to surface area ratio and the rate at which the etch pits opened. However, these experiments employed a high cell titer and small reaction volume, thereby precluding any possibility of large-scale calcite dissolution from occurring. The current study extends our understanding of the effect of MR-1 on carbonate dissolution by implementing an experimental setup that employs a greater solution volume to mineral surface area ratio. Under these conditions finite calcite dissolution rates can be observed in the presence of MR-1, allowing for quantitative assessment of carbonate surface dynamics in the context of microbial attachment. Additionally, dolomite surfaces were used to determine the consequences of microbial surface colonization for much less reactive surfaces. In all of these attachment studies, MR-1 was used due to its propensity to form biofilms, ubiquity in the natural environment, and its use as a model microbe for bioremediation studies (Tiedje, 2002).

4.2 Experimental Methods

4.2.1 MR-1 Culture Preparation and Controls

Shewanella oneidensis strain MR-1, formerly *Shewanella putrefaciens* MR-1 (Myers and Nealson, 1988; Venkateswaren et al., 1999) was originally isolated as a dissimilatory iron and manganese reducing microbe, and obtained from the culture collection of the Nealson laboratory (University of Southern California). MR-1 was aerobically cultured

in either standard Luria-Bertani (LB) broth adjusted to pH 7.0, or a pH 7.4, low-nutrient medium, prepared to 1L using: 200 mg yeast extract, 100 mg peptone, 10 mL 1M HEPES, 10 mL 0.2M bicarbonate and 20 mL 1M lactate. The low-nutrient medium was used in order to minimize inhibition by nutrient organics on carbonate dissolution. In contrast, nutrient-rich 10% LB medium was used to achieve higher MR-1 cell concentrations in the test solutions. Each of the cultures was allowed to enter stationary phase as monitored by spectrophotometric absorbance measurements. The corresponding final A_{600} reading for the low-nutrient culture was 0.15, corresponding to a cell titer of $\sim 3 \times 10^8$ cells/mL. Stationary phase for the 10% LB medium was characterized by an A_{600} reading of 0.26-0.28, yielding a cell titer of $\sim 5 \times 10^8$ cells/mL. Two portions of each of the 10% LB and low-nutrient cultures were used as control solutions. The first control was a cell-free extract that was prepared through centrifugation of the culture at 9000 rpm for 30 min. The supernatant was decanted from the pellet and the centrifugation step repeated twice more. Following this procedure, the spectrophotometric absorbance A_{600} of the solution fell to 0. A second dead-cell control was prepared by heat-killing the cells through incubation above 45°C and below 55°C for 2.5 hours and then allowing the culture to cool and repeating the cycle two more times. During this procedure, the measured spectroscopic absorbance A_{600} of the solutions was observed to fall to 0.12 for the 10% LB solution and 0.10 for the low-nutrient solution. Viability of the dead-cell control was assessed by counting the number of colony-forming units (cfu) per volume plated on Luria-Bertani (LB) agar plates. It was determined for each of the solutions that less than 1 bacterial cell per mL of culture was microbiologically viable.

4.2.2 Reaction Conditions

Cleavage surfaces of calcite (CaCO_3) and dolomite ($\text{CaMg}(\text{CO}_3)_2$) were prepared using a razor blade and mounted on glass coverslips using sealing wax. The glass coverslips were in turn mounted on stainless steel coupons similar to those commonly used for AFM analysis. The purpose of the glass coverslip was to minimize metal exposure to the test solutions during the course of the experiments. At least two reference masks were applied to each crystal surface prior to reaction and allowed to cure for 24 hours. The masks used in this study were made using Permatex (www.permatex.com), a commercially-available high-temperature silicone gasket making compound. This type of mask has previously been used in abiotic calcite dissolution experiments where it was found to have no measureable effect on solution chemistry or observed rates (e.g., Arvidson et al., 2003). The crystals were reacted in 100x15mm Petri dishes containing 50 mL of cell culture or control solution. The Petri dishes were placed on a platform shaker set to 15 rpm for the duration of the experiment and left unsealed so that aerobic conditions were maintained throughout the experiment. For each experiment, multiple crystals of each species were reacted in each test solution. Further, each crystal had multiple masked regions for maximum internal controls. When comparing different mineral surfaces in the same test solution, all crystal species were placed in the same Petri dish and therefore exposed to the same experimental conditions. Due to the high number of complexation sites present on the microbe surfaces and organic species in solution, it was not possible to monitor calcium or carbonate species in solution during

the course of the experiment. The crystals were reacted in the test solutions for either 8 or 33.5 hours. Following the reaction periods, the solutions were decanted from the Petri dishes containing the crystals and re-measured for pH and absorbance. The pH of both the live MR-1 cultures and the control solutions tended to rise during the course of the experiment, reaching a maximum of 7.5 to 7.6 after 33.5 hours. The measured absorbances of the live MR-1 cultures fell slightly during the experiment, most likely as a result of attachment to the crystal surfaces and the bottom of the Petri dish. The absorbance of the cell-free and dead-cell controls were measured to be the same as at the beginning of the experiments.

Prior to imaging, the crystals were washed in a standardized fashion necessary for accurate dissolution rate comparisons in the context of cell attachment. Each stainless steel coupon (containing the test crystal) was lodged vertically in a 15 mL centrifuge tube using a pair of tweezers. The tube was gently filled with DIW, capped, rotated end-over-end and emptied. This procedure was repeated twice more for each crystal. Excess solution was wicked away from the edges of the crystals using a Kimwipe prior to imaging.

4.2.3 VSI and AFM Imaging and Measurements

A commercially-available MicroXAM MP-8 (ADE Phase-shift, Tucson, AZ) vertical scanning interferometer (VSI), equipped with 10x and 50x Nikon Mirau objectives, was

used to monitor biofilm development as well as to quantify carbonate dissolution rates. The manner by which this instrument creates topographic images of the surface are described in detail elsewhere (Lüttge et al., 1999). The 10x interferometric objective yields a 845 x 630 μm field of view, while the 50x objective allows for scan sizes of 165 x 125 μm . Images made at 50x magnification using white-light illumination provide a lateral resolution of $\sim 0.5 \mu\text{m}$, while maintaining a vertical resolution (i.e., step height) on the order of 1-2 nm. There are two basic types of images that can be generated from data sets acquired using VSI. The standard data file is a 2-dimensional (2D) topographic image similar to height images obtained using AFM, where topographic information is conveyed according to a color scale. In these images, bright colors typically indicate higher surface features on the image. The second image type used in this study is a 3-dimensional (3D) solid-model representation of the topographic information contained in the VSI data file.

Interferometry measures relative surface height. By placing an inert mask on the surface and measuring the average height difference between the unreacted and reacted surfaces, an absolute value of surface normal retreat may be determined. Thus, during dissolution, changes in average height $\Delta \bar{h}$ made at time intervals Δt yields a surface normal retreat velocity, $v_{[hkl]}$:

$$\frac{\Delta \bar{h}}{\Delta t} = v_{[hkl]}.$$

$$r = v_{[hkl]} \bar{V}^{-1}.$$

This approach allows a simple and straightforward calculation of surface-area rates from measurements of average surface heights ($\Delta \bar{h}$) (e.g., Lüttge et al., 1999).

Additional high-resolution images of attached MR-1 cells as well as of microbial trenches were acquired *ex situ*, using a Multimode Nanoscope III AFM (Digital Instruments, Santa Barbara, CA, USA). This instrument was equipped with a J piezoelectric scanner with a maximum range of 130 x 130 μm . While Tapping Mode is often the preferred technique for imaging biological materials, the MR-1 cells were found to be attached strongly enough to the crystal surface to allow for Contact Mode imaging using minimal contact forces. It was found that this imaging technique provided the best resolution of both surface topography and attached cells.

4.3 Results and Discussion

4.3.1 Surface Colonization on Carbonate Surfaces

MR-1 biofilm development on the carbonate test surfaces was monitored at time intervals using the interferometer. Time series analysis revealed that the surfaces underwent continuous colonization during the course of the 33.5 hour exposure period studied. While the rate of microbial attachment was observed to vary with both cell titer and the choice of calcite or dolomite substrate, the morphologic progression of biofilm

development was consistent among the test surfaces. The early stages of surface colonization were characterized by the formation of a honeycomb-shaped network of cells surrounding cell-free portions of the crystal surface (Fig. 4.1a-c). Occasionally, initial surface colonization seemed to occur through microcolony formation, especially in the low-nutrient media (Fig. 4.2). Subsequent cell attachment deposited a nearly continuous monolayer biofilm on the carbonate substrates by the end of the 33.5 hour exposure period (Fig. 4.1d). It was apparent from the topographic images acquired using VSI that the attached cells were surrounded by organic material, possibly a conditioning film or the result of early extracellular polysaccharide (EPS) production (Fig. 4.3). The physical dimensions of the associated organic material as well as of the cells themselves could be directly determined from the VSI images (Fig. 4.4). The cells were found to range from 1 to 2.5 microns in length and from 400 to 650 nm in diameter. The associated organic material was consistently measured to rise 200 to 250 nm above the surface of the crystal. It was found that much of the organic material associated with the attached cells could be removed if the crystal surfaces were exposed to a direct stream of DIW from a wash bottle soon after removal from the experimental chambers. Subsequent VSI imaging revealed clearly visible entrenched cells arranged in the same patterns as previously discussed, but less obscured by associated organic material (Fig. 4.5). However, this washing step also caused some of the attached cells on the surface to lyse, as was evidenced by measured cell dimensions (cell diameters on the order of 100 nm) that were significantly smaller than undamaged cells.

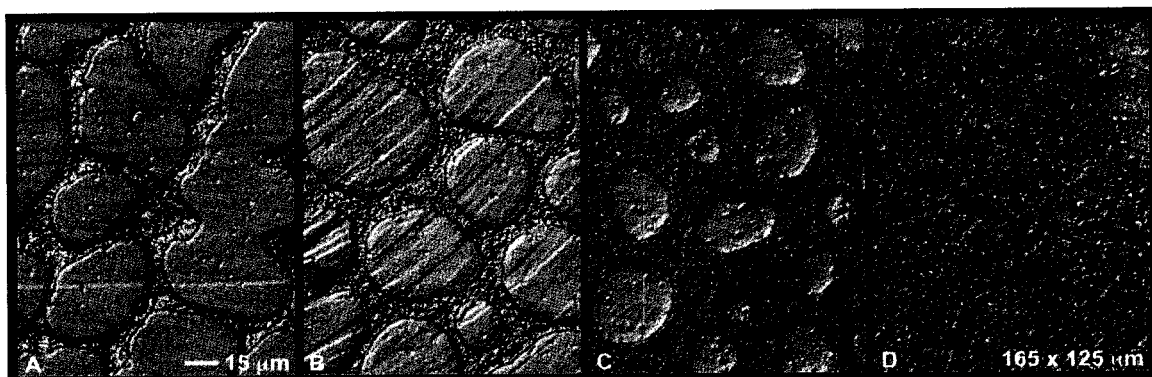


Fig. 4.1 MR-1 biofilm morphology and development on dolomite after A) 6 hours, B) 8 hours and C) 16 hours exposure to MR-1 cultures in 10% LB media. (A-C) indicates that initial MR-1 surface colonization exhibited a “honeycomb” morphology that progressively thickened until a monolayer of cells covered the surface. D) After 25 hours of exposure to MR-1 in the low-nutrient medium, the dolomite surface is covered with a nearly continuous monolayer biofilm. The biofilm organics are approximately 250 nm tall, punctuated by cells that vary between 550 and 650 nm in height. (All images are 165x125 μm .)

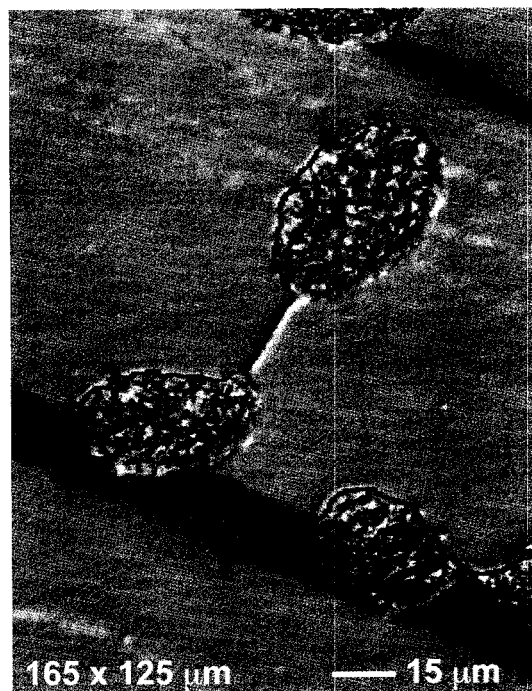


Fig. 4.2 Occasionally, initial surface colonization appeared to occur through microcolony formation, especially by cultures grown in the low-nutrient medium. Here small colonies of 5-10 cells and associated organic material begin to cover the calcite surface after 6 hours exposure to MR-1 culture in the low-nutrient medium.

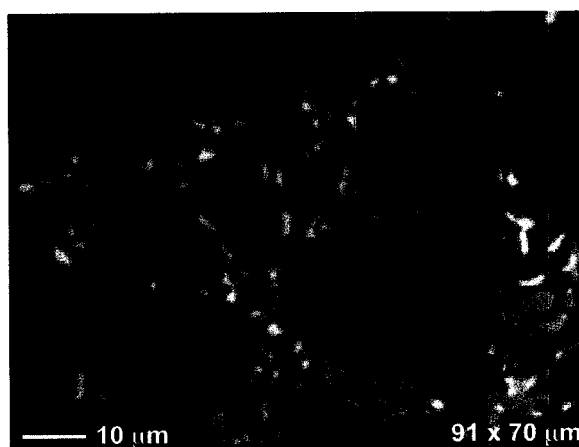


Fig. 4.3 2D VSI image of MR-1 surface colonization on a dolomite surface after 9 hours. This early biofilm consists of taller (bright-yellow) cells and associated lower (dark yellow) organic material.

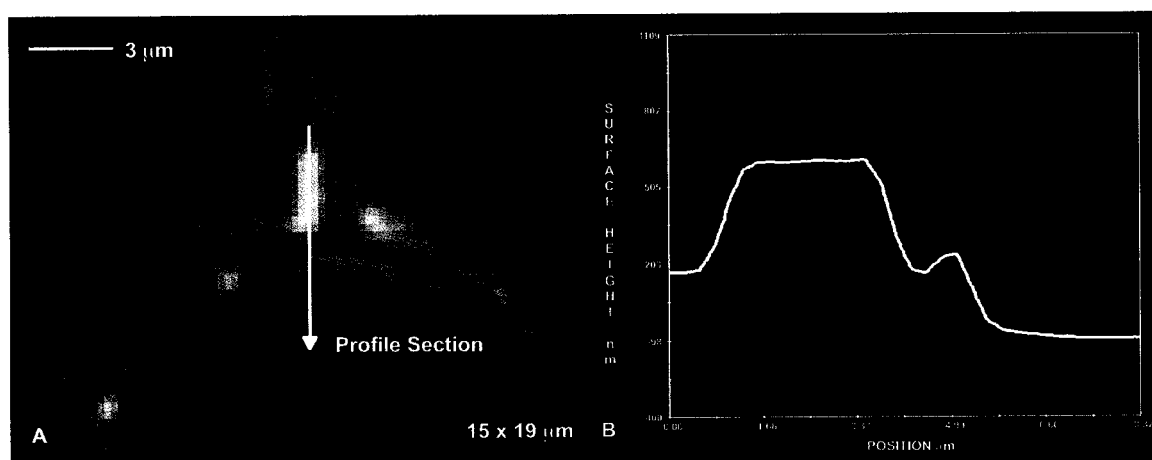


Fig. 4.4 Cross-section measurements of a single MR-1 cell on a dolomite surface and its associated organic material. Here, the cell is approximately 600 nm in diameter, 2 microns long, and the associated organic material rises 200 nm above the crystal surface.

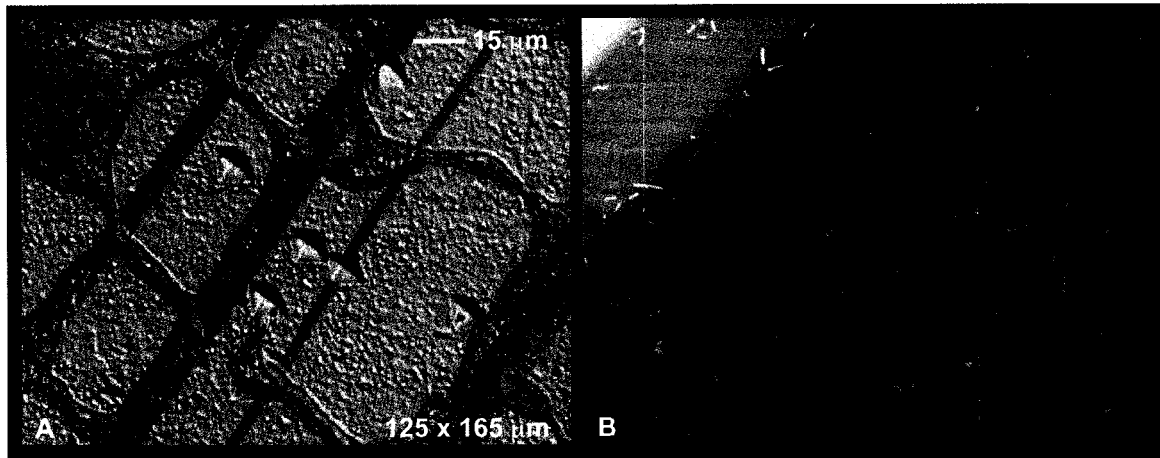


Fig. 4.5 MR-1 surface colonization on calcite after 2 hours exposure to MR-1 in the 10% LB medium. Etch pits tended to develop within the honeycomb biofilm structure during the early stages of surface colonization. A) 3-D plot of biofilm before washing B) 2D VSI image of entrenched cells on calcite following the removal of associated organics (both images are 125x165 µm)

4.3.2 Role of Surface Colonization in Determining Calcite Dissolution Rate

Calcite dissolution rates were measured in the context of microbial attachment by comparing masked portions of the crystal surface to those regions exposed to the experimental test solutions (Fig. 4.6). The measured surface normal retreats and corresponding dissolution rates for calcite crystals removed after 8 and 33.5 hours are contained in Table 4.1. Measured dissolution rates differed markedly between the two growth media. Despite its lower initial pH, calcite dissolution in the 10% LB solution was much slower than in the low-nutrient solution, probably the result of inhibition by the concentrated organics in the richer medium. Nonetheless, for both of the nutrient conditions employed, comparison of measured calcite dissolution rates for crystals exposed to MR-1 cultures with those obtained in the cell-free control solutions, indicated that MR-1 surface colonization had a significant effect on calcite dissolution rates (Figs. 4.7 and 4.8). The presence of live MR-1 cells in the 10% LB medium resulted in a 69% reduction in the calcite dissolution rate relative to the cell-free controls, while measurements in the low-nutrient medium yielded a calcite dissolution rate that was 43% slower than the dissolution rate observed for the cell-free control solutions. These differences in reaction rate are easily visualized by comparing the masked surfaces to the reacted surfaces in the 3D model images in figures 4.7 and 4.8. Insight into the mechanism by which the MR-1 cultures retarded calcite dissolution may be gained by looking at the results for the heat-killed MR-1 control solutions given in Table 4.1. The measured calcite dissolution rates in solutions containing heat-killed MR-1 cells were similar to those rates measured for the cell-free controls. Since the heat-killed cells were

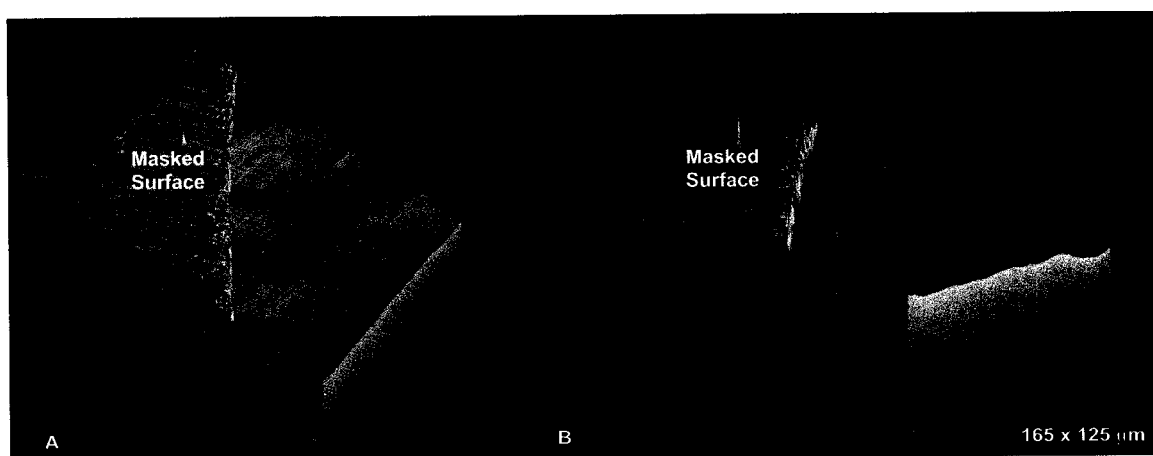


Fig. 4.6 Images showing the extent of dissolution between masked and unmasked areas of a calcite crystal following 4 hours of reaction in the cell-free control solutions (low-nutrient medium). The previously masked portion of the calcite surface is apparent as the taller (unetched) surface on the left side of the image. Analysis of the data contained in these images revealed 295 nm of average retreat between the reacted and unreacted portions of the crystal surface. The two images represent different perspectives of the same data set.

Table 4.1 – Calcite Dissolution Measurements after 8 and 33.5 Hours

Growth Medium	Solution	Cell Titer (cells/mL)	8 HOURS		33.5 HOURS	
			Retreat (nm)	Rate (mol•cm⁻²•s⁻¹)	Retreat (nm)	Rate (mol•cm⁻²•s⁻¹)
10% LB	<i>Cell-Free Control</i>	---	76 ± 13	7.15x10 ⁻¹²	667 ± 94	1.50x10 ⁻¹¹
	<i>Shewanella Culture</i>	~5x10 ⁸	43 ± 5	4.04x10 ⁻¹²	210 ± 18	4.72x10 ⁻¹²
	<i>Heat-Killed</i>	---	66 ± 7	6.21x10 ⁻¹²	591 ± 65	1.33x10 ⁻¹¹
	<i>Pristine Growth Media</i>	---	172 ± 20	1.62x10 ⁻¹¹	---	---
Low-Nutrient	<i>Cell-Free Control</i>	---	576 ± 72	5.42x10 ⁻¹¹	2768 ± 291	6.21x10 ⁻¹¹
	<i>Shewanella Culture</i>	~3x10 ⁸	343 ± 54	3.22x10 ⁻¹¹	1579 ± 118	3.54x10 ⁻¹¹
	<i>Heat-Killed</i>	---	609 ± 71	5.73x10 ⁻¹¹	2611 ± 217	5.86x10 ⁻¹¹
	<i>Pristine Growth Media</i>	---	1363 ± 111	1.28x10 ⁻¹⁰	---	---

Note: Rate data represents average measurements determined from at least five transects from each of five masked areas and from at least two different crystals. The ± error reflected in the retreat data represents the maximum difference between measurements along different transects.

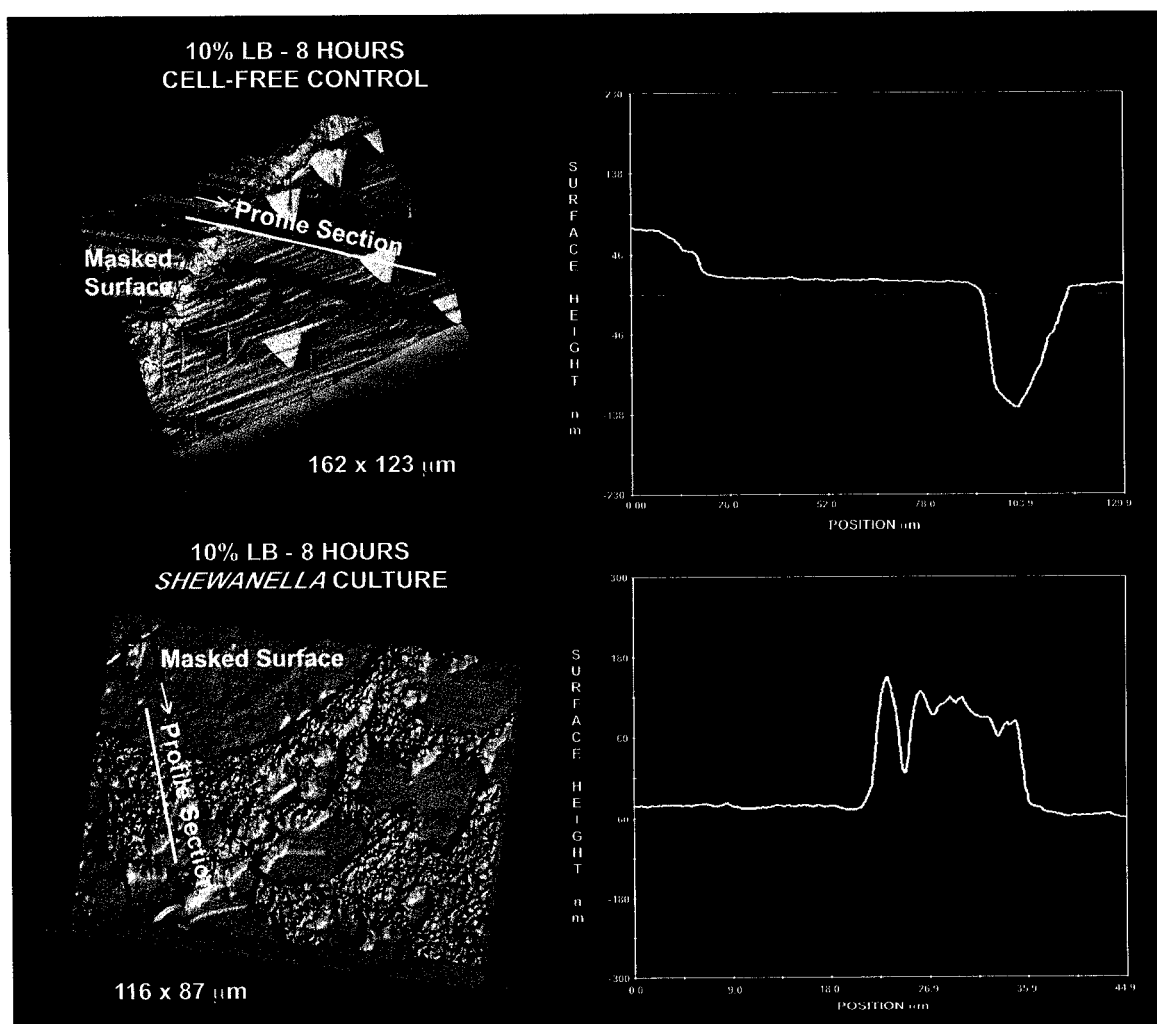


Fig. 4.7 Calcite dissolution relative to masked portions of the crystal surface after 8 hours of exposure to cell-free controls and MR-1 cell cultures in the 10% LB medium. Average measurements of calcite dissolution for the two systems are given in Table 1.

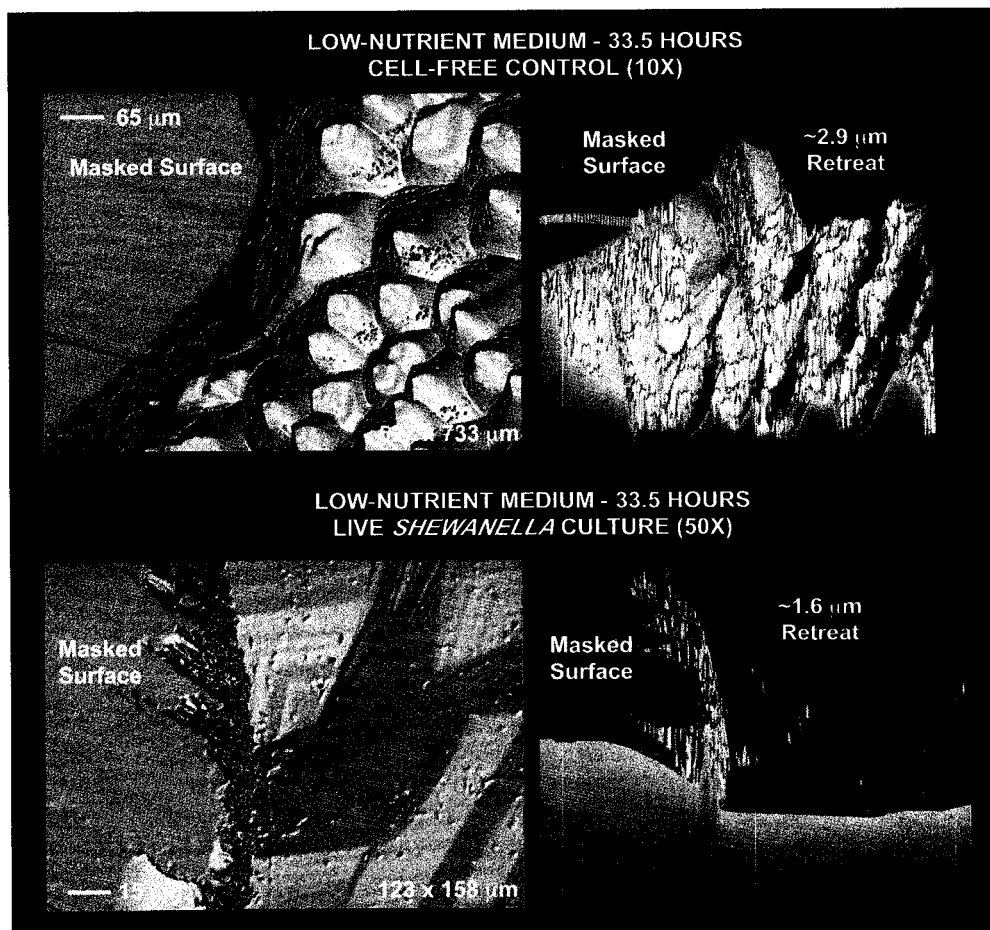


Fig. 4.8 Calcite dissolution relative to masked portions of the crystal surface after 33.5 hours of exposure to cell-free controls and MR-1 cell cultures in the low-nutrient medium. Average measurements of calcite dissolution for the two systems are given in Table 1.

not found to attach to the surface, it seems that the measured inhibition of calcite dissolution in the presence of live MR-1 cells resulted from the physical attachment of the cells to the surface. This attachment may have slowed calcite dissolution by interfering with the development of etch pits on the crystal surface, as has been previously described by Lüttge and Conrad (2004). It follows that the concentration of cells in the experimental solutions (cell titer) that was available for attachment to the mineral-surface may have been a determining factor in the dissolution of calcite under these conditions. The data in Table 4.1 supports this concept, where the 10% LB medium with the higher initial cell titer also yielded the greater reduction in the measured calcite dissolution rate. Lüttge and Conrad (2004) demonstrated that in the more extreme case of even higher cell titer and low reactive volumes, MR-1 attachment was capable of almost complete arrestment of calcite dissolution. Although the calcite dissolution measurements in this study were conducted for only two cell cultures and their control splits, these new results confirm the existence of a dynamic relationship between surface colonization and etch pit development on calcite.

4.3.3 Role of Surface Colonization in Dolomite Dissolution

As expected, the less reactive dolomite surfaces were relatively inert over the short reaction times employed in this study. While etch pits are detectable on the calcite surfaces within ten minutes of reaction with either the cell-free control solutions or the MR-1 cultures, no dissolution was observed on the dolomite surfaces during the 33.5 hour experiment. This difference in reactivity is especially apparent when comparing

masked and unmasked regions of the dolomite surfaces (Fig. 4.9) to those on calcite surfaces (Fig. 4.10). The stability of the dolomite surfaces seemed to significantly affect cell attachment rates. At each time step the dolomite surfaces were observed to have approximately twice the attached cell density of the calcite surfaces. (Although dissolution features on the calcite surface made assessment of attached cells much more difficult, especially after longer exposure times.) This result indicates that cell attachment occurred more slowly on actively dissolving calcite surfaces than on the less dynamic dolomite surfaces. Further, after longer exposure periods, it became clear that the majority of visible cells on the calcite surfaces were attached to the rims of large etch pits. This observation matches the results of an earlier study (Davis & Lüttge, 2005) and further indicates that conditions for microbial attachment are less favorable near the centers of dissolution where the surface is most dynamic.

4.3.4 Role of Microbial Entrenchment in Carbonate Dissolution

Lüttge and Conrad (2004) discovered that some of the attached MR-1 cells were actually entrenched in the calcite surface by as much as one third of their cell volume, as quantified by VSI. This was determined by measurements of microbial trenches left on the surface once cells were removed. Microbial entrenchment was also found to occur in this study (Fig. 4.11). Further, high-resolution imaging of the attached cells using AFM demonstrated that calcite dissolution was localized to the cell-mineral interface and did not produce centers from which additional calcite dissolution could occur. However, in

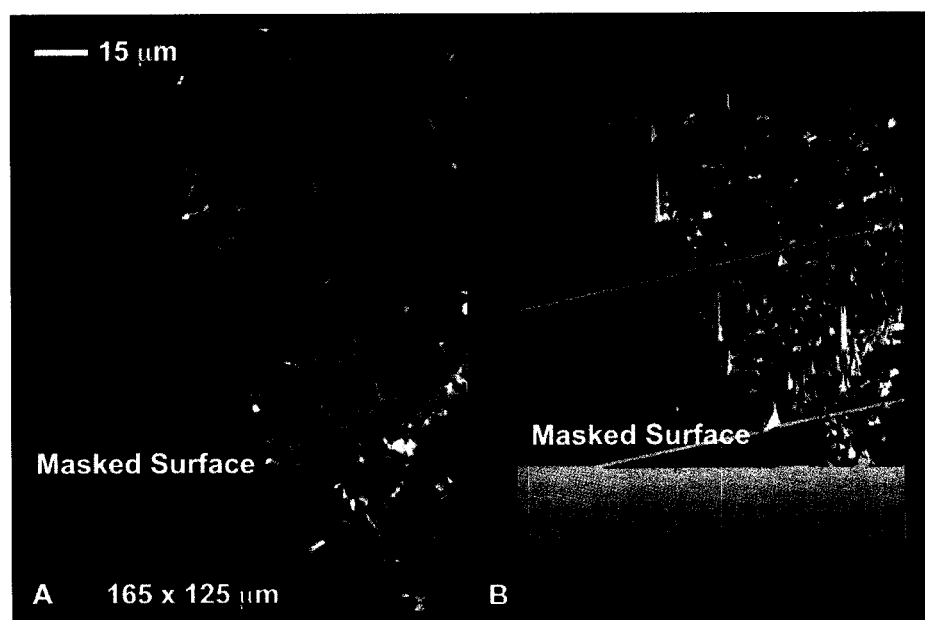


Fig. 4.9 Images showing the masked and unmasked regions of a dolomite crystal surface following 4 hours of exposure to MR-1 cells in the low-nutrient medium. These VSI images reveal that no dolomite dissolution occurred during the reaction period. Instead, a number of MR-1 cells have attached to the surface along with a thin organic film. The unreacted surface (previously masked) is apparent as the smooth surface on the left side of the images.

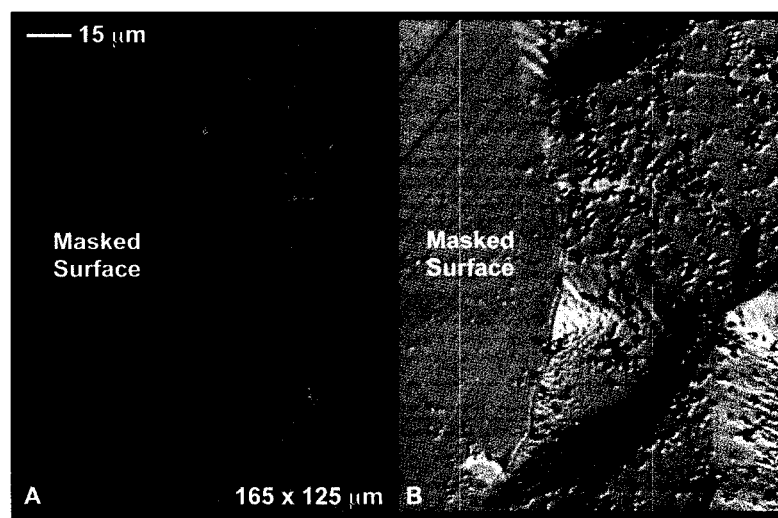


Fig. 4.10 Images showing the masked and unmasked regions of a calcite crystal surface following 4 hours exposure to MR-1 cells in the 10% LB medium. Attached MR-1 cells and dissolution features are readily apparent on the unmasked portion of the crystal while the masked surface remains smooth (unreacted).

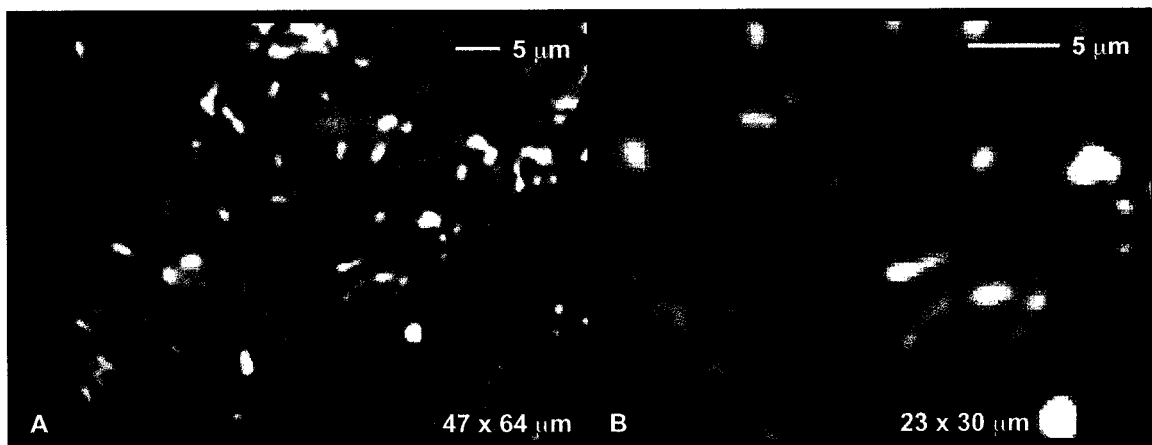


Fig. 4.11 Microbial trenches on the carbonate surface, indicating that MR-1 colonizes through irreversible attachment A) Image showing scratches residual from mechanical abrasion and removal of a dividing microbial cell. The scratches are 12 to 40 nm below the organics (EPS) coating the surface. B) Image showing a trench resulting from the removal of a microbe. This trench is 107 nm deep and 4.15 microns in length. The yellow rim (higher topography) surrounding the trench is indicative of microbial residue remaining attached to the surface. Thus, only part of the microbe was effectively removed from the surface. The remaining microbial material may be the portion of the cell wall that was in direct contact with the surface or residual EPS material aiding attachment. The length of the feature, including the yellow rim, is 5.3 microns, indicating that the removed cell was in the final stages of division or was actually a pair of cells attached at the poles (see Fig. 13).

one occurrence, a macrostep was observed to emerge from beneath two attached cells (Fig 4.12a). In general, it appeared that the microbes maintained exquisite control over dissolution processes occurring proximal to the cell interface, possibly to aid in irreversible attachment. The AFM images of trenches from which microbes had been completely removed were similar in shape to the bacteria-shaped depressions previously observed on ferric iron oxyhydroxide coatings under aerobic conditions by Grantham & Dove (1996). However, in this study, AFM observations indicated the presence of an organic lining that obscured the resolution of monomolecular steps and revealed an exceptionally flat pit-floor (Fig 4.12b). In some cases, trenches were exposed that clearly resulted from two or more cells that were attached polarly (Fig. 4.13). The more recently divided cell was apparent from the shallower portion of exposed trench. Therefore, trench depth was observed to vary with the duration that a particular microbe was present on the surface. Secondly, entrenchment seemed to occur soon after or coincident with cell division.

Interestingly, this study found that microbial trench formation occurred on dolomite in much the same manner as observed for calcite, despite the less favorable dissolution kinetics of dolomite (Fig 4.14). In fact, VSI measurements of trench depth showed that, on average, dolomite trenches were deeper than those found on calcite (Table 4.2). However, this result may be a function of the fact that the calcite surfaces to which trench depth is measured relative to are themselves actively retreating. Further, measurements of trench depth should not be considered definitive since only a relatively small number of the cells were successfully removed and those that were removed may have spent varying amounts of time actively metabolizing on the surface. Nonetheless, a few

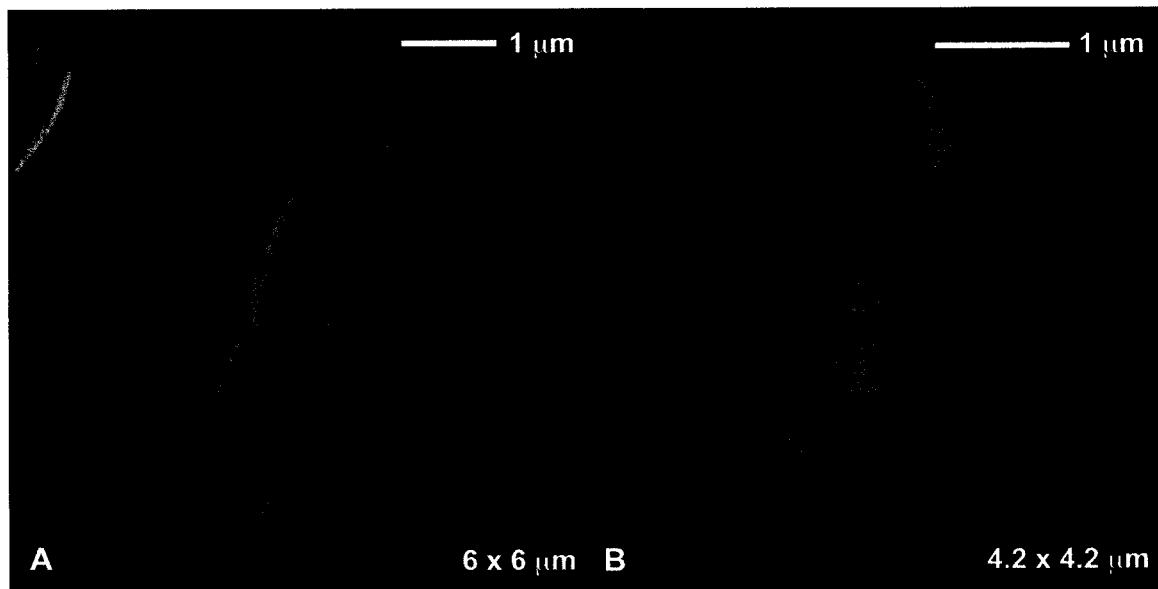


Fig. 4.12 AFM Images of calcite in the context of MR-1 Attachment A) Two MR-1 cells attached to the calcite surface with a macrostep emerging from underneath the microbes. B) Microbial trench lined with organics and characterized by a smooth floor.

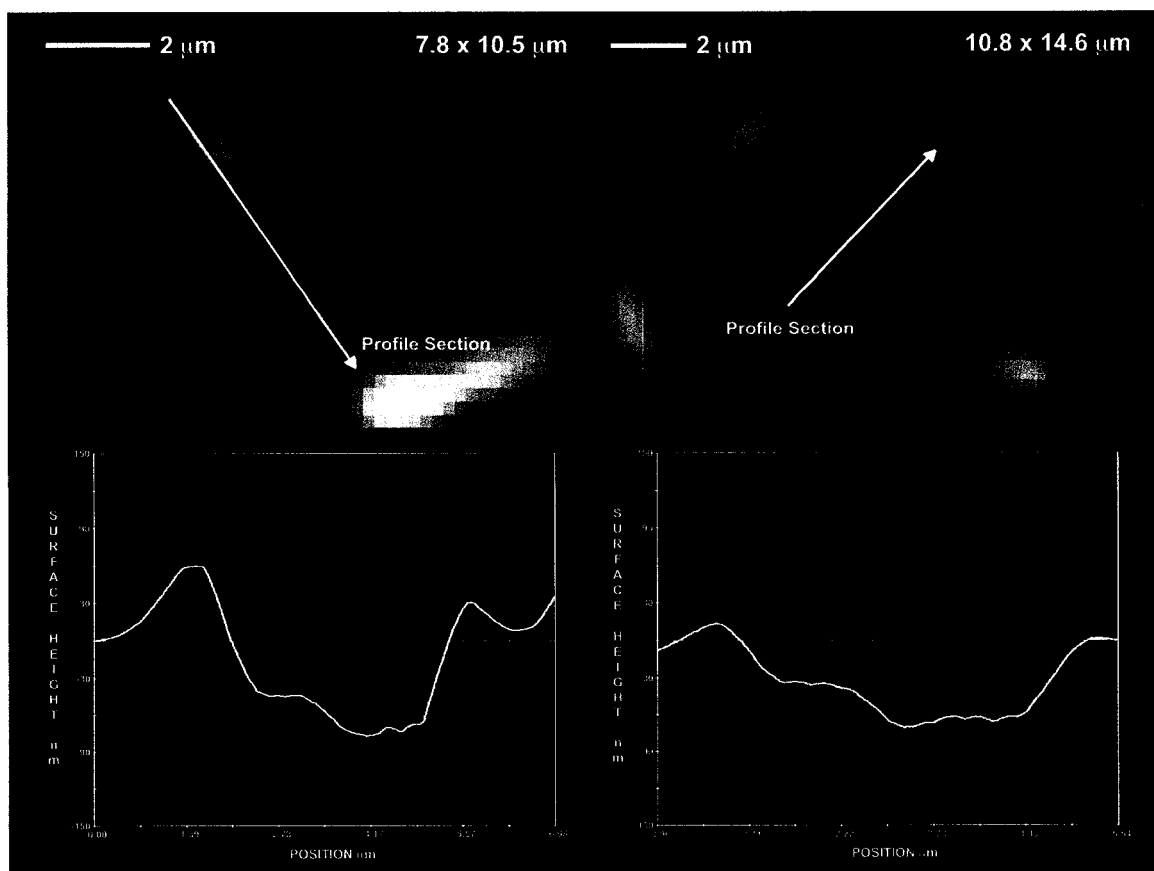


Fig. 4.13 Topographic profiles of trenches produced by dividing or polarly attached cells. In each of these examples, the more recently divided cell is apparent from the shallower portion of the exposed trench. Therefore, trench depth is observed to vary with the duration that a particular microbe is present on the surface. Secondly, entrenchment seems to occur soon after or coincident with cell division. It is clear from these profiles that the trenches are rimmed by microbial residue that may either be cell wall fragments that were in direct contact with the crystal surface or organic biofilm material that aided in attachment.

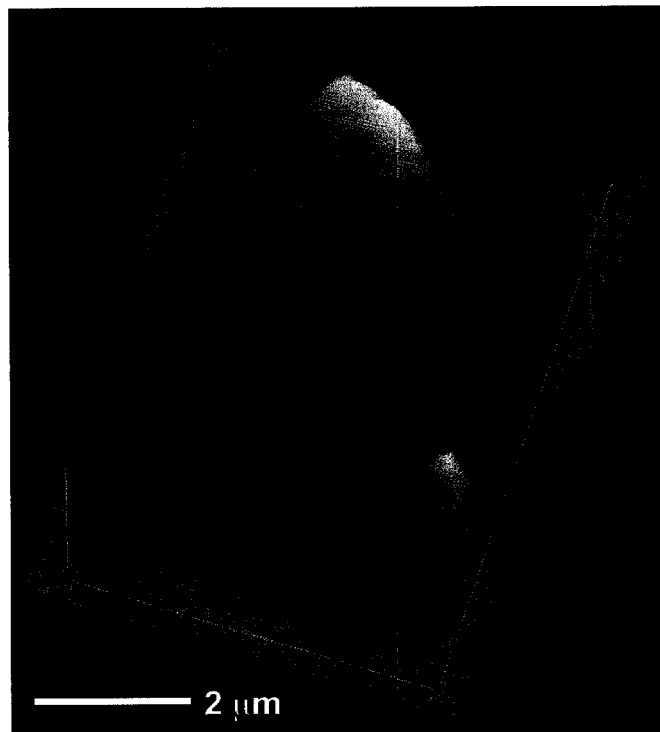


Fig. 4.14 3-D Plot of a MR-1 cell (top) and a microbial trench (bottom) on dolomite after 8 hours exposure to MR-1 in the low-nutrient medium. The pit is approximately 190 nm deep.

Table 4.2 – Trench Depth for Calcite and Dolomite after 8 and 33.5 Hours

	8 Hours	33.5 Hours
Calcite	182 nm	212 nm
Dolomite	217 nm	256 nm

Note: Data represents average measurements of at least 15 trenches for each time-step and mineral-surface.

conclusive observations can be drawn: 1) cells become entrenched relatively quickly, achieving near maximum depths after only 8 hours; 2) cells were not observed to be entrenched by more than 250 nm, or approximately one-third of their cell volume during this experiment; 3) no significant difference in trench depth was observed between the two nutrient media employed. The presence of trenches on the dolomite surfaces indicated that MR-1 was able to catalyze the removal of carbonate material during surface colonization to a much greater extent than occurred abiotically under the same conditions. This confirmed that the chemical environment at the cell-mineral interface differed substantially from that of the bulk. The apparent local decrease in free energy of the solution film in contact with the mineral-surface was most likely the result of CO₂ production during respiration and its associated decrease in solution pH. However, the observations of this study cannot rule out microbe-mediated changes in surface diffusion or weakening of Ca-CO₃ bond-strengths. Further insight into the potential mechanisms by which microbe-mineral surface processes may produce localized pit formation can be found in a recent modeling study (Lüttge et al., 2005). This study used Monte Carlo computer simulations to investigate etch pit formation in the context of microbial attachment for an AB crystal lattice. The modeling results demonstrated that calcite dissolution at the microbe-mineral interface could occur through either a local decrease in free energy or the weakening of certain bond strengths and that these mechanisms were operative for either atomically flat surfaces or in the presence of a strain field (dislocation). Further, the study demonstrated that organic molecules at the cell-mineral interface could prevent the propagation of stepwaves from escaping the outskirts of the

cell and was thus sufficient to reproduce the observed microbial control over trench formation (Lüttge et al., 2005).

If we measure the average volume of a trench and the density of cells on the surface, we can arrive at a reasonable “dissolution rate” based only upon the amount of material removed by the microbes during surface colonization. For instance, the volume of an average trench can be approximated as $2 \times 10^8 \text{ nm}^3$, corresponding to $5.4 \times 10^{-15} \text{ mol}$ of calcite or $3.1 \times 10^{-15} \text{ mol}$ of dolomite removed per microbial cell. If we assume an attached cell density of $0.01 \text{ cells}/\mu\text{m}^2$ and further assume that each of these cells is responsible on average for the aforementioned volume of excavated carbonate material, then a rate of $1.9 \times 10^{-13} \text{ mol} \cdot \text{cm}^{-2} \cdot \text{s}^{-1}$ for calcite and $1.1 \times 10^{-13} \text{ mol} \cdot \text{cm}^{-2} \cdot \text{s}^{-1}$ for dolomite can be expected after an 8 hour experiment. However, the significance of these trench “dissolution rates” to the overall dissolution processes occurring at the mineral-surface varies according to the carbonate mineral considered. In the case of calcite, the slowest dissolution rate directly measured in the presence of MR-1 cells is on the order of ~ 21 times greater than that estimated to occur as a consequence of cell entrenchment. Thus, the processes occurring at the cell-mineral interface are not a significant part of the overall calcite dissolution rate in the presence of MR-1. This contrasts with dolomite, where the only observable material removed either abiotically or in the presence of the microbes was that excavated during colonization. Therefore the presence of MR-1 actually increases the dissolution rate of dolomite relative to its abiotic control. This is because the surface colonization event itself removes more carbonate material than is otherwise achievable abiotically. However, the “dissolution rate” that occurs as a result of processes at the cell-mineral interface is only operative during active trench

development and cell attachment. For instance, Table 2 indicates that the average trench depth for dolomite does not change much between the 8 hour and 33.5 hour time-steps. If we had chosen to calculate “rates” at the later time periods, the apparent dolomite dissolution rate would be much reduced. Therefore the contribution from trench excavation to the overall dissolution rate is probably only important during the early stages of biofilm formation, where cells directly attach to the mineral-surface.

4.4 Conclusions

The results of this study indicate that MR-1 can significantly influence carbonate dissolution rates. Surface colonization by MR-1 was found to mediate carbonate dissolution kinetics through two distinct mechanistic pathways. First, bacterial attachment inhibited calcite dissolution by as much as 69%, probably through interference with etch pit development. The second mechanistic pathway was the catalytic removal of carbonate material at the cell-mineral interface (trench formation). The relative importance of these two competing effects was found to vary with the solubility and hence the background dissolution rate of the carbonate mineral. For the fast-dissolving mineral calcite, excavation of carbonate material at the cell-mineral interface was not found to be a significant component of the overall dissolution rate. However, in the case of the slower-dissolving mineral dolomite, mass-transfer during trench formation was the dominant result of surface colonization. The net result of this process is microbially-catalyzed dolomite dissolution that far outweighs the dissolution rate that would otherwise occur abiotically. Therefore, the surface colonization event

itself actually increased dolomite dissolution relative to abiotic rates. Of course surface colonization only occurs as long as cells continue to directly attach to the mineral-surface. Therefore the contribution from trench excavation to the overall dissolution rate is probably only important during the early stages of dissolution and biofilm formation. However, if the biofilm completely covers the surface, retarding long-term mineral dissolution, trench excavation may represent the dominant mechanism of material removal. In either of these cases, removal of the biofilm would expose the trenches produced during surface colonization, resulting in a substantial increase in the reactive surface area available for further dissolution. This may be an important process in soils where wet/dry cycles could result in microbial attachment followed by removal, thus enhancing carbonate dissolution rates.

While the quantitative results presented in this paper represent data from only two cell cultures and their control splits, the key findings of this study are also supported by other qualitative experiments (Davis et al., 2004; Lüttge and Conrad, 2004). Collectively, these experiments effectively demonstrate the range of mechanisms by which microbes may alter the dissolution rates of carbonate minerals. The findings of this study further demonstrate the dynamic and competitive relationship between mineral dissolution and surface colonization that may dominate microbially-mediated processes in natural environments. Especially relevant is the observation that far from equilibrium (more soluble minerals) microbial activity may retard dissolution rates by suppressing etch pit formation, while closer to equilibrium (less soluble minerals) the processes involved in bacterial attachment may actually enhance the overall dissolution rate. This concept offers an added complexity to the microbe-mineral relationship beyond the

physicochemical factors that govern microbial attachment. Still, the relevance of these processes to natural systems and for other environmentally-relevant microbes must in the end be determined experimentally through quantitative measurements of carbonate dissolution rates in the context of microbial attachment. If these microbially-mediated dissolution mechanisms can be shown to be environmentally-relevant, then the application of abiotically-measured carbonate dissolution rates to natural systems may need to be re-evaluated.

GENERAL CONCLUSIONS

Current rate laws assume that calcite growth and dissolution are governed by the saturation state, ignoring the potential influence of solution stoichiometry ($\text{Ca}^{2+}/\text{CO}_3^{2-}$ ratio) on growth and dissolution rates. The results of these studies demonstrate that solution stoichiometry plays a fundamental role in determining both the rates and anisotropy of calcite growth and dissolution. For the first time, the interaction between monomolecular surface steps and the cation/anion ratio in carbonate solutions has been resolved, yielding novel insight into the dominant mechanisms of calcite growth and dissolution. This nanoscale evidence, confirmed at multiple length-scales, demonstrates that changes in the $\text{Ca}^{2+}/\text{CO}_3^{2-}$ ratio at constant saturation determines both the kinetics and anisotropy of step advancement. Anisotropic step velocities, in turn, alter step generation rates at screw dislocations, thereby significantly affecting the overall growth and dissolution rate of calcite surfaces. Thus, our experiments indicate that changes in $\text{Ca}^{2+}/\text{CO}_3^{2-}$ ratio at constant saturation produces significant changes in calcite growth and dissolution rates that are normally only associated with changes in the saturation state. These results reflect different mechanistic roles for the cation and anion during both growth and dissolution of calcite, and suggests limitations on the application of concentration-based rate laws in solutions of varying ionic ratios. Further, this study offers clear demonstration that the crystal surface exerts a primary control on growth and dissolution rates through step-specific and defect-directed interactions, producing differences in rate that could not be predicted from considerations of bulk chemistry alone. Instead, specific knowledge of the surface and its interaction with particular solution-species is required for accurate rate prediction. Even in the absence of specific

knowledge of the surface, the results of these studies suggest that current saturation-based rate laws describing calcite growth and dissolution should be modified to include the relative concentrations of reactive species so as to account for the kinetic effects imposed by nonstoichiometric solutions.

In biologically-dominated natural systems, the surface that often matters the most is the microbial cell surface. Cell attachment to mineral-surfaces creates a specialized interface in which acids, bases, and ligands may enhance mineral dissolution rates (Bennett et al., 1996; Barker et al., 1997; Ehrlich, 1998). In order to achieve a mechanistic understanding of the way in which microbes alter the dissolution rates of carbonate minerals, the effect of *Shewanella oneidensis* MR-1 surface colonization on the dissolution rates of calcite (CaCO_3) and dolomite ($\text{CaMg}(\text{CO}_3)_2$) was assessed through qualitative analysis of etch pit development and quantitative measurements of surface-normal dissolution rates. The results of this study indicate that MR-1 can significantly influence carbonate dissolution rates. By quantifying and comparing the significant processes occurring at the microbe–mineral interface, the dominant mechanism of mineral dissolution during surface colonization was determined. MR-1 attachment under aerobic conditions was found to influence carbonate dissolution through two distinct mechanistic pathways: (1) inhibition of carbonate dissolution through interference with etch pit development and (2) excavation (catalytic removal) of carbonate material at the cell–mineral interface during irreversible attachment to the mineral surface. The relative importance of these two competing effects was found to vary with the solubility and hence the background dissolution rate of the carbonate mineral studied. For the faster-dissolving calcite substrates, inhibition of dissolution by attachment and subsequent

extracellular polysaccharide (EPS) production was the dominant effect associated with MR-1 surface colonization. This interference with etch pit development resulted in a 40–70% decrease in the surface normal dissolution rate relative to cell-free controls, depending primarily on the concentration of cells in solution. However, in the case of the slower-dissolving dolomite substrates, carbonate material displaced during the entrenchment of cells on the surface far outweighed the abiotic dissolution rate. Therefore, during the initial stages of surface colonization, dolomite dissolution rates were actually enhanced by MR-1 attachment. While these experiments demonstrated the importance of microbial attachment in determining carbonate dissolution rates, other results indicated that mineral-surface dynamics can, in turn, influence microbial attachment rates. These experiments found that surface colonization occurred more slowly on actively dissolving calcite surfaces than on the less dynamic dolomite and magnesite surfaces and that surface microtopographical features such as etch pits provide high-energy sites that favor microbial attachment. Collectively, these experiments effectively demonstrate the range of mechanisms by which microbes may alter the dissolution rates of carbonate minerals. The findings of this study further demonstrate the dynamic and competitive relationship between mineral dissolution and microbial surface colonization that may dominate microbially-mediated processes in natural environments.

REFERENCES

- Arnold, R.G., DiChristina, T.J., and Hoffman, M.R. (1988) Reductive dissolution of Fe(III) oxides by *Pseudomonas* sp. 200. *Biotechnology and Bioengineering* **32**, 1081-1096.
- Arvidson, R.S., Ertan, I.E., Amonette, J.E. and Lüttge, A. (2003) Variation in Calcite Dissolution Rates: A Fundamental Problem? *Geochimica Cosmochimica Acta* **67**, 1623-1634.
- Arvidson, R.S., Beig, M.S. and Lüttge, A. (2004) Single-crystal plagioclase feldspar dissolution rates measured by vertical scanning interferometry. *American Mineralogist* **89**, 51-56.
- Bakke, R., Characklis, W.G., Turakhia, M.H., and Yeh, A. (1990) Modeling a Monopopulation Biofilm System: *Pseudomonas Aeruginosa*, in Characklis, W. G., and Marshall, K. C., editors, *Biofilms*: John Wiley & Sons, Inc., New York, p. 487-520.
- Banfield, J.F., Welch, S.A., and Edwards, K.J. (1998) Microbes as Geochemical Agents: The Geochemical News, Number **96**, 11-17.
- Barker, W.W., Welch, S.A., and Banfield, J.F. (1997) Biogeochemistry of silicate mineral weathering, in Banfield, J. F., and Nealson, K. H., editors, *Geomicrobiology: Interactions between microbes and minerals*: Mineralogical Society of America Reviews in Mineralogy, v. **35**, 391-428.
- Bennett, P.C., and Hiebert, F.K. (1992) Microbial mediation of silicate diagenesis in organic-rich natural waters, in Kharaka, Y. K., Maest, A. S., editors, *Water-Rock Interaction*: AA Balkema, Rotterdam, p. 267-270.
- Bennett, P.C., Hiebert, F.K., and Choi, W.J. (1996) Microbial colonization and weathering of silicates in a petroleum-contaminated aquifer. *Chemical Geology* **132**, 45-53.
- Bennett, P.C., Hiebert, F.K., and Rogers, J.R. (2000) Microbial control of mineral-groundwater equilibria: Macroscale to microscale. *Hydrogeology Journal* **8**, 47-62.
- Boyd, R.D., Verran, J., Jones, M.V., and Bhakoo, M. (2002) Use of the Atomic Force Microscope to Determine the Effect of Substratum Surface Topography on Bacterial Adhesion. *Langmuir* **18**, 2343-2346.

- Burton, W.K., Cabrera, N. and Frank, F.C. (1951) The Growth of Crystals and the Equilibrium Structure of their Surfaces. *Phil. Trans. R. Soc.* **243**, 299.
- Cai, W.-J., Zhao, P. and Wang, Y. (2000) pH and pCO₂ microelectrode measurements and the diffusive behavior of carbon dioxide species in coastal marine sediments. *Mar. Chem.* **70**, 133-148.
- Characklis, W.G. (1990) Microbial Fouling, in Characklis, W. G., Marshall, K. C., editors, *Biofilms*: John Wiley & Sons, Inc., New York, p. 523-584.
- Chernov, A.A., Petrova, E.V. and Rashkovich, L.N. (2006) Dependence of the CaOx and MgOx growth rate on solution stoichiometry. Non-Kossel crystal growth. *Journal of Crystal Growth* **289**, 245-254.
- Davis, K.J., Dove, P.M. and De Yoreo, J.J. (2000) The role of Mg²⁺ as an impurity in calcite growth. *Science* **290**, 1134-1137.
- Davis, K.J., Dove, P.M., Wasylenki, L.E. and De Yoreo, J.J. (2004) Morphological consequences of differential Mg²⁺ incorporation at structurally distinct steps on calcite. *American Mineralogist* **89**, 714-720.
- Davis, K.J., Lüttge, A and Conrad, P.G. (2004) The Mechanistic Consequences of Microbial Surface Colonization on Carbonate Mineral Dissolution, in Wanty, R.B., and Seal, R.R., editors, *Proceedings of the 11th Symposium on Water-Rock Interactions*, v. 2: London, United Kingdom, Taylor and Francis Group, p. 1101-1105.
- Davis, K.J. and Lüttge, A. (2005) Quantifying the relationship between microbial attachment and mineral surface dynamics using vertical scanning interferometry (VSI) *American Journal of Science* **305**, 727-751.
- Davis, K.J., Nealson, K.H. and Lüttge, A. (2007) Calcite and dolomite dissolution rates in the context of microbe-mineral surface interactions. *Geobiology* **5**, 191-205.
- Dawson, M.P., Humphrey, B. and Marshall, K.C. (1981) Adhesion: A tactic in the survival strategy of a marine vibrio during starvation. *Current Microbiology* **6**, 195-99.
- DiChristina, T.J. and DeLong, E.F. (1994) Isolation of anaerobic respiratory mutants of *Shewanella putrefaciens* and genetic analysis of mutants deficient in anaerobic growth on Fe³⁺. *Journal of Bacteriology* **176**, 1468-1474.
- Ehrlich, H.L. (1996) *Geomicrobiology*. Marcel Dekker, New York. 719 pp.
- Ehrlich, H.L. (1998) Geomicrobiology: its significance for geology. *Earth-Science Reviews* **45**, 45-60.

- Ehrlich, H.L. (1999) Microbes as Geologic Agents: Their Role in Mineral Formation. *Geomicrobiology Journal* **16**, 135-153.
- Elderfield, H., Yu, J., Anand, P., Kiefer, T. and Nyland, B. (2006) Calibrations for benthic foraminiferal Mg/Ca paleothermometry and the carbonate ion hypothesis. *Earth and Planetary Science Letters* **250**, 633-649.
- Flemming, H.- C. and Schaule, G. (1996) Biofouling, *in* Heitz, E., Flemming, H.- C., Sand, W., editors, *Microbially Influenced Corrosion of Materials: Scientific and Engineering Aspects*: Springer, Berlin, p. 39-54.
- Fletcher, M. (1996) Bacterial Attachment in Aquatic Environments: A Diversity of Surfaces and Adhesion Strategies, *in* Fletcher, M., editor, *Bacterial Adhesion: Molecular and Ecological Diversity*: John Wiley and Sons, Inc., New York, p. 1-24.
- Fletcher, M. and Murphy, E. (2001) Transport of Microorganisms in the Subsurface: The Role of Attachment and Colonization of Particle Surfaces, *in*, Fredrickson, J. K., and Fletcher, M., editors, *Subsurface Microbiology and Biogeochemistry*: John Wiley & Sons, Inc., New York, p. 39-68.
- Fortin, D., Ferris, F.G. and Beveridge, T.J. (1997) Surface-Mediated Mineral Development by Bacteria, *in* Banfield, J. F., and Nealson, K. H., editors, *Geomicrobiology: Interactions between microbes and minerals*: Mineralogical Society of America, Reviews in Mineralogy, v. **35**, 161-177.
- Geesey, G.G. and Bryers, J.D. (2000) Biofouling of Engineered Materials and Systems, *in* Bryers, J. D., editor, *Biofilms II: Process Analysis and Applications*: John Wiley & Sons, Inc., New York, p. 237-280.
- Geesey, G.G., Beech, I., Bremer, P.J., Webster, B.J. and Wells, D.B. (2000) Biocorrosion. *In*: J. D. Bryers (Ed.), *Biofilms II: Process Analysis and Applications*. John Wiley & Sons, Inc., New York pp. 281-326.
- Grantham, M.C. and Dove, P.M. (1996) Investigation of bacterial-mineral interactions using Fluid-Tapping Mode Atomic Force Microscopy. *Geochimica et Cosmochimica Acta* **60**, 2473-2480.
- Grasso, B.F., Smets, K.A., Strevett, B.D., Machinist, C.J., Van Oss, R.F., Giese and Wu, W. (1996) Impact of Physiological State on Surface Thermodynamics and Adhesion of *Pseudomonas aeruginosa*. *Environmental Science and Technology* **30**, 3604-3608.
- Gratz, A.J., Hillner, P.E. and Hansma, P.K. (1993) Step dynamics and spiral growth on calcite. *Geochimica et Cosmochimica Acta* **57**, 491-495.

- Hamilton, W.A. (1995) Biofilms and Microbially Influenced Corrosion, in Lappin-Scott, H. M., and Costerton, J. W., editors, *Microbial Biofilms*: Cambridge University Press, New York, p. 171-182.
- Henriksen, K., Stipp, S.L.S., Young, J.R. and Bown, P.R. (2003) Tailoring calcite: Nanoscale AFM of coccolith biocrystals. *American Mineralogist* **88**, 2040-2044.
- Higgins, S.R., Bosbach, D., Eggleston, C.M., Knauss, K.G. (2000) Kink Dynamics and Step Growth on Barium Sulfate (001): A Hydrothermal Scanning Probe Microscopy Study. *J. Phys. Chem. B.* **104**, 6978-6982.
- Hiebert, F.K. and Bennett, P.C. (1992) Microbial control of silicate weathering in organic-rich ground water. *Science* **258**, 278-281.
- House, W. (1981) Kinetics of crystallization of calcite from calcium bicarbonate solutions. *J. Chem. Soc. Faraday Trans.* **77**, 341-359.
- Jahnke, R.A. and Jahnke, D.B. (2004) Calcium carbonate dissolution in deep sea sediments: Reconciling microelectrode, pore water and benthic flux chamber results. *Geochim. Cosmochim. Acta* **68**, 47-59.
- Jordan, G. and Rammensee, W. (1998) Dissolution rates of calcite (1014) obtained by scanning force microscopy: Microtopography-based dissolution kinetics on surface with anisotropic step velocities. *Geochimica et Cosmochimica Acta* **62**, 941-947.
- Kjelleberg, S. and Hermansson, M. (1984) Starvation-induced effects on bacterial surface characteristics. *Appl. Environ. Microbiol.* **48**, 497-503.
- Korber, D.R., Lawrence, J.R., Lappin-Scott, H.M. and Costerton, J.W. (1995) Growth of Microorganisms on Surfaces, in: Lappin-Scott, H. M., and Costerton, J. W., editors, *Microbial Biofilms*: Cambridge University Press, New York, p. 15-45.
- Kossel, W. (1927) Zur Theorie des Kristallwachstums. *Nachrich. Ges. Wiss. Gottingen, Math.-phys. Klasse*, 135-143.
- Lahann, R.W. and Siebert, R.M. (1982) A kinetic model for distribution coefficients and application to Mg-calcites. *Geochimica et Cosmochimica Acta* **46**, 2229-2237.
- Land, T.A., De Yoreo, J.J. and Lee, J.D. (1997) An *in situ* AFM investigation of canavalin crystallization kinetics. *Surf. Sci.* **384**, 136-155.
- Lasaga, A.C. and Lüttge, A. (2001) Variation of Crystal Dissolution Rate Based on a Dissolution Stepwave Model. *Science* **291**, 2400-2404.

- Lasaga, A.C. and Lüttge, A. (2003) A model for crystal dissolution. *Eur. J. Mineral.* **15**, 603-615.
- Lasaga, A.C. and Lüttge, A. (2004a) Mineralogical approaches to fundamental crystal dissolution kinetics. *American Mineralogist* **89**, 527-540.
- Lasaga, A.C. and Lüttge, A. (2004b) Mineralogical approaches to fundamental crystal dissolution kinetics – Dissolution of an A(3)B structure. *European Journal of Mineralogy* **16**, 713-729.
- Lasaga, A.C. and Lüttge, A. (2005) Kinetic justification of the solubility product: Application of a general kinetic dissolution model. *Journal of Physical Chemistry B* **109**, 1635-1642.
- Lea, A.S., Amonette, J.E., Baer, D.R., Liang, Y. and Colton, N.G. (2001) Microscopic Effects of Carbonate, Manganese, and Strontium Ions on Calcite Dissolution. *Geochimica et Cosmochimica Acta* **65**, 369-379.
- Lens, P., Moran, A.P., Mahony, T., Stoodley, P. and O'Flaherty, V. (2003) Biofilms in Medicine, Industry and Environmental Biotechnology: Characteristics, Analysis and Control: IWA Publishing, Cornwall, 610 pp.
- Liang, Y., Baer, D.R., McCoy, J.M., Amonette, J.E. and LaFemina, J.P. (1996) Dissolution kinetics at the calcite-water interface. *Geochimica et Cosmochimica Acta* **60**, 4883-4887.
- Little, B.J., Wagner, P.A., Characklis, W.G. and Lee, W. (1990) Microbial Corrosion, in Characklis, W. G., Marshall, K. C., editors, Biofilms: John Wiley & Sons, Inc., New York, p. 635-670.
- Little, B.J., Wagner, P.A. and Lewandowski, Z. (1997) Spatial Relationships Between Bacteria and Mineral Surfaces, in Banfield, J. F., and Nealson, K. H., editors, Geomicrobiology: Interactions between microbes and minerals: Mineralogical Society of America Reviews in Mineralogy, v. **35**, 123-155.
- Lorens, R.B. (1981) Strontium, cadmium, manganese, and cobalt distribution coefficients in calcite as a function of calcite precipitation rate. *Geochimica et Cosmochimica Acta* **45**, 553-561.
- Lovley, D.R. and Phillips, E.J.P. (1988) Novel mode of microbial energy metabolism: Organic carbon oxidation coupled to dissimilatory reduction of iron or manganese. *Appl. Environ. Microbial.* **54**, 1472-1480.
- Lovley, D.R., Coates, J.D., Blunt-Harris, E.L., Phillips, E.J.P. and Woodward, J.C. (1996) Humic substances as electron acceptors for microbial respiration. *Nature* **382**, 445-448.

- Lovley, D.R. and Blunt-Harris, E.L. (1999) Role of Humic-Bound Iron as an Electron Transfer Agent in Dissimilatory Fe(III) Reduction. *Applied and Environmental Microbiology* **65**, 4252-4254.
- Lowenstein, T.K., Timofeeff, M.N., Brennan, S.T., Hardie, L.A. and Demicco, R.V. (2001) Oscillations in Phanerozoic Seawater Chemistry: Evidence from Fluid Inclusions. *Science* **294**, 1086-1088.
- Lower, S.K., Tadanier, C.J. and Hochella Jr., M.F. (2000) Measuring interfacial and adhesion forces between bacteria and mineral surfaces with biological force microscopy. *Geochimica et Cosmochimica Acta* **64**, 3133-3139.
- Lower, S.K., Tadanier, C.J. and Hochella Jr., M.F. (2001a) Dynamics of the Mineral-Microbe Interface: Use of Biological Force Microscopy in Biogeochemistry and Geomicrobiology. *Geomicrobiology Journal* **18**, 63-76.
- Lower, S.K., Hochella Jr., M.F. and Beveridge, T.J. (2001b) Bacterial recognition of mineral surfaces: nanoscale interactions between *Shewanella* and α -FeOOH. *Science* **292**, 1360-1363.
- Lüttge, A., Bolton, E.W., Lasaga, A.C. (1999) An interferometric study of the dissolution kinetics of anorthite: The role of reactive surface area. *American Journal of Science* **299**, 652-678.
- Lüttge, A. and Conrad, P.G. (2004) Direct Observation of Microbial Inhibition of Calcite Dissolution. *Applied and Environmental Microbiology* **70**, 1627-1632.
- Lüttge A., Winkler, U. and Lasaga, A.C. (2003) Interferometric study of dolomite dissolution: A new conceptual model for mineral dissolution. *Geochimica et Cosmochimica Acta* **67**, 1099-1116.
- Lüttge, A., Zhang, L. and Nealson, K.H. (2005) Mineral surfaces and their implications for microbial attachment: Results from Monte Carlo simulations and direct surface observations *American Journal of Science* **305**, 766-790.
- Marshall, K.C. (1996) Adhesion as a strategy for access to nutrients. In: *Bacterial Adhesion* (Ed. Fletcher M). John Wiley & Sons, Inc., New York. pp. 59-87.
- Mills, A.L. and Powelson, D.K. (1996) Bacterial Interactions with Surfaces in Soils, in Fletcher, M., editor, *Bacterial Adhesion: Molecular and Ecological Diversity*: John Wiley and Sons, Inc., New York, p. 25-58.
- Morse, J.W. (1983) The kinetics of calcium carbonate dissolution and precipitation. In: *Carbonates: Mineralogy and Chemistry*, Rev. Mineral. Society of America (ed. Reeder R), Washington, DC, vol. 11, pp. 227-264.

- Morse, J.W. and Arvidson, R.S. (2002) The dissolution kinetics of major sedimentary carbonate minerals. *Earth Science Reviews* **58**, 51-84.
- Morse, J.W. and Bender, M.L. (1990) Partition coefficients in calcite: Examination of factors influencing the validity of experimental results and their application to natural systems. *Chemical Geology* **82**, 265-277.
- Morse J.W. and Mackenzie, F.T. (1990) *Geochemistry of Sedimentary Carbonates*. Elsevier, Amsterdam.
- Mueller, B., Wang, Y., Dittrich, M. and Wehrli, B. (2003) Influence of organic carbon sequestration on calcite dissolution in surficial sediments of a freshwater lake. *Water Res.* **37**, 4524-4532.
- Myers, C. and Nealson, K. (1988) Bacterial manganese reduction and growth with manganese oxide as the sole electron acceptor. *Science* **240**, 1319-1321.
- Nealson, K.H. and Myers, C.R. (1992) Microbial reduction of manganese and iron: New approaches to carbon cycling. *Appl. Environ. Microbial.* **58**, 439-443.
- Newman, D.K. and Kolter, R. (2000) A role for excreted quinones in extracellular electron transfer. *Nature* **405**, 94-97.
- Nielsen, A.E. (1983) Precipitates: formation, coprecipitation, and aging. In *Treatise on Analytical Chemistry* (ed. I.M. Kolthoff and P.J. Elving), pp. 269-347. Wiley.
- Paine, S.G., Lingood, F.V., Schimmer, F. and Thrupp, T.C. (1933) IV. The relationship of microorganisms to the decay of stone. *Roy. Soc. Phil. Trans.* **222B**, 97-127.
- Paquette, J. and Reeder, R.J. (1990) New type of compositional zoning in calcite: Insights into crystal-growth mechanisms. *Geology* **18**, 1244-1247.
- Paquette, J. and Reeder, R.J. (1995) Relationship between surface structure, growth mechanism, and trace element incorporation in calcite. *Geochim. Cosmochim. Acta* **59**, 735-749.
- Pina, C.M., Becker, U., Risthaus, P., Bosbach, D. and Putnis, A. (1998) Molecular-scale mechanisms of crystal growth in barite. *Nature* **395**, 483-486.
- Prince, A. (1996) *Pseudomonas Aeruginosa*: Versatile Attachment Mechanisms, in Fletcher, M., editor, *Bacterial Adhesion: Molecular and Ecological Diversity*: John Wiley and Sons, Inc., New York, p. 183-200.

- Reddy, M.M. (1977) Crystallization of calcium carbonate in the presence of trace concentrations of phosphorus-containing anions. I. Inhibition by phosphate and glycerophosphate ions at pH 8.8 and 25°C. *J. Cryst. Growth* **41**, 287-295.
- Reddy, M.M. and Gaillard, W.D. (1981) Kinetics of calcium carbonate (calcite)-seeded crystallization: Influence of solid/solution ratio on the reaction rate constant. *J. Colloid Interface Sci.* **80**, 171-178.
- Reddy, M.M. and Nancollas, G.H. (1971) The crystallization of calcium carbonate I. Isotopic exchange and kinetics. *J. Colloid Interface Sci.* **36**, 166-172.
- Reddy, M.M. and Nancollas, G.H. (1973) Calcite crystal growth inhibition by phosphates. *Desalination*. **12**, 61-73.
- Reeder, R.J. and Rakovan, J. (1999) Surface Structural Controls on Trace Element Incorporation During Crystal Growth. In *Growth, Dissolution and Pattern Formation in Geosystems*. B. Jamtveit and P. Meakin, eds. Kluwer Academic Publishers, Dordrecht. pg. 143-162.
- Risthaus, P., Bosbach, D., Becker, U. and Putnis, A. (2001) Barite scale formation and dissolution at high ionic strength studied with atomic force microscopy. *Colloids and Surfaces A: Physiochemical and Engineering Aspects* **191**, 201-214.
- Rosenthal, Y., Lear, C.H., Oppo, D.W. and Linsley, B.K. (2006) Temperature and carbonate ion effects on Mg/Ca and Sr/Ca ratios in benthic foraminifera: Aragonitic species *Hoeglundina elegans*. *Paleoceanography* **21**, PA1007.
- Rosso, K.M., Zachara, J.M., Fredrickson, J.K., Gorby, Y.A. and Smith, S.C. (2003) Nonlocal bacterial electron transfer to hematite surfaces. *Geochimica et Cosmochimica Acta* **67**, 1081-1087.
- Russell, A.D. and Spero, H.J. (2000) Field examination of the oceanic carbonate ion effect on stable isotopes in planktonic foraminifera. *Paleoceanography* **15**, 43-52.
- Russell, A.D., Hönisch, B., Spero, H.J. and Lea, D.W. (2004) Effect of seawater carbonate ion concentration and temperature on shell U, Mg, and Sr in cultured planktonic foraminifera. *Geochim. Cosmochim. Acta*. **68**, 4347-4361.
- Scheuerman, T.R., Camper, A.K. and Hamilton, M.A. (1998) Effects of Substratum Topography on Bacterial Adhesion. *Journal of Colloid and Interface Science* **208**, 23-33.
- Spero, H.J., Bijima, J., Lea, D.W. and Bemis, B. (1997) Effect of seawater carbonate chemistry on planktonic foraminiferal carbon and oxygen isotope values. *Nature* **390**, 497-500.

- Spero, H.J., Bijma, J., Lea, D.W. and Russell, A.D. (1999) Deconvolving glacial ocean carbonate chemistry from the planktonic foraminifera carbon isotope record. *Reconstructing Ocean History: A Window into the Future*. F. Abrantes and A. Mix. N.Y., Kluwer Academic.
- Stanley, S.M. and Hardie, L.A. (1998) Secular oscillations in the carbonate mineralogy of reef-building and sediment-producing organisms driven by tectonically forced shifts in seawater chemistry. *Palaeogeography, Palaeoclimatology, Palaeoecology* **144**, 3-19.
- Stanley, S.M. and Hardie, L.A. (1999) Hypercalcification: Paleontology Links Plate Tectonics and Geochemistry to Sedimentology. *GSA Today* **9**, 1-7.
- Teng, H.H., Dove, P.M., Orme, C.A., De Yoreo, J.J. (1998) Thermodynamics of Calcite Growth: Baseline for Understanding Biomineral Formation. *Science* **282**, 724-727.
- Teng, H.H., Dove, P.M. and De Yoreo, J.J. (1999) Reversed calcite morphologies induced by microscopic growth kinetics: insight into biomineralization. *Geochimica et Cosmochimica Acta* **63**, 2507-2512.
- Teng, H.H., Dove, P.M., De Yoreo, J.J. (2000) Kinetics of calcite growth: surface processes and relationships to macroscopic rate laws. *Geochimica et Cosmochimica Acta* **64**, 2255-2266.
- Tiedje, J.M. (2002) *Shewanella* – the environmentally versatile genome. *Nature Biotechnology* **20**, 1093-1094.
- Tyrrell, T. and Zeebe, R.E. (2004) History of carbonate ion concentration over the last 100 million years. *Geochimica et Cosmochimica Acta* **68**, 3521-3530.
- Venkateswaren, K., Moser, D.P., Dollhopf, D., Lies, D.P., Saffarini, D.A., MacGregor, B.J., Ringelberg, D.B., White, D.C., Nishijima, M., Sano, H., Burghardt, J., Stackebrandt, E., Nealson, K.H. (1999) Polyphasic taxonomy of the genus *Shewanella* and description of *Shewanella oneidensis* sp. nov. *Int. J. Syst. Bacteriol.* **49**, 705-724.
- Videla, H.A. (1996) *Manual of Biocorrosion*: CRC Lewis Publishers, Boca Raton, 273 pp.
- Vinson, M.D., Arvidson, R.S. and Luttge, A. (2007) Activation and Passivation of Calcite (104) Dissolution Surface Phenomena by Mn^{2+} : Implications for the Roles of Impurity Ions and Dissolved Inorganic Carbon. *Journal of Crystal Growth* **307**, 116-125.

- Wagner, D., Fischer, W.R., Paradies, H.H. and von Franqué, O. (1996) Microbiologically Influenced Corrosion in Copper Potable Water Installations, in Heitz, E., Flemming, H.- C., Sand, W., editors, Microbially Influenced Corrosion of Materials: Scientific and Engineering Aspects: Springer, Berlin, p. 259-269.
- Wolery, T.J. (1992) EQ3NR, A Computer Program for Geochemical Aqueous Speciation-Solubility Calculations. (Version 7.0): UCRLMA-110662-PT-I, Lawrence Livermore National Laboratory, Livermore, California.
- Zeebe, R.E. and Westbroek, P. (2003) A simple model for the CaCO_3 saturation state of the ocean: The “Strangelove”, the “Netitan”, and the “Cretan” Ocean. *Geochem. Geophys. Geosyst.* **4**, 1104.
- Zhang, J. and Nancollas, G.H. (1998) Kink Density and Rate of Step Movement during Growth and Dissolution of an *AB* Crystal in a Nonstoichiometric Solution. *Journal of Colloid and Interface Science* **200**, 131-145.
- ZoBell, C.E. (1943) The effect of solid surfaces upon bacterial activity. *Journal of Bacteriology* **46**, 39-56.